

REPUBLIQUE ALGERIENNE DEMOCRATIQUE ET POPULAIRE
MINISTERE DE L'ENSEIGNEMENT SUPERIEUR ET DE LA RECHERCHE SCIENTIFIQUE

UNIVERSITE YAHIA FARES DE MEDEA
FACULTE DE TECHNOLOGIE

2020-UYFM-LBMPT

Doctorat

THÈSE

Pour obtenir le grade de docteur délivré par

L'Université Yahia Farès de Médéa

Spécialité : Génie Mécanique, énergétique nucléaire

Présentée et soutenue publiquement par

Abdelkrim TERFAI

Le 12 décembre 2020

Contribution à l'étude de faisabilité de l'utilisation des nano-fluides dans les dispositifs de l'énergie solaire.

Jury

M. Salah HANINI	Professeur, Université Y.F Médéa	Président
M. Younes CHIBA	Maitre de Conférences A, Univ. Y.F Médéa	Directeur de Thèse
M. Mohamed Najib BOUAZIZ	Professeur, Université Y.F Médéa	co- Directeur de Thèse
M. Mustapha HATTI	Directeur de recherche, CDER-UDES	Examinateur
M. Mounir ZIRARI	Maitre de Conférences A, Univ. Y.F Médéa	Examinateur

Laboratoire de Biomatériaux
et Phénomènes de Transport

THÈSE

UNIVERSITY OF MEDEA

DOCTORAL THESIS

Contribution to study the feasibility of the use of nano-fluids in solar energy devices.

Author:
Abdelkrim TERFAI

Supervisor:
Dr.Younes CHIBA
Pr. Mohamed Najib BOUAZIZ

A thesis submitted in fulfillment of the requirements for the degree of Doctor of nuclear energy

in the

Biomaterials and Transport Phenomena Laboratory
Mechanical Engineering

ملخص : الهدف الأساسي لهذه الأطروحة يمكن تلخيصه في جزأين. في الجزء الأول قمنا بتطوير نموذج عددي لمحاكاة تشغيل حوض شمسي شبه عميق يعمل حول درجة الحرارة المحيطة. الحوض الشمسي يمكن اعتباره كلاقط مسطح بخلفية سوداء ممتلئ بماء ملون بلون اسود، كما قمنا باستخدام لوح زجاجي لتغطية المياه الملونة لتعزيز فعل تأثير الاحتباس الحراري. كما تم غمر أنابيب أفقية متوازية في حوض الماء لنقل السعرات الحرارية الملتقطة من الطاقة الشمسية لسائل نقل الحرارة الموجود داخل الأنابيب. للقيام بذلك، تم حل معادلة الطاقة أحادية البعد لسائل نقل الحرارة بدلالة الزمن لغرض تحديد حقول درجات الحرارة وأداء الحوض. أيضًا ، تم استخدام موائع نانوية لتحسين نقل الحرارة وأداء الحوض الشمسي. في الجزء الثاني من الرسالة قمنا بإجراء دراسة تجريبية مع مقارنة النتائج المتحصل عليها نظرياً. كما قمنا بتحليل ومناقشة النتائج التي تم الحصول عليها بما في ذلك درجة حرارة الحوض ودرجة حرارة مائع نقل الحرارة والاشعة الشمسية .

الكلمات المفتاحية : طاقة شمسية ، حوض شمسي شبه عميق ، موائع نانوية ، أداء حراري ، دراسة تجريبية.

Résumé :

Le présent travail de thèse porte sur deux volets. Le premier volet consistait à développer un modèle numérique permettant de simuler le fonctionnement d'un bassin solaire peu profond opérant autour de la température ambiante. Le bassin est considéré comme un capteur solaire plan avec un fond noir et remplit d'eau, une vitre est utilisée pour couvrir l'eau coloré en noir afin de favoriser l'effet de serre. Un serpentin est immergé dans le bassin d'eau pour transporter les calories le fluide caloporteur issues l'énergie solaire. Pour ce faire, l'équation de l'énergie monodimensionnelle du fluide caloporteur a été résolue en régime transitoire pour évaluer les champs des températures et les performances du bassin. Aussi, les nanoluides ont été utilisés pour améliorer le transfert de chaleur et l'efficacité du bassin solaire. La deuxième partie de la thèse s'est focalisé sur l'étude expérimentale avec une confrontation des résultats obtenus théoriquement. Les principaux résultats obtenus incluant la température de bassin, la température du fluide caloporteur, le gisement solaire sont analysés et discutés.

Mots clés : Énergie solaire, Bassin solaire peu profond, Nanoluides, Performances Thermiques, Etude expérimentale.

Abstract:

This present work consists in two parts. The first part consisted of developing a numerical model to simulate the operation of a shallow solar pond operating around ambient temperature. The shallow solar pond is considered a flat solar collector with a black background and fills with water, a glass covers is used to cover the water to promote the greenhouse effect. A serpentine is submerged in the water pond to transport the heat transfer fluid calories from solar energy. To do this, the one-dimensional energy equation of the heat transfer fluid was solved in transient conditions to evaluate the temperature fields and the performance of the basin. Also, nanofluids have been used to improve heat transfer and efficiency of shallow solar pond. The second part of the thesis focused on the experimental study with a comparison of the results obtained theoretically. The main results obtained including the basin temperature, the temperature of the heat transfer fluid, the solar radiation are analyzed and discussed.

Keywords: Solar energy, Shallow solar pond, Nanofluids, Thermal performances, Experimental study.

Acknowledgements

Foremost, I give thanks to Allah who through his mercy and grace I have been able to accomplish this task.
I would like to express my deep and sincere gratitude to my supervisor, Mr. Younes CHIBA, Associate Professor at University of Medea, for his empathic understanding, encouragement and personal guidance during my work on this thesis.
I wish also to express my warm and sincere thanks to my co-supervisor, Mr.Mohamed Najib BOUAZIZ,Professor at University of Medea, who gave me assistance and guidance at all stages in this endeavour.
The members of the jury who did me the honor of evaluating my work, and more specifically:
Mr. Salah HANINI, Professor at University of Medea, for the honor he did me, by accepting the presidency of this jury.
Mr. Mustapha HATTI, Research Director, CDER-UDES
Mr. Mounir ZIRARI, Associate Professor at University of Medea
who did me the honor of accepting to be part of my jury as examiners.
I want to express my undying gratitude to my parents and family for their love and support.
Finally, my thanks go to all the people who have supported me to complete the research work directly or indirectly

Contents

Acknowledgements iii

General Introduction 1

1 Historical Background 3
- 1.1 Introduction . . . 3
  - 1.1.1 Types of solar ponds . . . 4
    - 1.1.1.1 Salt gradient Solar Ponds . . . 4
    - 1.1.1.2 Membrane Solar Ponds . . . 4
    - 1.1.1.3 Shallow Solar Pond . . . 5

2 Solar Radiation 15
- 2.1 Introduction . . . 15
- 2.2 The Earth's Motion Around the Sun . . . 15
- 2.3 Solar Times . . . 16
  - 2.3.1 True Solar Time . . . 16
- 2.4 Geographical Coordinates . . . 17
  - 2.4.1 Latitude . . . 18
  - 2.4.2 Longitude . . . 18
  - 2.4.3 Altitude . . . 19
- 2.5 Position of The Sun . . . 19
  - 2.5.1 Equatorial Coordinates . . . 19
    - 2.5.1.1 Solar Declination . . . 19
    - 2.5.1.2 Hour Angle . . . 20
  - 2.5.2 Horizontal Coordinates . . . 21
    - 2.5.2.1 Sun Height . . . 21
    - 2.5.2.2 Azimuth of The Sun . . . 22
    - 2.5.2.3 The Zenith Distance . . . 23
- 2.6 Calculation of Solar Radiation . . . 24
  - 2.6.1 Solar Radiation Outside the Atmosphere . . . 24
  - 2.6.2 Semi-Empirical Models . . . 24

2.6.2.1 Lacis & Hansen Model 25
2.6.2.2 Davies & Hay Model 26
2.6.2.3 Bird & Hulstrom Model 30
2.6.2.4 Atwater & Ball Model 33
2.6.3 Comparison of experimental and calculated results for solar radiation 34

3 Thermal Analysis of Shallow Solar Ponds 37
3.1 Introduction 37
3.2 SSP Under the Batch mode of Heat Extraction 37
3.2.1 Heat Balance Equations 38
3.2.1.1 Energy Balance Equations for The Upper Glass Cover: 39
3.2.1.2 Energy Balance Equations for The Lower Glass Cover: 41
3.2.1.3 Energy Balance Equations for The Absorber Plate: 42
3.2.1.4 Energy Balance Equations for The Pond Water 42
3.3 SSP Under the Open Cycle and Continuous Mode of Heat Extraction: 44
3.3.1 Energy Balance Equation for Absorber Plate 45
3.3.1.1 Energy Balance Equation for the Pond Water: 46
3.3.2 Energy Balance Equation for Heat Exchanger Tube Welded on The Absorber Plate: 46
3.4 Carrier Fluid Description 50
3.4.1 components of nanofluids 50
3.4.2 Thermal and physical properties of nanofluids 51
3.4.2.1 Density 52
3.4.2.2 Specific heat 53
3.4.2.3 Viscosity 53
3.4.2.4 Thermal conductivity 54
3.4.2.5 Heat transfer 56

4 Results and Discussion 59
4.1 Results obtained from a numerical simulation of SSP under different operating conditions 59

4.1.1 Numerical Simulation of SSP Under the Batch Mode of heat Extraction 60
4.1.1.1 The Effect of the Depth of the Pond Water on the Thermal Performance of the SSP 61
4.1.1.2 The Effect of the Gap Between the Glass Covers on the Thermal Performance of the SSP . . 62
4.1.1.3 The Effect of Insulating Material Thickness on the Thermal Performance of the SSP 62
4.1.2 Numerical Simulation of the SSP Under the Open and Continuous mode of heat Extraction 64
4.1.2.1 The Effect of heat Exchanger Length on the Thermal Performance of the SSP 65
4.1.2.2 The Effect of heat Exchanger Diameter on the Thermal Performance of the SSP 66
4.1.2.3 The Effect of Mass Flow Rate on the Thermal Performance of the SSP 67
4.1.3 The effect of using nanofluids on the thermal performance of the SSP 68
4.1.3.1 Thermophysical Properties of Nanofluids . . 69
4.1.3.2 The effect of nanoparticles on the thermal conductivity of nanofluids 69
4.1.3.3 The effect of nanoparticles on the dynamic viscosity of nanofluids 71
4.1.3.4 The effect of nanoparticles on the specific heat capacity of nanofluids 71
4.1.3.5 The effect of nanoparticles on the density of nanofluids 72
4.1.3.6 The effect of nanoparticles on the outlet temperature of the nanofluids 72
4.1.3.7 Comparison between the outlet temperature for different nanofluids 74
4.1.3.8 The effect of nanoparticles on the useful energy extracted 75
4.1.3.9 Comparison between the useful energy for different nanofluids 78
4.1.3.10 The effect of nanoparticles on daily efficiency 78

5 Experimental techniques **81**
5.1 Introduction 81
5.2 Material and Methods 81
5.2.1 Solar Radiation Calculation 81
5.2.2 Temperature Measurement 82
5.2.2.1 Ambient air temperature and humidity measurement 82
5.2.2.2 Measuring the Temperature of SSP Components 82
5.2.3 Microcontroller 83
5.2.4 Water Pump 83
5.3 Experiment Description 83
5.3.1 The SSP is operated under the batch mode for heat extraction 83
5.3.2 The SSP is operated under open cycle and continuous heat extraction mode 85
5.4 Results of Experimental Tests 86

General Conclusion **95**

List of Figures

1.1 Diagram showing the salt gradient solar pond 5
1.2 Diagram showing a typical shallow solar pond design 5
1.3 a compact shallow solar pond 7
1.4 Schematic diagram of shallow solar pond. 9
1.5 A schematic diagram of a single-basin solar still coupled with the shallow solar pond. 12
1.6 A schematic diagram of the active solar still coupled with a shallow solar pond and a storage water tank. 13

2.1 Earth at seasonal points in its orbit 16
2.2 Evolution of the time equation as function of the days of the yea 17
2.3 The difference between true solar time and legal time 18
2.4 Sun-Earth angles 19
2.5 Variation in solar declination angle as function of the days of the year 20
2.6 Hour angle variation as a function of timer 21
2.7 Horizontal coordinate system 22
2.8 Variation of the height of the sun - Site: Medea during a day and throughout the year 22
2.9 Variation of the azimuth of the Sun - Site: Medea during a day and throughout the year 23
2.10 Variation of the zenith distance - Site: Medea during a day and throughout the year 23
2.11 Annual evolution of the solar constant 24
2.12 Solar radiation calculated by the Lacis & Hansen model - Site: Medea during a day and throughout the year 27
2.13 Solar radiation calculated by the Davies & Hay model - Site: Medea during a day and throughout the year 30
2.14 Solar radiation calculated by the Bird & Hulstrom model - Site: Medea during a day and throughout the year 33

2.15 Solar radiation calculated by the the Atwater & Ball model - Site: Medea during a day and throughout the year 34
2.16 A comparison between the measured and calculated results of solar radiation according to the four models of the site of Ouargla 35

3.1 A schematic diagram showing the studied SSP operating under the batch mode of heat extraction 38
3.2 Diagram showing the heat transfer mechanisms in SSP operating under a batch mode for heat extraction 39
3.3 A schematic diagram showing the studied SSP operating under the open cycle mode of heat extraction. 44
3.4 Diagram showing the heat transfer mechanisms in SSP operating under the open cycle mode of heat extraction. 45
3.5 Length scale and some examples related 50
3.6 The most important nanoparticles used in the preparation of nanofluids 51
3.7 Some basic fluids used in the preparation of nanofluids 52

4.1 Hourly values of solar radiation I_T at Medea calculated by the Bird & Hulstrom model and the ambient air temperature on August 18 60
4.2 Calculated pond water temperature T_w vs time for different depth of the pond water 61
4.3 Calculated pond water temperature T_w vs time for different distance between the lower and upper glass covers 62
4.4 Calculated pond water temperature T_w vs time for different thicknesses of insulating material 63
4.5 Variation of the pond water temperature T_w during the day and throughout the year 63
4.6 Variation of the useful energy collected during the day and throughout the year 64
4.7 Calculated outlet temperature of the heat transfer fluid T_{fo} as a function of time for different values of the heat exchanger length 65
4.8 Calculated outlet temperature of the heat transfer fluid T_{fo} as a function of time for different values of diameter of the heat exchanger 66

4.9 Calculated outlet temperature of the heat transfer fluid T_{fo} as a function of time for different values of mass flow rate 67
4.10 hourly variations in useful energy $\dot{Q}_u$ vs time for different value of mass flow rate 68
4.11 Impact of nanoparticles volume fraction on thermal conductivity of nanofluids 70
4.12 Impact of nanoparticles volume fraction on dynamic viscosity of nanofluids 70
4.13 Impact of nanoparticles volume fraction on specific heat capacity of nanofluids 71
4.14 Impact of nanoparticles volume fraction on mass density of nanofluids 72
4.15 Calculated outlet temperature of the nanofluids $(Al_2O_3 + H_2O)$ vs time for different nanoparticles volume fraction φ 73
4.16 Comparison between calculate outlet temperature of the nanofluids vs time with nanoparticles volume fraction φ=5 (%) for different types of nanofluids and $\dot{m}_{nf}$= 0.003 (Kg/s) 74
4.17 Comparison between calculate outlet temperature of the nanofluids vs time with nanoparticles volume fraction φ=5 (%) for different types of nanofluids and $\dot{m}_{nf}$= 0.007 (Kg/s) 75
4.18 Calculated useful energy of the nanofluids $(Al_2O_3 + H_2O)$ vs time for different nanoparticle volume fraction φ 76
4.19 Comparison between calculate useful energy of the nanofluids vs time with nanoparticles φ=5 (%) for different types of nanofluids and $\dot{m}_{nf}$= 0.003 (Kg/s) 77
4.20 Comparison between calculate useful energy of the nanofluids vs time with nanoparticles φ=5 (%) for different types of nanofluids and $\dot{m}_{nf}$= 0.007 (Kg/s) 77
4.21 Daily collection efficiency with nanoparticle volume fraction φ=5 (%) for different types of nanofluids: $\dot{m}_{nf}$ = 0.003 (Kg/s) . 79
4.22 Daily efficiency of heat removell with nanoparticle volume fraction φ=5 (%) for different types of nanofluids: $\dot{m}_{nf}$ = 0.003 (Kg/s) 79

5.1 Measuring instrument used in the experimental study 84
5.2 Photograph showing the operation of the SSP under the batch mode of heat extraction 85

5.3 Photograph showing the operation of the SSP under the open cycle mode of heat extraction 86
5.4 Hourly variations of the calculated solar radiation by Bird & Hulstrom model 87
5.5 Hourly variations of the measured ambient temperature under the batch mode of heat extraction 87
5.6 Comparison between experimental and calculated results for the temperature of the upper glass cover of the SSP operating under the batch mode for heat extraction 88
5.7 Comparison between experimental and calculated results for the temperature of the lower glass cover of the SSP operating under the batch mode for heat extraction 88
5.8 Comparison between experimental and calculated results for the temperature of the pond water of the SSP operating under the batch mode for heat extraction 89
5.9 Comparison between experimental and calculated results for the temperature of the absorber plate of the SSP operating under the batch mode for heat extraction 90
5.10 Hourly variations of the measured ambient temperature under the open cycle mode of heat extraction 90
5.11 Hourly variations of the measured inlet temperature of the heat transfer fluid under the open cycle mode of heat extraction 91
5.12 Comparison between experimental and calculated results for the temperature of the upper glass cover of the SSP operating under the open cycle and continuous heat extraction mode . . 92
5.13 Comparison between experimental and calculated results for the temperature of the lower glass cover of the SSP operating under the open cycle and continuous heat extraction mode . . 93
5.14 Comparison between experimental and calculated results for the outlet temperature of the heat transfer fluid of the SSP operating under the open cycle and continuous heat extraction mode 93
5.15 Comparison between experimental and calculated results for the pond water temperature of the SSP operating under the open cycle and continuous heat extraction mode 94

5.16 Comparison between experimental and calculated results for the temperature of the absorber plate of the SSP operating under the open cycle and continuous heat extraction mode . . . 94

List of Tables

2.1 Some ground albedo value. 25
2.2 Parameters α and β according to different states of the atmosphere 28
2.3 Values of factor F_C as a function of zenith distance 29
2.4 Geographical coordinates of the site used 34

3.1 The coefficients of the water transmittance 46
3.2 Ratio of the viscosities of the nanofluid $(Al_2O_3 + H_2O)$ obtained from the different models studied 54
3.3 Values of thermal conductivities of nanoparticles and fluids used 55

4.1 Numerical parameters which were used for numerical calculations 60
4.2 Thermophysical properties of base fluid and nanoparticles . . 69
4.3 Maximum temperature values for different nanofluids and with different volume fraction 74
4.4 Maximum useful energy values for different nanofluids and with different volume fraction 76

List of Symbols

A	area	m^2
A_t	cross sectional area	m^2
a_z	azimuth of the sun	$^\circ$
C_P	specific heat	J/ Kg K
D	diameter	m
D_i	time difference	hour
E_T	the correction of the equation of times	min
g	acceleration due to gravity	m/s^2
h	height of the sun	$^\circ$
h_C	convective heat transfer coefficient	W/m^2K
h_R	radiative heat transfer coefficient	W/m^2K
I_0	solar constant	W/m^2
I_{sc}	the corrected solar constant	W/m^2
I_T	global solar radiation	W/m^2
K	Thermal conductivity	W/mK
L	the reduced ozone thickness	cm
L	length	m
Lon	Longitude	$^\circ$
L_T	legal time	hour
m_a	air mass	–
m_r	relative optical air mass	–
m_w	mass of the pond water	Kg
$\dot{m}_f$	mass flow rate	Kg/s
N	Number of the day of the year from January 1	–
Nu	Nusselt number	–
Gr	Grashof number	–
P	perimeter	m
P	atmospheric pressure	mbar
P_0	atmospheric pressure at sea level	mbar
Pr	Prandtl number	–

Ra	Rayleigh number	$-$
T	temperature	K
T_{ST}	true solar time	hour
U_0	the thickness of the ozone layer corrected	cm
U_W	thickness of the condensed water vertically from the place	cm
V	wind speed	m/s
X	thickness	m
X_W	thickness of condensed water corrected	cm

α	thermal diffusivity	m^2/s
α	absorptivity	$-$
α_0	Transmittance of ozone ahsorptance.	$-$
α_W	Water vapor absorptance	$-$
β	temperature coefficient	$1/K$
δ	solar declination	$\circ$
ε	emissivity	$-$
η	efficiency	%
θ_z	zenith distance	$\circ$
μ	absolute viscosity	Ns/m^2
μ_i	extinction coefficient	m^{-1}
ν	kinematic viscosity	m^2/s
ρ	mass density	Kg/m^3
$\rho_S^{'}$	soil albedo	$-$
σ	Stefan Boltzmann constant	W/m^2K^4
τ	transmissivity	$-$
φ	Latitude	$\circ$
φ	volume fraction	%
ψ_i	solar radiation portion	$-$
ω	hour angle	$\circ$

a	ambient
c	cover
g	glass
is	isolation
nf	nanofluid
he	heat exchanger

s sky

w water

SSP **S**hallow **S**olar **P**ond

General Introduction

The world's dependence on industry has become an imperative, so the need for energy is increasing in order to support economic development and the needs in terms of comfort and consumption for the population, at the present time, we are approaching a critical moment in energy exploitation, where fossil energy resources and even fission are gradually reduced. Thus, the crude oil and natural gas fields will be practically exhausted in the long term. In addition, the intensive use of fossil fuels and coal causes serious environmental damage in addition to the phenomenon of global warming. The economic consequences of the oil shocks in the 1970s [1, 2] led to the necessity to find alternative solutions to the energy problem, which led scientific research to move towards renewable energies. Solar energy is one of the most important renewable energy. Its importance is due to the fact that it is available worldwide and during the year. In addition, it is a clean energy that does not have a negative impact on the environment and is considered a good alternative to fossil fuels [3]. Algeria is considered one of the countries with abundant solar radiation in the world. Among the methods of collecting and storing solar energy is a shallow solar pond SSP, a solar pond is a water body [4], it is a unique and free system of energy sources to collect, convert and store solar energy into thermal energy, and use it in industrial and household applications that depend on a low temperature, or medium. The thermal transfer plays an effective role in making use of the thermal energy collected by the shallow solar pond in order to transport it and store it in thermally insulated tanks for use when needed.However, conventional fluids used in thermal processes such as water, engine oil and ethylene glycol possess low thermal properties such as thermal conductivity, which may limit and severely restrict heat transfer efficiency. One of the most important ways to overcome this problem is to use nanofuids, which are a colloidal fluid consisting of small particles ranging in size from 1 to 100 nanometers suspended in a basic liquid such as water [5]. It has been proven that adding nanoparticles such as copper or aluminum oxide to conventional liquids improves significant

thermal conductivity. The aim of this PhD thesis is the theoretical study of the effect of using nanofluids on the thermal performance of a shallow solar pond operating under open and continuous heat extraction mode . That is why we developed the following action plan: The manuscript consists of five chapters and an introduction and general conclusion.

- In the first chapter we presented a historical overview of the solar pond and its types, in addition to some previous studies that dealt with the shallow solar pond.
- In the second chapter, we described the basic concepts related to solar radiation calculation in addition to four semi-emperical models in order to predict solar radiation and compare it with experimental data in order to choose a model for use in numerical simulations.
- The third chapter is devoted to mathematical models resulting from the energy balance equations between the various components of the solar pond, in addition to mentioning some models that allow calculating the physical and thermal properties of nanofluids.
- In the fourth chapter, the results from numerical simulations of a shallow solar pond are presented and discussed under different heat extraction designs and methods.
- In the fifth chapter, an experimental study of the shallow solar pond operating under the batch mode on one hand and the open cycle mode and continuous heat extraction on the other hand was made, in order to verify the correctness of the mathematical model.
- Finally, we end this manuscript with a general conclusion that summarizes the work done

Chapter 1

Historical Background

1.1 Introduction

A solar pond is a body of water used to collect and store solar energy by converting it into thermal energy, and it is considered one of the simplest and least expensive technologies and it has a unique ability to work as a collection and storage system , it is used in many areas that depend on temperature low or medium range, such as air conditioning, desalination, heating [6], and power generation via the Organic Rankine Cycle Engine [7]. In short, solar ponds have enormous potential applications for military bases around the world.

Solar ponds are not an emerging phenomenon.Kalychinsky referred to the concept of solar ponds in 1902 after noticing that the temperature of Lake Medvie in Transylvania, Hungary reached 70 $(^{\circ}C)$ at a depth of 1.3 (m) at the end of summer. Anderson reported in 1958 that there was a lake with a temperature of 50 $(^{\circ}C)$ at a depth of 2 (m) at the end of the summer in Oroville(Washington State) .The concept of an artificial solar pond as a possible means of collection and storage of solar energy was proposed in Israel by Bloch. The first experimental solar pond began operation around 1959 (Tabor,1959, 1961). Subsequently, many investigations on the physics and engineering of the solar pond were reported (Tabor 1963; Weinberger, 1964; Elata and Levin, 1965; Tabor and Mat.z,1965). These studies and reports are the ones that introduced salinity gradient solar pond technology to the world. and this research, in which the main goal was to produce electrical power, provided important data that are still relevant today [8].

1.1.1 Types of solar ponds

Solar ponds can be either natural or artificially formed from bodies of water that collect and store solar energy. Although most of this energy is lost to the atmosphere mainly as a result of convection and evaporation, various techniques are used to reduce the convection or heat loss and thus trap a large amount of energy inside the pond. There are several types of solar ponds, These types will be briefly discussed below:

1.1.1.1 Salt gradient Solar Ponds

One of the most common types of solar ponds is a saline gradient solar pond, its depth is usually between 1 and 2 (m) and the bottom is painted black [9, 10].The typical saline gradient solar pond consists of three main areas as shown in figure 1.1:

- The surface layer, which is also called the upper convection zone. This areanis characterized by small concentrations of salt. Its temperature is close to the ambient temperature, the thickness of this surface layer ranges from 0.1 to 0.4 (m) and it is formed due to the transport of rising salt, surface heating, cooling and wave movement. The importance of this layer is to prevent the lower layers from being exposed to evaporation, wind effects and falling impurities.

- The second layer is called the middle layer or the non-convicting zone NCZ, the salt concentration increases with the increasing depth of the pond, the depth of this layer ranges between 0.6 to 1.0 (m), and although this layer is not homogeneous, it acts as an insulating layer for the pond.

- The lower layer is called the storage zone and it is an area that contains a high concentration of salt. The thickness of this zone depends on the temperature and the amount of heat to be stored. Usually, the beneficial heat is extracted from this layer.

1.1.1.2 Membrane Solar Ponds

In the membrane pond, the pond is provided with two thin transparent films to separate each area of the pond. This pond uses the same concept of a salinity solar pond in its work [10].

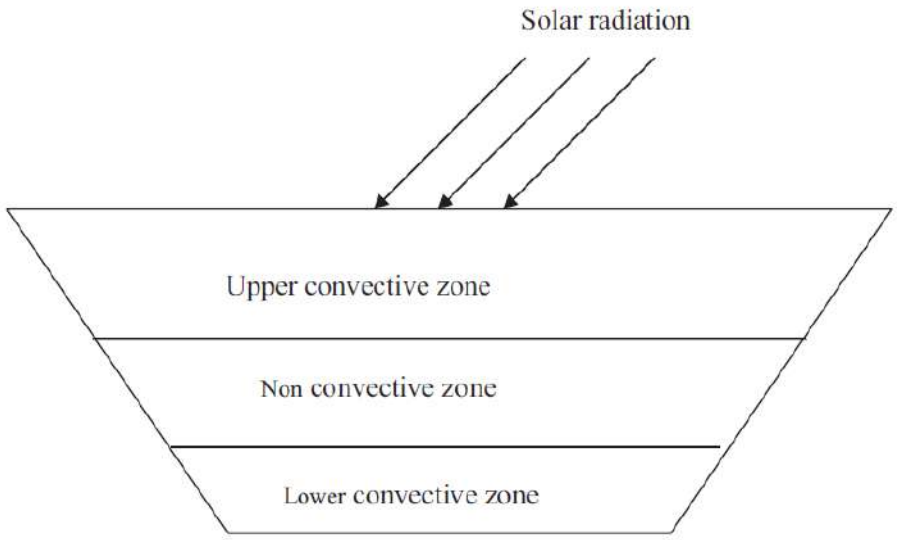


FIGURE 1.1: Diagram showing the salt gradient solar pond [6]

1.1.1.3 Shallow Solar Pond

A shallow solar pond as shown in figure 1.2 is a fairly large solar collector, typical SSP units are 5 x 60 (m) with a water depth of about 0.1 (m) . As the name indicates, the depth of the pond is shallow, ranging between 0.4 to 0.15 (m) . It is a large plastic bag that contains water placed in a thermal insulated container. The shallow solar pond was developed to provide medium temperature water ranging from 40 to 60 $(°C)$.The temperature of the pond water is inversely proportional to the depth of the water, but the collected heat is directly proportional to the water depth. There are three modes of op-

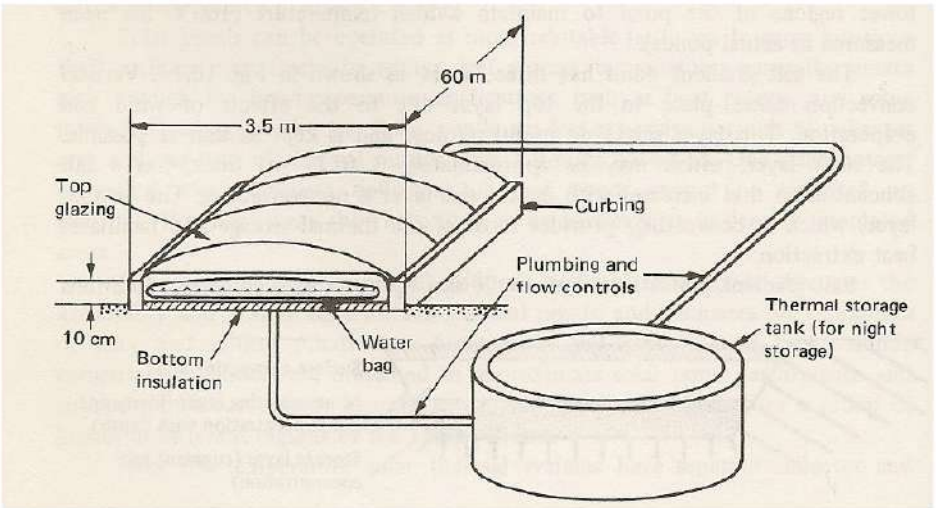


FIGURE 1.2: Diagram showing a typical shallow solar pond design [10]

eration possible with the SSP [11]. The first mode is called the batch-heating mode in which, the pond is filled in the early morning with water at an initial temperature Twi. In the afternoon, when the water temperature reaches its maximum value, the pond is emptied into an insulating reservoir. In the second mode, which called the closed-cycle continuousflow heating mode, the water is continuously circulated at a constant rate between the pond and the storage reservoir from which heat may or may not be continuously removed by a heat exchanger. When the useful heat added to the pond water reaches zero, all of the pond water is emptied into the reservoir. The third mode is called the open-cycle continuous-flow heating-mode in which the water at the initial temperature Twi flows continuously at a constant rate through the pond and then either to storage or to some end-use. As in the closed-cycle mode, water is drained from the pond when the useful heat added to the pond reaches zero, Shallow solar ponds find applications in innumerable processes requiring hot water. A few of these applications are listed below [10, 12]:

- Providing hot water for space heating purposes.
- Using a SSP for desalination by combining it with a solar still
- Supplying pre-heated water to industrial boilers.
- Providing industrial process heat.
- Providing service hot water.
- Generating electric power from hot water of SSP.
- For washing bottles in dairies and in different industries.
- Supplying hot water for washing clothes in laundry.

The idea of using a shallow, small-sized solar pond as a water heater is not new, The Japanese have been using numerous variations of this idea to heat water for domestic usage since the 1930's. In fact, 39 patents were issued for solar water heaters in Japan in the 1930's and another 20 were issued in the 1940's, the majority of these being for the water pillow type , also it has been reported in the literature that the Japanese used about 250,000 water pads in the early 1960, which is a transparent plastic bag on the top and painted in black from the bottom filled with water, placed inside a thermally insulated

support. The goal of these pillows is to provide hot water during the afternoon [13, 12].

The shallow solar pond has been touched by many scientific studies over the past century.as shown in figure 1.3 , [13] have done the testing on a compact SSP designed for camping and military use. Their prototype design consisted of a water pillow placed within an insulated container. The container cover was insulated on the outside to maintain the water temperature for overnight storage and fitted with a mirrored surface (aluminized mylar) on the inside to function as a reflector, when open and in operation during the day. A

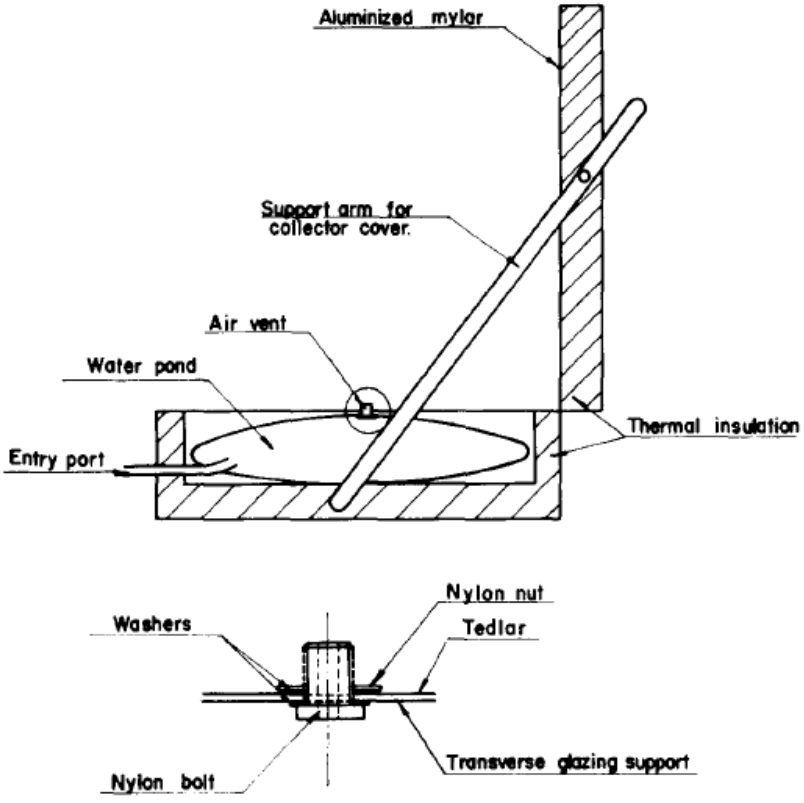


FIGURE 1.3: a compact shallow solar pond [13]

clarification was provided of the use of the ssp as an effective means of producing electric power using water to collect and store heat by Dickinson et al [7]. the collected heat is stored during the day inside an insulated water tank at night, this hot water heats the freon 11, which recycles the turbine and an electric generator.

Sodha et al [14] have done the analytical study of the system consisting of a metallic rectangular tank with black bottom and sides and a transparent cover at the top. It is concluded that one dimensional analysis is adequate

for prediction of the performance of the shallow solar pond water heater. The daily efficiency would increase if water would be continually withdrawn for consumption, thereby reducing the average pond water temperature and the resultant rate of heat loss.

A mathematical model was proposed by sodha et al [15] to predict the performance of a ssp fitted with a single cover and heat exchanger, which was simulated through a change flow rate ,It is seen that efficiencies may be achieved as high as 60 (%) at water flow rates of 0.1 - 0.2 (kg/s) . There after, the efficiency becomes almost constant at higher flow rates.

A mathematical model was proposed by Dutt et al [16] to predict the performance of a ssp with a single cover and a baffle plate. Digital simulation was performed on a cold day December 18, 1984 in New Delhi. It was concluded that the performance of the SSP using the baffle plate was better than a pond without a baffle plate .

Kamiuto et al [17] studied the thermal performance of the SSP theoretically and practically, the change in the number of transparent covers of the shallow solar pond is from zero to three covers, and it was found that the best performance is the presence of two covers .

Kishore et al [18] have presented the construction and fabrication details of portable shallow solar pond. The results have shown that the Portable shallow solar pond water heater was suitable of middle income groups due to low cost.

Ali et al [19] has proposed a theoretical model to predict the performance of a shallow solar pond in Tehran. The theoretical results obtained are in close agreement with experimental results.

Ibrahim et al [20] has analyzed the performance of a mobile covered shallow solar pond and concluded that the performance of the pond to be trouble – free and suitable for practical water heating use. The calculated values are in good agreement with the experimental value.

The thermal performance of shallow solar pond under batch and open cycle heat extraction mode were experimentally examined by Ramadan [4]. The pond performance is examined in terms of heat loss coefficients, power loss rates and combined energy. It was found that the use of an additional cover glass reduces the total loss coefficients Ut and Ul by 54 (%) and 44 (%) , respectively. The highest value of the rate of energy collected Qcoll. 644 (W) achieved when using a pond with double glass covers and an outside mirror.

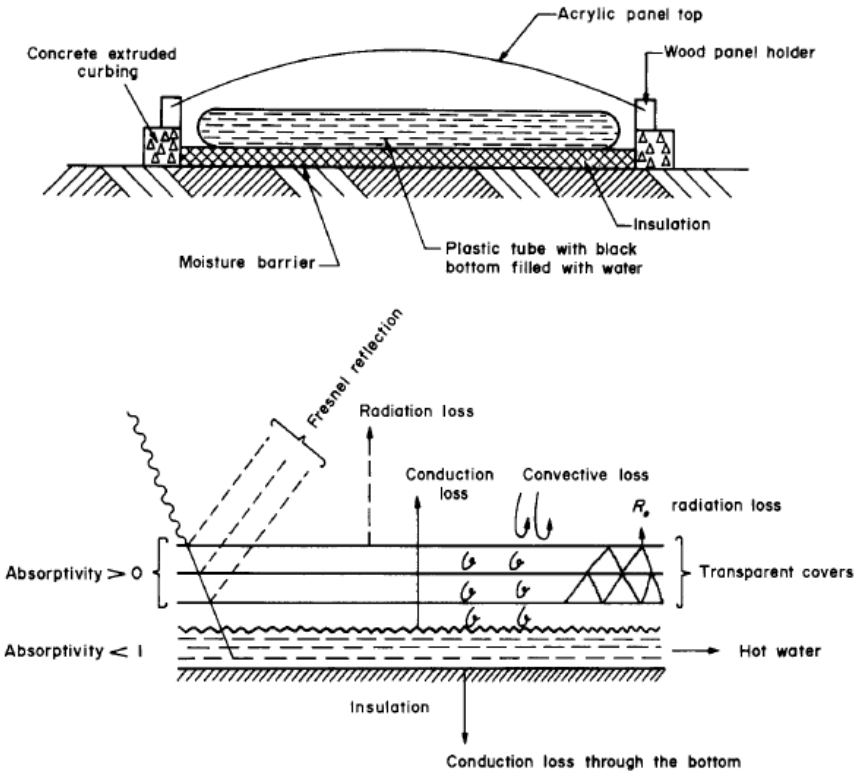


FIGURE 1.4: Schematic diagram of shallow solar pond. [13]

Moreover, tap water is used as a liquid flowing through a heat exchanger, welded to a pond absorber plate, to extract heat in the open cycle mode. The outlet temperature of the heat transfer fluid is found to decrease with increasing mass flow rate. Comparisons are made between the two thermal extraction modes based on the efficiency and successive operation of the pond. The long-term performance of the pond was checked under the best operating conditions by computer simulation for an entire year. It is inferred that the existing SSP can be used as a source of warm water required for domestic applications.

Aboul-Enein [11] studied the thermal performance of a shallow solar pond operating under the batch mode to extract heat, and he also made a numerical simulation based on solutions of the energy balance equations between the various components of the pond resulting from a proposed mathematical model, to improve the performance of the pond, which is provided with a mirror in order to enhance the amount of solar radiation the falling on the cover of the pond, numerical calculations were made in order to test the effect of the structural parameters of the pond represented in the depth of the pond water, the thickness of the insulating material and the wind speed in

addition to the height and width of the mirror, and the effect of the increase in the number of glass covers at night was also tested. Experiments indicated that the pond could provide 88 liters of hot water at a maximum temperature of 60 $(^{\circ}C)$ at sunset. The pond can hold hot water until 7 am the next day at a temperature of 47 $(^{\circ}C)$,Comparisons between experimental and theoretical results showed that good agreement was reached.

El-Sebaii [21] made a numerical simulation based on solutions to the thermal equilibrium equations for the pond. He also provided a mathematical model for a shallow solar pond that works under the batch mode to extract heat and is integrated with a baffle plate. The pond was examined theoretically and experimentally. It is concluded that the present system can provide 88 liters of hot water at a maximum temperature of 71 $(^{\circ}C)$ at 3:00 pm with a daily efficiency of 64.3 (%) when using the a baffle plate. The pond can hold hot water until 7:00 the next morning at a temperature of 43 $(^{\circ}C)$, which can be used in most home applications. The comparisons between experimental and theoretical results indicated that the theoretical model could be used to estimate the performance of the ponds with good accuracy.

The thermal performance of a shallow solar pond operating under the open cycle mode and continuous heat extraction was examined by El-Sebaii et al [22], a numerical simulation was made to compare the thermal performance of the pond, by providing the pond with a heat exchanger, either by welding it to the absorption plate, or by submerging it in the pond water, the numerical simulation were carried out based on solutions of the energy balance equations between the different components of the pond, in order to improve the system performance, optimization were made to the heat exchanger design parameters represented in its length and diameter in addition to the effect of the mass flow rate on the thermal performance of the system. The obtained results concluded that the outlet temperature of the heat transfer fluid increases with the increase in the length of the heat exchanger, while it decreases with the increase in the mass flow rate. It was concluded that the typical value of the length of the heat exchanger is 4 (m) , while the typical value of the mass flow rate is 0.004 (Kg/s), and a comparison was made between experimental and theoretical results. It turns out that there is a good agreement between them.

El-Sebaii et al [23] compared the thermal performance of a shallow solar pond operating under two different heat extraction modes. The first mode is

to operate the pond under the open cycle mode and continuous heat extraction, while the second mode is to operate the pond under the closed cycle heat extraction mode. A numerical simulation was made based on solutions of the energy-balance equations of the system elements, as the various components of the system were optimized, the system performance was checked throughout the year under the best configuration and operating conditions through computer simulations. Daily efficiencies were obtained at 59 (%) and 33 (%) when operating the pond with closed and open cycle mode , respectively. The comparisons between experimental and theoretical results showed that the proposed mathematical models could be used to examine the thermal performance of the SSP with reasonable accuracy.

Janarthanan [24] compared the thermal performance of two solar ponds experimentally and theoretically: one with a depth of 0.06 m and the other with a depth of 0.15 m. He concluded by his study that the pond with a depth of 0.06 m with a maximum temperature of 57 $(^{\circ}C)$ provides a better performance than the pond with a depth of 0.15 (m) with a maximum temperature of 42$(^{\circ}C)$.

As shown in figure 1.5 El-Sebaii et al [25] studied the effect of integrating a shallow solar pond operating under the open cycle mode and continuous heat extraction with a solar still in order to improve the daily productivity of solar distillers, for the sake of doing d numerical simulations, a computer program was prepared based on solutions of the energy balance equations of the studied system that were solved analytically. numerical calculations were carried out for different water thicknesses and mass flow rates to know their impact on daily productivity and system efficiency by using geographical and climatic inputs for the city of Tanta on summer and winter days, Comparisons between the calculated and measured results were made to verify the validity of the proposed theoretical model. A good deal was reached. Offers were also investigated throughout the year for silence with and without SSP. The optimum values of effluent water thickness and mass flow rate for this typical active sun SSP formation were obtained as 0.03 (m) and 0.0009 (kg/s). Average annual values of daily Pd yield and gd efficiency were found to be still higher with SSP than those obtained without SSP at 52.36 (%) and 43.80 (%), respectively.

Terfai et al [26, 27] made a numerical simulation of a SSP operating under the open and closed cycle of heat extraction was performed, Improvements

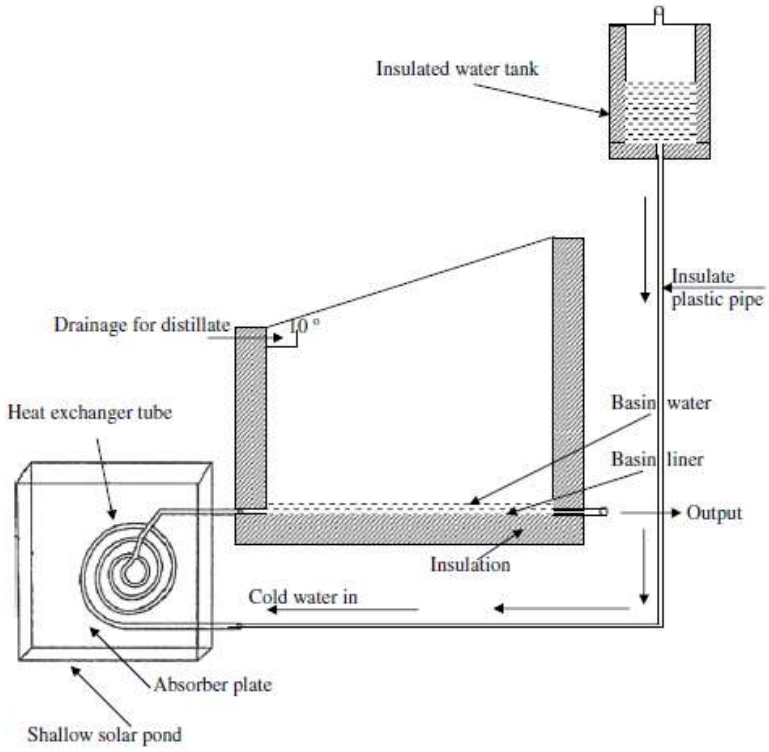


FIGURE 1.5: A schematic diagram of a single-basin solar still coupled with the shallow solar pond [25]

have also been made to various components of the SSP including the heat exchanger and storage water tank, the obtained results showed that the thermal performance of the SSP is better when working in the closed cycle mode. Terfai et al [28] has developed a calculation code that allows calculating the exergy of a shallow solar pond, and in another work Terfai et al [29, 3] has developed an algorithm based on neural networks and the Matlab program that allows predicting the exrgy and the temperature values of the different elements of the pond respectively.

In another work, and in order to improve the daily productivity of a solar still,El-Sebaii et al [30] studied the effect of combining a solar still with a shallow solar pond operating under closed-cycle heat extraction mode as shown in the figure 1.6. The results obtained from the numerical simulation resulting from the energy balance equations of the studied system showed that the daily productivities of the active single basin solar still were found to be 5.740 and 1.830 (kg/m2 day) with and without the SSP, respectively. The daily productivity Pd and efficiency d of the active still were found to decrease with increasing the thickness dw and mass flow rate $\dot{m}$ of the water flowing over the basin liner of the still up to typical values of 0.030 m and 0.015 kg/s.

Moreover, the monthly average of the daily productivity Pd had minimum values of 3.0 and 1.570 (kg/m2 day) in December with and without the SSP, respectively. The maximum values of Pd were found to be 6.68 and 5.29 (kg/m2 day) in July with and without the SSP, respectively. To validate the proposed mathematical models, comparisons between experimental and theoretical results had been performed. Good agreement had been achieved.It was also mentioned that the studied system as a source of drinking water is relatively easy to establish, operate and test for several years without much attention to maintenance and repair. It consists of cheap and available materials such as wood and glass panels, in addition to metal parts and a heat exchanger. On the other hand, this system provides a suitable solution to the freshwater problems that people who live in remote and rural areas of the world face, especially in developing countries.

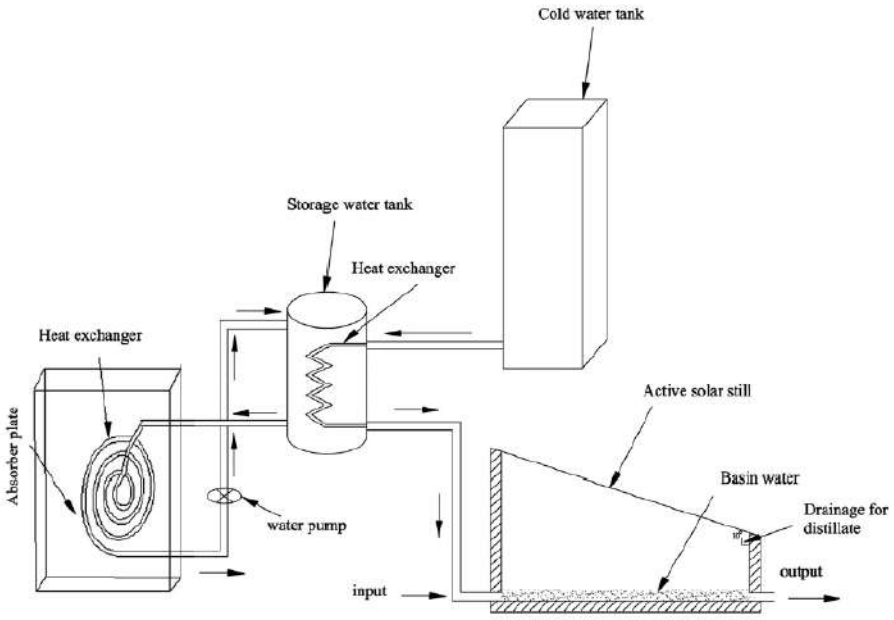


FIGURE 1.6: A schematic diagram of the active solar still coupled with a shallow solar pond and a storage water tank [30]

Chapter 2

Solar Radiation

2.1 Introduction

Solar energy is one of the most important renewable energies. Its importance is due to the fact that it is available throughout the world and during the year. In addition, it is a clean energy that has no negative impact on the environment and is considered a good substitute for fossil fuels [3]. Accurate information about the solar radiation availability is very important for researchers, the best way to know about the availability of solar radiation is possible through the processing of satellite images and measurements from appropriate measuring instrumentations such as pyranometers or pyrheliometers at a set of locations in a region with day-by-day recording, maintenance and calibration .a solar radiation database is mandatory for the design, evaluation or installation of solar systems, but it is not possible to provide a measured database practically, always or easily at any location, due to the cost of maintenance of the measuring devices, so a solar radiation database is provided through semi-empirical models that depend on meteorological parameters that are easy to measure, such as ambient air temperature, humidity, or geographic parameters such as longitude ,latitude in addition to altitude [31, 32].

2.2 The Earth's Motion Around the Sun

The Earth takes 365.25 days to complete one revolution around the sun, through its passage through a semicircular elliptical orbit, and this orbit is called the ecliptic plane, and the Earth approaches the sun by a distance of 147 million (Km) in the winter solstice (December 21), while it moves away from it in the summer to reach to a distance of 152 million (Km) and an average distance of

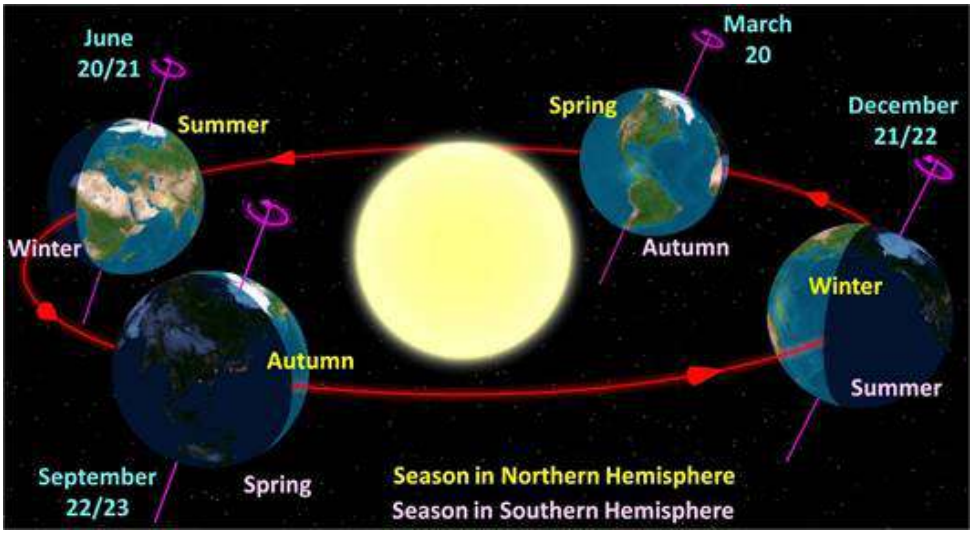


FIGURE 2.1: Earth at seasonal points in its orbit

149.5 million (Km), the Earth crosses the small axis of its orbit in the spring. Equinox (March 21) and autumn (September 21). Earth takes 24 hours to spin around. The axis of rotation (the axis of the poles) has a constant orientation in the ecliptic.

2.3 Solar Times

2.3.1 True Solar Time

The true solar time is defined by the Earth's rotation on itself. So, it is directly related to the time angle. The Earth performs a full cycle in 24 hours. At noon (12:00) when the sun is at its height, we have [33]:

$$T_{ST} = L_T - D_i + \left(\frac{E_t + 4Lon}{60}\right) \tag{2.1}$$

T_{ST}: True solar time which is equal to the legal time corrected by an offset due to the difference between the longitude of the place and the reference longitude.
L_T: legal time (given by a watch).
D_i:time difference from the Greenwich meridian (equal to 1 for Algeria).
E_T:is the correction of the equation of times. This correction varies over the year from 14.59 (min) to 16.45 (min). It can be calculated by the approximate formula [1]:

$$E_t = 9.87 \times \sin(2N_P) - 7.53 \times \cos(N_P) - 1.5 \times \sin(N_P) \tag{2.2}$$

E_T calculated in minutes and as a decimal fraction of the minute.

$$N_P = \frac{360}{365}(N - 81) \tag{2.3}$$

N: is the number of the day of the year from January 1.
L_{on}:Longitude of the place, in degrees.

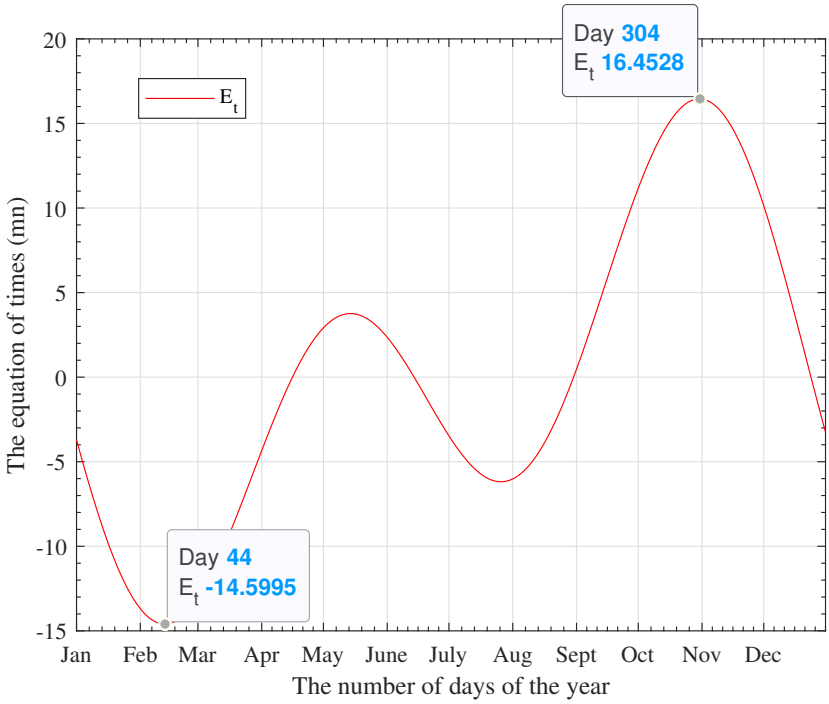


FIGURE 2.2: Evolution of the time equation as function of the days of the year.

As shown in figure 2.3 We took the city of Medea as an example. It is evident that there is a 55 minutes gap between the two times.

2.4 Geographical Coordinates

The Earth is separated by the virtual equator into two parts: the northern hemisphere of the point on the north pole side, and the southern hemisphere of the hemisphere on the south pole. It is also divided into two parts, west

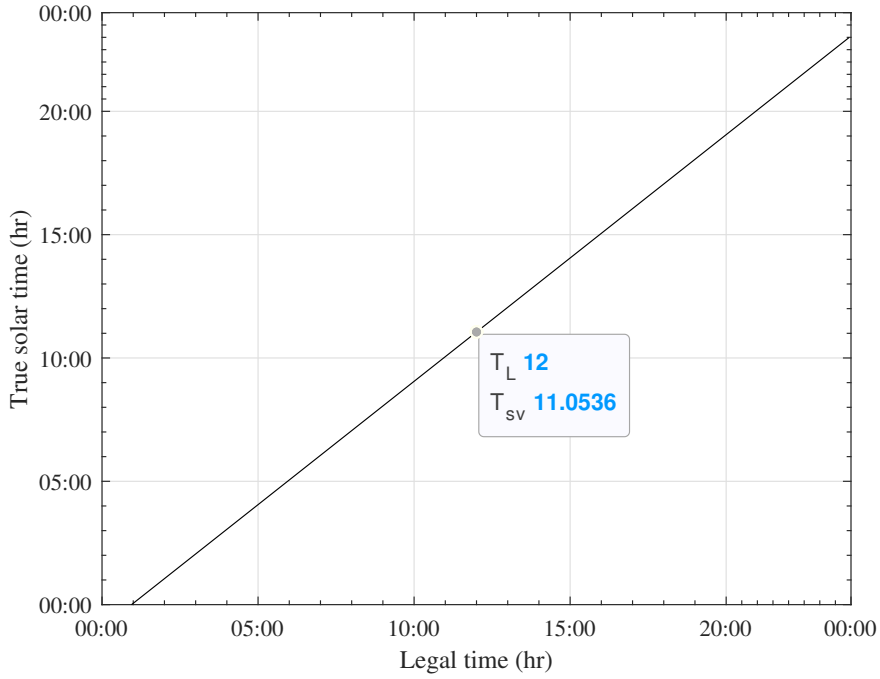


FIGURE 2.3: The difference between true solar time and legal time.

and east, by the imaginary Greenwich line that runs through Greenwich (near London, England).

2.4.1 Latitude

Latitude of a place is an angular value, an expression of the north south position, of the equator of a point on Earth. Theoretically, it has the value 0 ° at the equator up to 90 ° at the poles, it is counted positively from (0 to + 90 °) towards the North and negatively from (0 to -90 °) towards the South. Generally, this quantity is noted φ.

2.4.2 Longitude

Longitude of a place is an angular value, an expression of the East-West positioning of a point on Earth relative to the original meridian. It is therefore a 360 ° angular measurement with respect to a reference meridian, with a range from + 180 ° to -180 ° or 180 ° East to 180 ° West. Generally, this quantity is noted Lon.

2.4.3 Altitude

Altitude expresses a difference between a given point and an average level, most often sea level (or level 0). The vertices are associated with an altitude, calculated by various indirect means (geodesy, triangulation).

2.5 Position of The Sun

The position of the sun is spotted at every moment of the day and year by two different coordinate systems.

2.5.1 Equatorial Coordinates

The movement of the sun is identified relative to the equatorial plane of the earth using two angles (ω, δ)

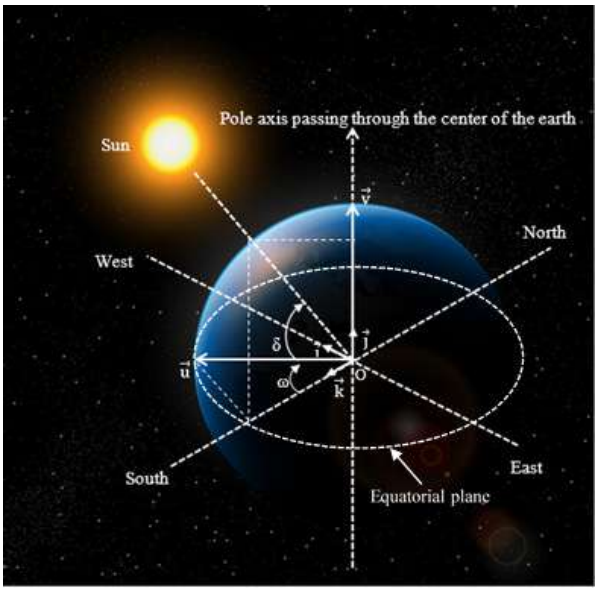


FIGURE 2.4: Sun-Earth angles.

2.5.1.1 Solar Declination

The declination of the sun δ is the angle that the direction of the sun makes with the equatorial plane of the earth. The variation varies from -23,27° at the winter solstice to + 23, 27° at the summer solstice and it is zero at the equinoxes [33].

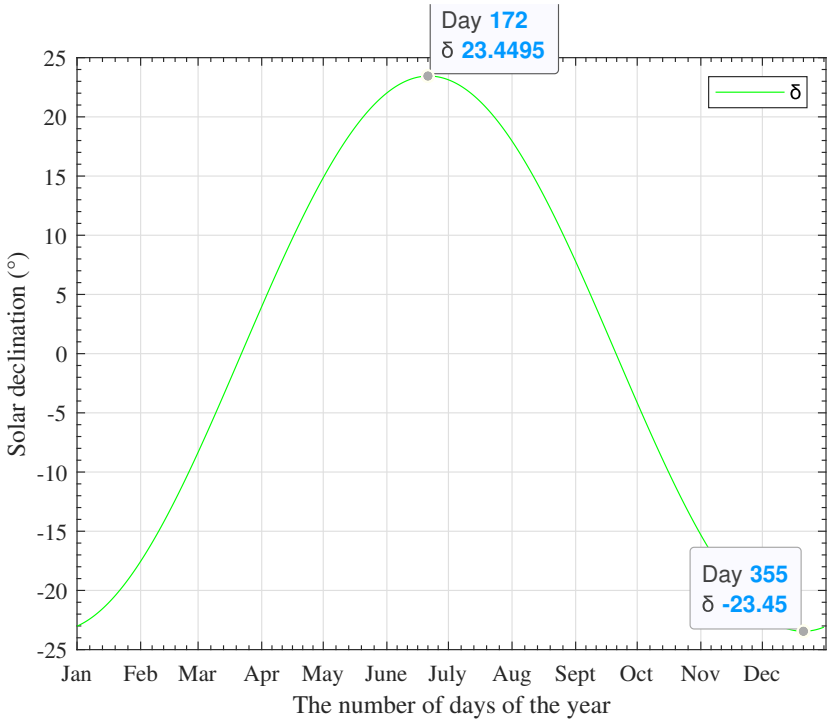


FIGURE 2.5: Variation in solar declination angle as function of the days of the year.

The solar declination is well represented by the following formula:

$$\delta = 23.45 \times \sin\left[\frac{360}{365} \times (N + 284)\right] \tag{2.4}$$

The angle of the solar declination δ is equal 23,45° on the June 21th, which represents the summer solstice, while the value of is equal -23,45° on the December 21th, which represents the winter solstice, and the value of is equal 0 ° on the March 21th and September 21th which represents the spring and autumn equinoxes, respectively.

2.5.1.2 Hour Angle

The hour angle ω being the angle formed by the meridian plane passing through the center of the sun and the vertical plane of the place (meridian) defines the true solar time TST. To calculate the hour angle, Capderou [33] in the Solar Atlas of Algeria , used the following formula:

$$\omega = 15 \times (TST - 12) \tag{2.5}$$

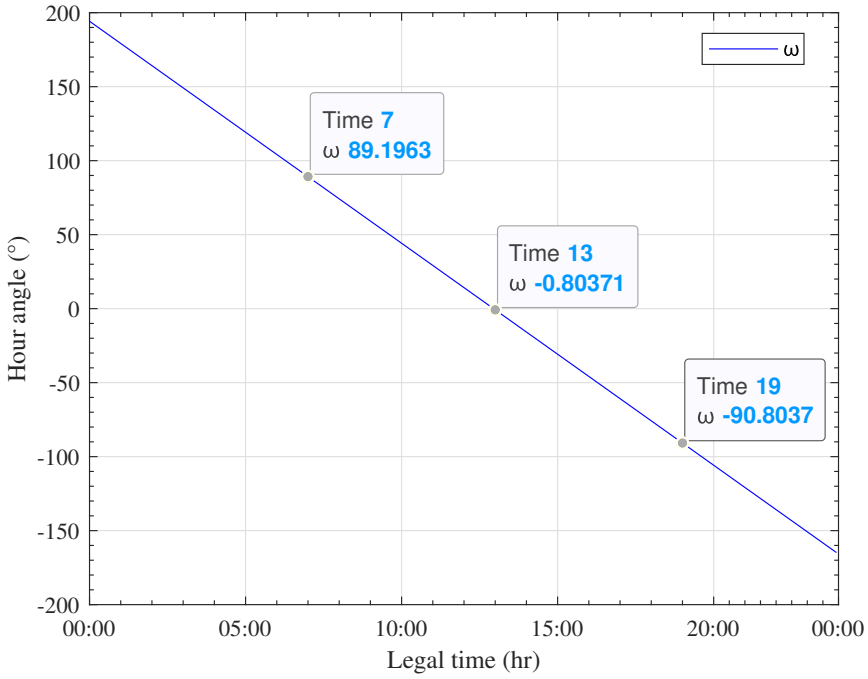


FIGURE 2.6: Hour angle variation as a function of timer.

The hour angle measurement depends on the solar noon, which is positive if it is noon and negative if it is afternoon ω is 0° at midday, -90° at 6 pm and 90° at 6 am, in true solar time, each hour changes it by 15 solar regressions, positive in the morning and negative in the afternoon.

2.5.2 Horizontal Coordinates

The horizontal coordinate system is formed by the plane of the astronomical horizon and the vertical of the place. In this coordinate system, the coordinates are the height h and the azimuth az.

2.5.2.1 Sun Height

The height of the sun h is the angle made, the horizontal plane with the direction of the sun, the value h = 0 corresponds to sunrise and sunset, the height of the sun varies between + 90 ° (zenith) and -90 ° (nadir). The height of the sun is well represented by a well-known formula, which had also been adopted by Capderou [33].

$$h = arc\ \sin\left[\cos\left(\delta\right) \times \cos\left(\varphi\right) \times \cos\left(\omega\right) + \sin\left(\varphi\right) \times \sin\left(\delta\right)\right. \tag{2.6}$$

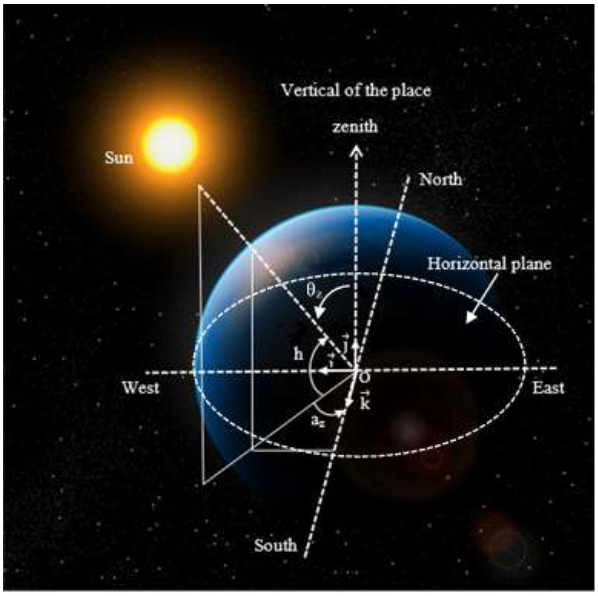


FIGURE 2.7: Horizontal coordinate system.

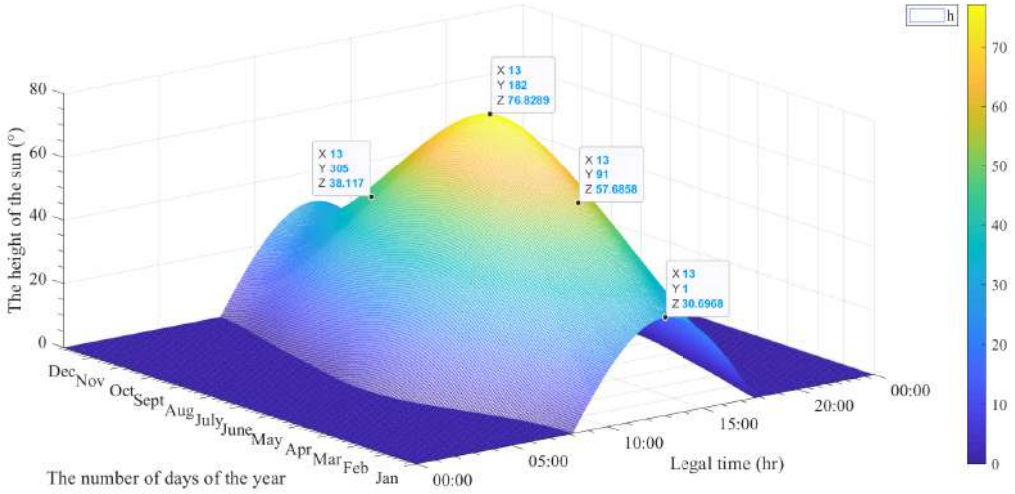


FIGURE 2.8: Variation of the height of the sun - Site: Medea during a day and throughout the year.

2.5.2.2 Azimuth of The Sun

The azimuth of the sun is the angle between the projection of the direction of the sun on the horizontal plane and the south direction. The azimuth angle can be calculated by the following relation [34]:

$$\sin(a_z) = \frac{\cos(\delta).\sin(\omega)}{\cos(h)} \tag{2.7}$$

It is zero at noon T_{SV} and maximum at sunrise and sunset.

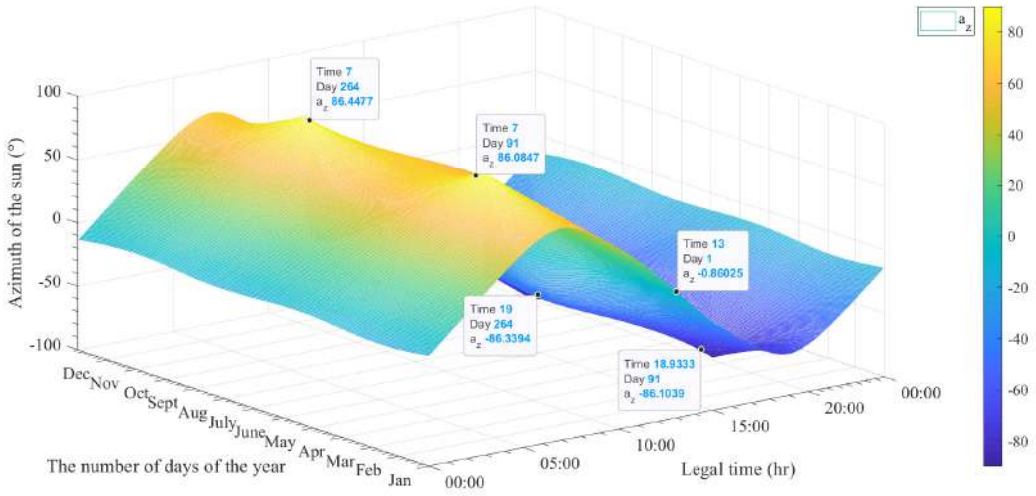


FIGURE 2.9: Variation of azimuth of the Sun - Site: Medea during a day and throughout the year.

2.5.2.3 The Zenith Distance

The zenith distance is the angular distance between the zenith and a point on the celestial sphere, measured along a meridian. It is the complement of the height, that is to say that the zenith distance and the height are complementary angles (in other words their sum is equal to a right angle).

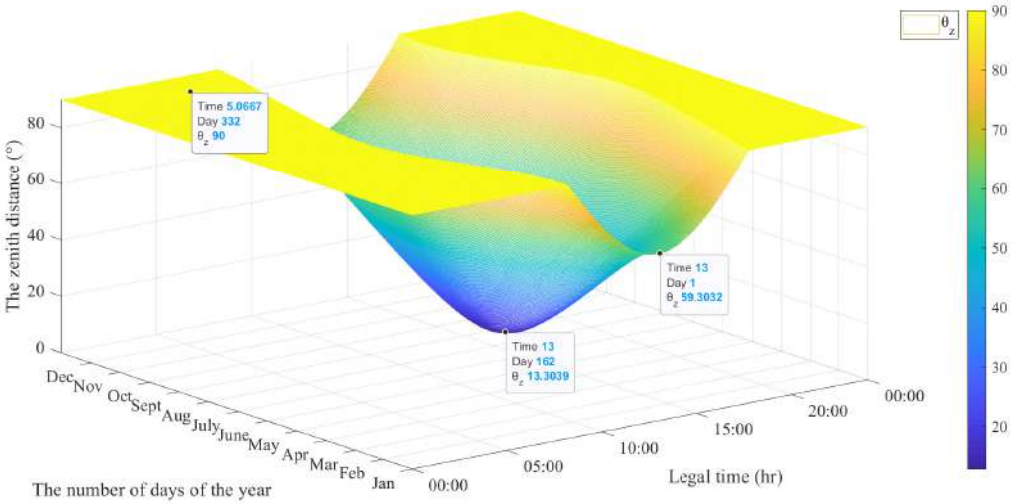


FIGURE 2.10: Variation of the zenith distance - Site: Medea during a day and throughout the year.

$$\theta_z = 90^{\circ} - h \tag{2.8}$$

2.6 Calculation of Solar Radiation

2.6.1 Solar Radiation Outside the Atmosphere

The extraterrestrial solar radiation is a function of the solar constant I_0 and the correction of the distance between the earth and the sun. The solar constant is the energy flux received by a unit surface. In our case, the value that was retained in 1980 is: $I_0 = 1367\ \left(W/m^2\right)$, I_{sc} is [34]:

$$I_{sc} = I_0 \times \left[1 + 0.033 \times \cos\left(\frac{360}{365}\left(N - 3\right)\right)\right] \tag{2.9}$$

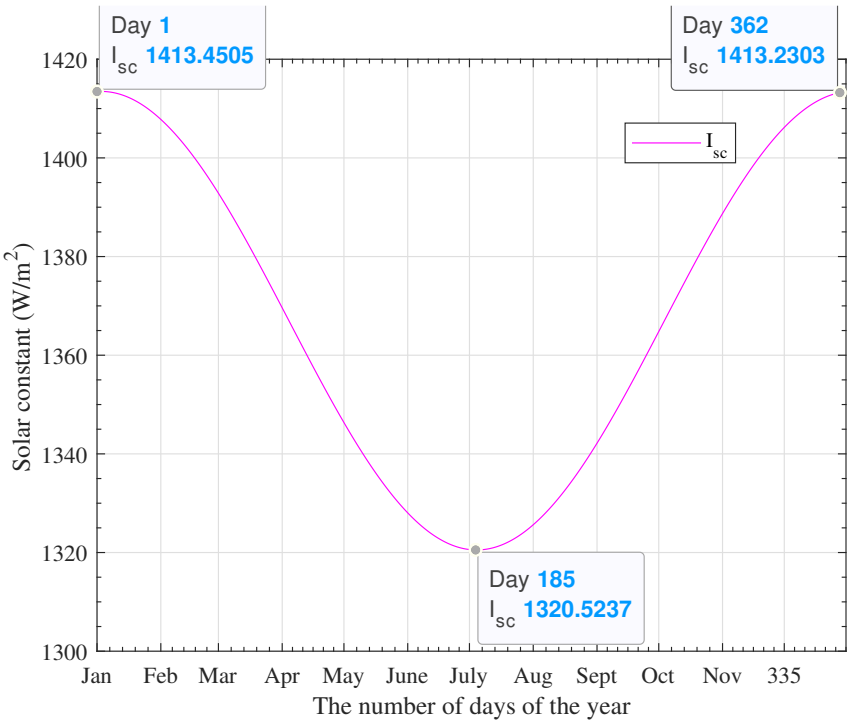


FIGURE 2.11: Annual evolution of the solar constant.

2.6.2 Semi-Empirical Models

Semi-empirical models use mathematical relations as a function of air mass to calculate the effects of the constituents of the atmosphere (integrated across the spectrum) on the attenuation of direct radiation and the creation of diffuse radiation. Several models have been proposed in the literature among which the Bird & Hulstrom model , the Davies & Hay model, the Atwater & Ball model, the Lacis & Hansen model [34, 35].

2.6.2.1 Lacis & Hansen Model

2.6.2.1.1 Calculation of Global Solar Radiation The general formula proposed by Lacis & Hansen for the calculation of global solar radiation on a horizontal plane is given by equation [36, 35]:

$$I_T = I_{sc} \times \cos(\theta_z) \left[\frac{(0.647 - \rho'_s - \alpha_0)}{(1 - 0.0685\rho)} + 0.353 - \alpha_\omega \right] \tag{2.10}$$

I_{SC} is the extraterrestrial solar constant calculated by equation 2.9
θ_z is the zenith angle is determined by equation 2.8

$$\rho'_S = \frac{0.28}{1 + 6.43 \times \cos\theta_Z} \tag{2.11}$$

$\rho'_S$is the soil albedo, the values of which are given in the following table 2.1

TABLE 2.1: Some ground albedo value. [36]

Surface type	Albedo (0 to 1)
Lake surface	0,02 to 0,04
Coniferous forest	0,05 to 0,15
Sea surface	0,05 to 0,15
Dark floor	0,05 to 0,15
Cultures	0,15 to 0,25
Light and dry sand	0,25 à 0,45
Ice	about 0.60
Packed snow	0,40 to 0,70
Fresh snow	0,75 to 0,90
Mirror	1

The coefficient corresponding to the absorption of direct solar radiation by the ozone layer, is calculated by the relation:

$$\alpha_0 = \frac{0.02118\ U_0}{1 + 0.042\ U_0 + 3.2310^{-4}\ U_0^2} + \frac{1.082\ U_0}{(1 + 138.6\ U_0)^{0.805}} + \frac{0.0658\ U_0}{1 + (103.6\ U_0)^3} \tag{2.12}$$

Where U_0 is the thickness of the ozone layer corrected by the optical path of solar radiation through this layer and defined by:

$$U_0 = L \times m_r \tag{2.13}$$

Where m_r is the relative optical air mass given by the following equation :

$$m_r = \left[\cos\theta_z + 0.15(93.885 - \theta_z)^{-1.253}\right]^{-1} \tag{2.14}$$

and, L represents the amount of ozone vertical to the place (thickness of the reduced ozone layer)

$$L = \frac{\left\{235+[150+40\sin(0.9856(N-30))+20\sin(3Lon)]\left\lfloor \sin^2(1.28\varphi)\right\rfloor\right\}}{1000} \tag{2.15}$$

α_W represents the absorption coefficient of direct radiation by water vapor, is given by :

$$\alpha_w = \frac{2.9\ X_W}{(1+141.5\ X_W)^{0.635}+5.925\ X_W} \tag{2.16}$$

X_W is the thickness of condensed water corrected by optical path of the radiation through this layer, given by:

$$X_W = m_a \times U_W \tag{2.17}$$

U_W is the thickness of the condensed water vertically from the place (cm) and is given by:

$$U_W = \frac{0.493}{T} HR \times \exp\left(26.23 - \frac{5416}{T}\right) \tag{2.18}$$

With m_a the corrected air mass expressed by:

$$m_a = m_r\left(\frac{P}{1013}\right)^{0.75} \times \left(\frac{273}{T}\right)^{0.5} \tag{2.19}$$

P is the atmospheric pressure (mbar). It can be calculated from the following relation:

$$P = P_0 \exp\left(-0.0001184 \times z\right) \tag{2.20}$$

P_0 is the atmospheric pressure at sea level P_0= 1013 (mbar).
z is the altitude of the site (m) above sea level.
T is the ambient temperature (K).
RH is the relative humidity (%).

2.6.2.2 Davies & Hay Model

The model proposed by Davies & Hay in 1976 allows the determination of the components of solar radiation on the ground as a function of the different

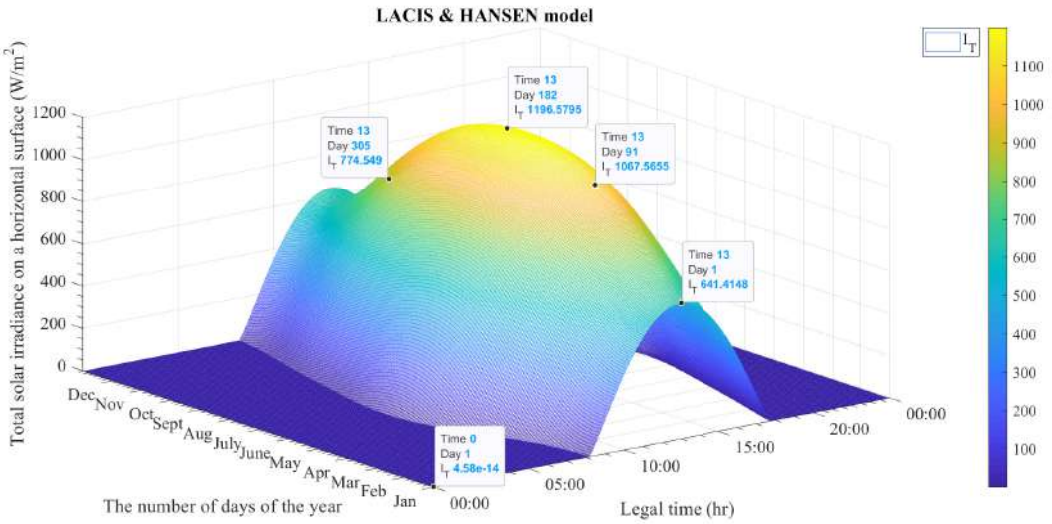


FIGURE 2.12: Solar radiation calculated by the Lacis & Hansen model - Site: Medea during a day and throughout the year.

transmission coefficients of the elements constituting the atmosphere at any time of the day [36, 35].

2.6.2.2.1 Calculation of Direct Radiation

$$I = I_{SC} \times [(1 - \alpha_0) . \tau_r - \alpha_W] \tau_a \times \cos \theta_z \tag{2.21}$$

$\alpha_0$is the coefficient corresponding to the absorption of direct solar radiation by the ozone layer, is calculated by the relation 2.12 τ_r is the transmission coefficient after molecular diffusion or Rayleigh diffusion calculate by the following relations :

$$\tau_r = 0.972\text{-}0.08262\mathrm{m}_a + 0.00933 m_a^2 - 0.00095 m_a^3 + 0.000437 m_a^4 \tag{2.22}$$

m_a is the corrected air mass expressed by the following relation :

$$m_a = \frac{P}{P_0} m_r = \frac{exp(-0.0001184 \times z)}{\cos(\theta_z) + 0.15(93.885\text{-}\theta_z)^{-1.253}} \tag{2.23}$$

The absorption coefficient of direct radiation by water vapor $\alpha_W$is given by equation 2.16 The transmission coefficient after diffusion by aerosols $\tau_a$is proposed by MÄCHLER according to the equation :

$$\tau_a = (0.12445\,\alpha - 0.0162) + (1.003 - 0.125\alpha)\exp\left[-\beta m_a\,(1.089{+}0.5123)\right] \tag{2.24}$$

and $\beta \prec 0.5$.
Such as: α and β are respectively the coefficient characterizing the visibility of the sky and the coefficient of cloudiness of Angstrom. Their calculation is based on the experimental determination of two attenuation coefficients $k_{a\lambda 1}$ and $k_{a\lambda 2}$corresponding to the wavelengths where absorption by water vapor does not occur λ_1= 380 (nm)and λ_2= 500 (nm), Knowing that is close to 0 for small particles, increases with size particles and reaches 4 for large particles. In our work, we take . The coefficient β =0.02 for a very pure sky (deep blue) and 0.2 for a polluted sky (milky blue) 2.2.

TABLE 2.2: Parameters α and β according to different states of the atmosphere. [34]

Atmosphere	α	β
Very pure	1.3	0.01
Pure	1.3	0.1
Polluted	1.3	0.2
very polluted	1.3	0.4

2.6.2.2.2 Calculation of Diffuse Radiation The diffuse radiation on a horizontal plane is the sum of the three diffuse components: D_r, D_a and D_m.

2.6.2.2.3 Diffuse Radiation From Rayleigh Scattering The diffuse radiation from Rayleigh scattering is expressed by the following relation:

$$D_r = I_{SC}\tau_0\tau_a\,(1-\tau_r)\,0.5\times\cos\theta_z \tag{2.25}$$

which $\tau_0$is the transmission coefficient after absorption by ozone:

$$\tau_0 = 1 - \alpha_0 \tag{2.26}$$

α_0.is the coefficient corresponding to the absorption of direct solar radiation by the ozone layer, is calculated by the relation 2.12

2.6.2.2.4 Diffuse Radiation After Diffusion by Aerosols Diffuse radiation after aerosol diffusion is given by:

$$D_a = I_{SC}\left(\tau_0\tau_r - \alpha_\omega\right) \times \left[F_C \times \omega_0\left(1-\tau_a\right)\right]\cos\theta_z \tag{2.27}$$

With $\varpi_0$whom is the albedo of dispersion of the atmosphere. In practice, determining this coefficient is almost impossible. Indeed, it depends on the nature, the shape, and the optical properties of the particles in suspension. a value of ϖ_0 is generally assigned independent of the wavelength. For urban industrial regions, ϖ_0 is 0.6, and for rural agricultural regions, it is 0.9. and, F_C which is the direct dispersion coefficient of the atmosphere 2.3.

TABLE 2.3: Values of factor F_C as a function of zenith distance [34]

θ_z	0	10	20	30	40	50	60	70	80	85
F_C	0,92	0,92	0,90	0,90	0,90	0,85	0,78	0 ,68	0,60	0,50

2.6.2.2.5 The Diffuse Radiation Resulting From The Phenomenon Of Multi Reflection Earth Atmosphere The expression of the diffuse radiation resulting from the multi-reflection phenomenon is given by equation

$$D_m = \frac{(I+D_a+D_r)\times\rho\times\rho'_a}{(1-\rho\times\rho'_a)} \tag{2.28}$$

Whereρ'_a is the clear sky albedo of the site considered, which is given by the relation:

$$\rho'_a = 0.0685 + 0.17\,\omega_0 \times (1-\tau'_a) \tag{2.29}$$

With, the constraint on τ_a indicating that the transmission coefficient of solar radiation after diffusion by aerosols should be calculated for an air mass value equal to 1.66 $\left(\frac{P}{P_0}\right)$. The factor 0.17 represents (1 - F_C) for θ_z= 53 ° and (1 - F_C), is the backscatter coefficient.

2.6.2.2.6 Calculation of Global Radiation: The global radiation on a horizontal plane is calculated by:

$$I_T = (I\ +\ Dr + Da)\left(\frac{1}{1-\rho\rho'_a}\right) \tag{2.30}$$

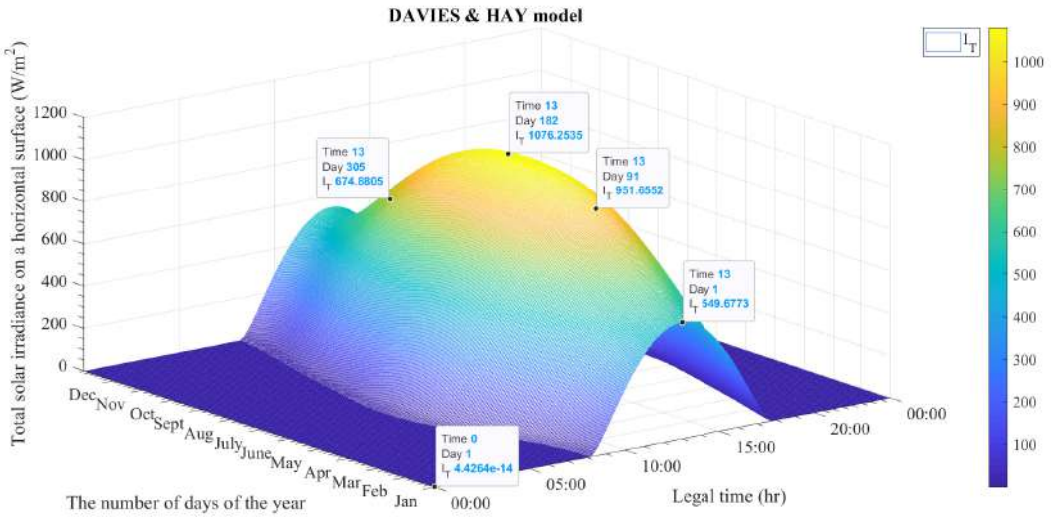


FIGURE 2.13: Solar radiation calculated by the Davies & Hay model - Site: Medea during a day and throughout the year

2.6.2.3 Bird & Hulstrom Model

In 1981, Bird & Hulstrom [34] developed a mathematical model which makes it possible to calculate the solar radiation incident on the ground. This model takes into account the scattering and absorption effects that solar radiation undergoes when it crosses the atmosphere. It is based on the determination of the transmission coefficients of the various atmospheric constituents. These coefficients require the availability of current meteorological parameters (relative humidity, ambient temperature, atmospheric pressure,) and geographic parameters (latitude, longitude and altitude).

2.6.2.3.1 Direct Radiation The illumination due to direct radiation on a horizontal plane is given by the relation [36, 35]:

$$I = 0.9751 \times I_{SC} \times \tau_r \times \tau_g \times \tau_0 \times \tau_W \times \tau_a \times \cos(\theta_z) \tag{2.31}$$

Where, the absorption coefficient by the ozone layer τ_0 is given by:

$$\tau_0 = 1 - 0.1611 \times U_0 \times (1.0 + 139.48 \times \mathrm{U}_0)^{-0.3035} \times 0.002715 \times \mathrm{U}_0 \times \left(1 + 0.044 \times U_0 + 0.0003 \times U_0^2\right)^{-1} \tag{2.32}$$

and U_0 is the thickness of the ozone layer corrected by the optical path of solar radiation through this layer and defined by equation 2.13

The transmission coefficient after absorption of solar radiation by water vapor is given by:

$$\tau_\omega = 1 - 2.4959 \times U_W \times \left[(1 + 79.03 \times U_W)^{0.6828} + 6.385 \times U_W\right]^{-1} \quad (2.33)$$

$U_W$is the thickness of water condensed vertically from the place (cm) given by equation 2.18

The transmission coefficient after absorption by permanent gases CO_2 and O_2 is expressed as a function of the air mass corrected using equation :

$$\tau_g = \exp\left(-0.0127 \times m_a^{0.26}\right) \quad (2.34)$$

Where, $m_a$is the corrected air mass expressed by the relation 2.19

The transmission coefficient after molecular diffusion is also expressed as a function of the air mass by:

$$\tau_r = \exp\left[\text{-}0.0903 \times m_a^{0.84}\left(1.0 + m_a - m_a^{1.01}\right)\right] \quad (2.35)$$

The transmission coefficient after diffusion by aerosols can be calculated by:

$$\tau_a = \exp\left[-k_a^{0.873} \times m_a^{0.9108} \times \left(1.0 + k_a - k_a^{0.7088}\right)\right] \quad (2.36)$$

Where:

$$k_a = 0.2758 \times k_{a\lambda/\lambda=0.38\mu m} + 0.35 \times k_{a\lambda/\lambda=0.5\mu m} \quad (2.37)$$

$k_{a\lambda/\lambda=0.38\mu m}$ and $k_{a\lambda/\lambda=0.5\mu m}$ are two attenuation coefficients determined from experimental measurements deduced from equation :

$$\begin{cases} k_{\alpha\lambda}\left(\lambda = 0.38\mu m\right) = \beta(0.38)^{-\alpha} \\ k_{\alpha\lambda}\left(\lambda = 0.50\mu m\right) = \beta(0.50)^{-\alpha} \end{cases} \quad (2.38)$$

Where, α is the particle size distribution coefficient and β the atmospheric cloud coefficient established by Angstrom. These values allowed us to calculate:

2.6.2.3.2 Diffuse Radiation: Also in this model, the diffuse radiation on a horizontal plane is the sum of the three diffuse components due to the various types of diffusion of solar radiation by the atmospheric layer:

$$D = D_r + D_a + D_m \tag{2.39}$$

The diffuse radiation resulting from Rayleigh diffusion is given by:

$$D_r = 0.79 \times I_{SC} \times \cos(\theta_z) \times \tau_0 \times \tau_g \times \tau_W \times \tau_{aa} \times 0.5 \times \frac{(1-\tau_r)}{\left(1-m_a+m_a^{1.02}\right)} \tag{2.40}$$

Whereτ_{aa} is given by the following expression:

$$\tau_{aa} = 1 - (1-\omega_0) \times \left(1 - m_a + m_a^{1.06}\right) \times (1-\tau_a) \tag{2.41}$$

andω_0, is the unit reflection coefficient relative to the diffusion by aerosols. In this model, Bird & Hulstrom recommended ω_0 = 0.90.

The diffuse radiation after diffusion by aerosols is given by:

$$D_a = 0.79 \times I_{SC} \times \cos(\theta_z) \times \tau_0 \times \tau_W \times \tau_{aa} \times F_C \times \frac{(1-\tau_{as})}{\left(1-m_a+m_a^{1.02}\right)} \tag{2.42}$$

Where F_C, is the dispersion coefficient of the atmosphere.F_C = 0.84 is the value recommended by this model.

$\tau_{as}$is given by the following relation:

$$\tau_{as} = \frac{\tau_a}{\tau_{aa}} \tag{2.43}$$

The diffuse due to the phenomenon of multi-reflection earth atmosphere is given by:

$$D_m = \frac{(I+D_a+D_r)\times\rho\times\rho'_a}{\left(1-\rho_g\times\rho'_a\right)} \tag{2.44}$$

With $\rho$is the terrestrial albedo, and $\rho'_a$is the clear sky albedo given by:

$$\rho'_a = 0.0685 + (1-F_C)(1-\tau_{as}) \tag{2.45}$$

2.6.2.3.3 Global solar radiation The global radiation on a horizontal plane is the sum of the two direct and diffuse solar components:

$$I_T = I + D \tag{2.46}$$

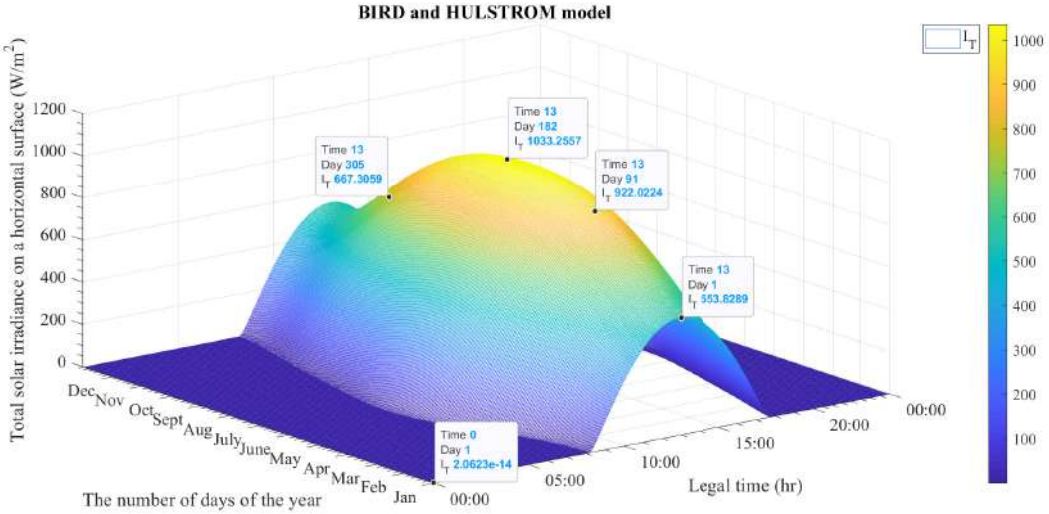


FIGURE 2.14: Solar radiation calculated by the Bird & Hulstrom model - Site: Medea during a day and throughout the year

2.6.2.4 Atwater & Ball Model

2.6.2.4.1 Global Solar Radiation The general formula proposed by Atwater & Ball for the calculation of global solar radiation is given by the mathematical equation [36, 35]:

$$I_T = I_{SC} \times \cos\theta_z \times \left[\frac{(T_M - \alpha_W) \times \tau_a}{(1 - 0.0685 \times \rho)}\right] \tag{2.47}$$

Where T_M is given by the following relation:

$$T_M = 1.021\text{-}0.0824 \times \left[m_0 \left(949 \times 10^{-10} \times P + 0.051\right)\right]^{0.5} \tag{2.48}$$

$m_0$is the mass of ozone air given by:

$$m_0 = \frac{35}{(1224 \cos^2(\theta_z) + 1)^{0.5}} \tag{2.49}$$

The absorption coefficient of direct radiation by water vapor is given by equation:

$$a_W = 0.077 \times (U_\omega \times m_0)^{0.3} \tag{2.50}$$

U_w is the thickness of water condensed vertically from the place (cm) given by equation 2.18

The transmission coefficient after diffusion by aerosols is provided by the following relation:

$$\tau_a = \exp\left(-k_a \times m_a\right) \tag{2.51}$$

$k_a$is determined by equation 3.71

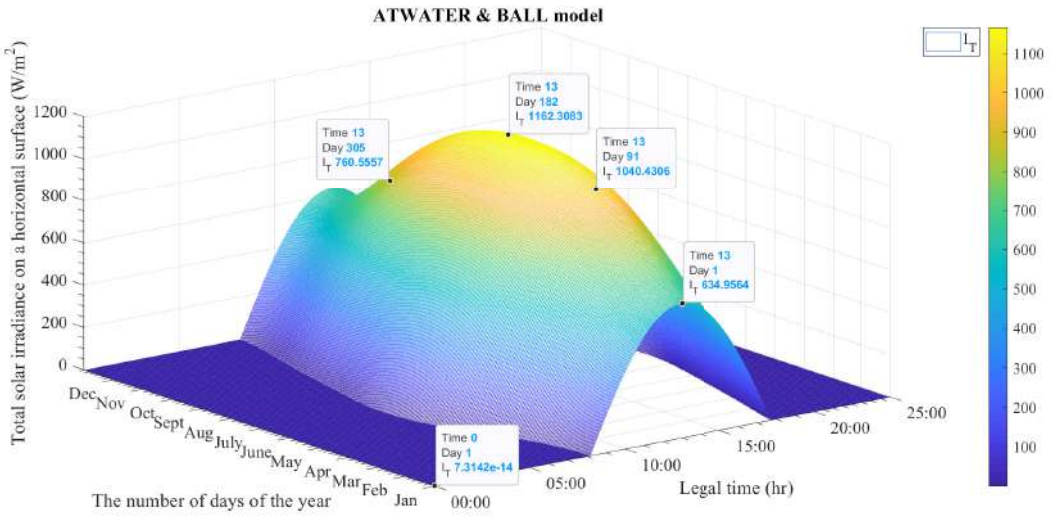


FIGURE 2.15: Solar radiation calculated by the Atwater & Ball model - Site: Medea during a day and throughout the year

2.6.3 Comparison of experimental and calculated results for solar radiation

Figure 2.16 shows a comparison between the measured and calculated results of solar radiation according to the four models of the site of Ouargla by date 02/05/2005 [37].The geographical characteristics of the studied site are given in table 2.4. It is clear that the Davies Hay model and the Bird & Hulstrom model give a good estimate of the solar radiation. The results obtained by the two previous models approach with great accuracy the real data.

TABLE 2.4: Geographical coordinates of the site used

Site	Dated	Latitude	Longitude	Altitude
Ouargla	02/05/2005	32.65 (°)	5.82 (°)	135 (m)

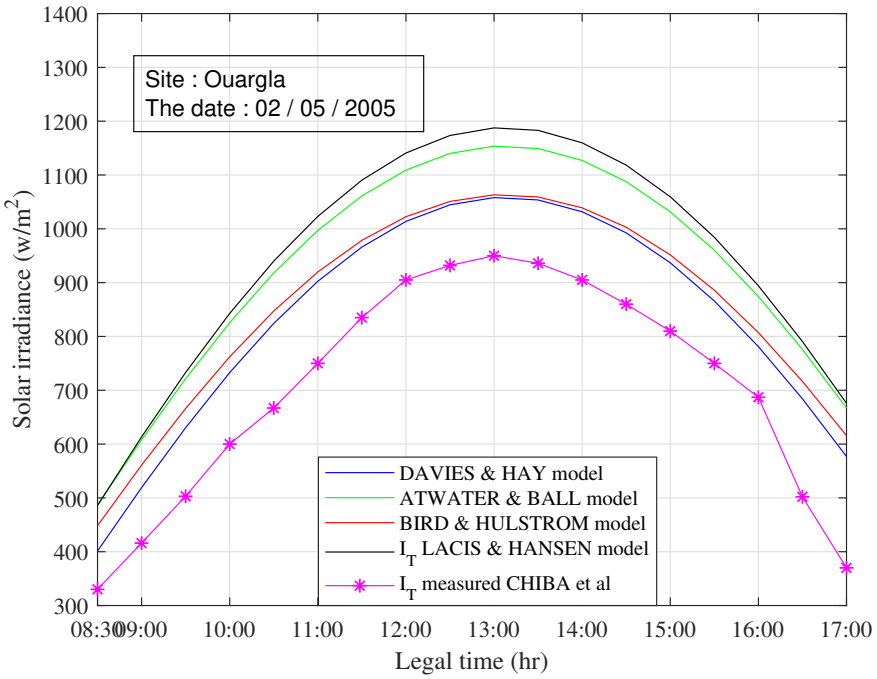


FIGURE 2.16: A comparison between the measured and calculated results of solar radiation according to the four models of the site of Ouargla

Chapter 3

Thermal Analysis of Shallow Solar Ponds

3.1 Introduction

The performance of the shallow solar pond SSP is highly dependent on the amount of solar energy input into the SSP and the amount of heat loss from the SSP. The pond water and absorber plate are heated by absorbing the incident solar radiation. The thermal losses are due to the temperature difference between the pond and the surrounding environment, which is divided into four classes: front losses, posterior losses, collateral losses, heat losses due to heat transfer fluid in the pond. This chapter aims to propose a mathematical model that allows the development of a new device to receive and store solar energy by converting it into thermal energy using a pond filled with water. This chapter is divided into three sections:

- SSP under the batch mode of heat extraction
- SSP under the open cycle and continuous mode of heat extraction
- carrier fluid description

3.2 SSP Under the Batch mode of Heat Extraction

The first section aims to develop a mathematical model based on the thermal equilibrium equations of a SSP operating under the batch mode for heat extraction as shown in the figure 3.1, in order to choose the best values for the parameters that allow to provide the best thermal performance.These parameters are :

- The depth of the pond
- The distance between the glass covers
- The thickness of the insulating material

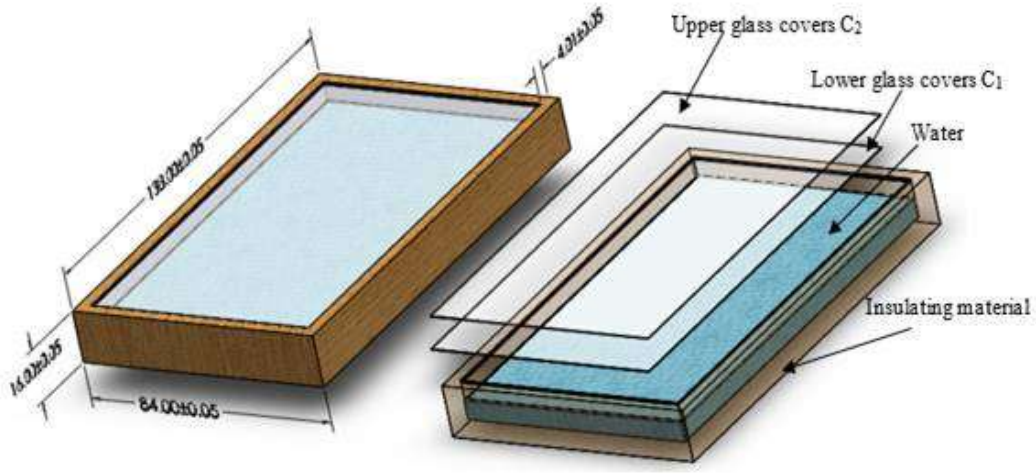


FIGURE 3.1: A schematic diagram showing the studied SSP operating under the batch mode of heat extraction.

3.2.1 Heat Balance Equations

In order to write the energy balance equations for the various elements of the system , the following assumptions are made:

- The SSP is fitted with two glass covers
- The area of the two glass covers, the surface area of the water and the area of the absorber plate are equals.
- The SSP is thermally insulated
- The pond water comes into contact with the surface of the lower glass cover to prevent the evaporative heat transfer between the water surface and the lower glass cover
- There is no thermal gradient in the pond water due to its shallow depth
- The heat capacities of the glass covers , and insulation are negligible compared to that of the pond water
- The heat flow received by the SSP is a function of time

- The temperatures of the SSP components are a function of time
- The wind speed on the face of the SSP is assumed to be constant

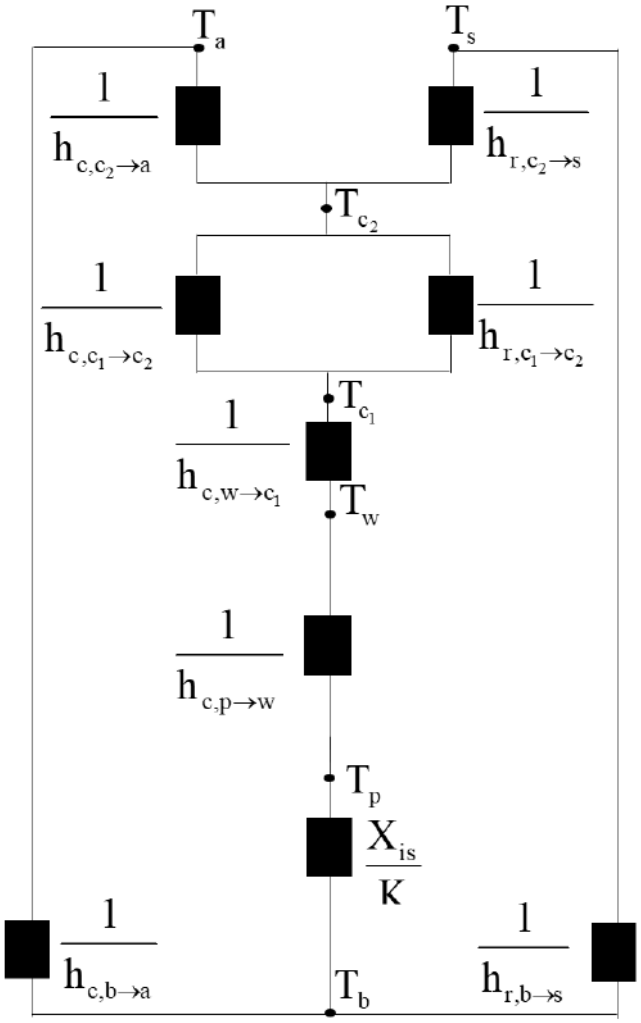


FIGURE 3.2: Diagram showing the heat transfer mechanisms in SSP operating under a batch mode for heat extraction.

A schematic diagram of the energy flows in terms of the various heat transfer coefficients between the different elements of the SSP operating under a batch mode for heat extraction is presented in figure 3.2. Based on these assumptions and figure 3.2, the energy balance equations for the different elements of the SSP may be written as follows:

3.2.1.1 Energy Balance Equations for The Upper Glass Cover:

$$\begin{aligned} &I_T \alpha_c A_c + h_{c,c_1 \to c_2} A_c \left(T_{c_1} - T_{c_2}\right) + h_{r,c_1 \to c_2} A_C \left(T_{c_1} - T_{c_2}\right) \\ &= h_{c,c_2 \to a} A_c \left(T_{c_2} - T_a\right) + h_{r,c_2 \to s} A_c \left(T_{c_2} - T_s\right) \end{aligned} \tag{3.1}$$

Where :
$I_T$is the solar radiation (W/m^2).
α_c is the absorptivity of the glass cover .
A_c is the area of the glass cover (m^2).
$h_{C,c_1\to c_2}$is the convective heat transfer coefficient between the lower and upper glass covers(W/m^2K), it is can be calculated using the following correlation:

$$h_{C,c_1\to c_2} = \frac{\overline{Nu_{X_g}}\times K_a}{X_g} \tag{3.2}$$

Where :
K_a is the thermal conductivity of the air (W/mK).
X_g is the gap between the glass covers (m).
$\overline{Nu}$ is the average Nusselt number, it can be calculated as follows [38]:

$$\overline{Nu_{X_g}} = 1 + 1.44\left[1 - \frac{1708}{Ra_{X_g}}\right]^* + \left[\left(\frac{Ra_{X_g}}{5830}\right)^{1/3} - 1\right]^* \tag{3.3}$$

for $1700 \leq Ra \leq 10^8$.
where the notation $[]^*$ indicates that if the quantity inside the bracket is negative the quantity is to be taken as zero.
Ra is the Rayleigh number.

$$Ra = Gr\,\mathrm{Pr} \tag{3.4}$$

Gr is the Grashof number:

$$Gr = \frac{\beta g L^3 \Delta T}{\nu^2} \tag{3.5}$$

β is the temperature coefficient $(1/K)$.
g is the acceleration due to gravity $\left(m/s^2\right)$.
Pr is the Prandtl number:

$$\mathrm{Pr} = \frac{C_p\mu}{K} \text{ or } \frac{\nu}{\alpha} \tag{3.6}$$

Where:
C_P is the specific heat $(J/\ Kg\ K)$.
μ is the absolute viscosity (Ns/m^2) .
K is the thermal conductivity (W/mK).
ν is the kinematic viscosity (m^2/s).
α is the thermal diffusivity (m^2/s),it can be calculated as follows:

$$\alpha = \frac{K}{\rho C_P} \tag{3.7}$$

With :

ρ is the mass density (Kg/m^3)..

$h_{R,c_1\to c_2}$is the radiative heat transfer coefficient between the lower and upper glass covers (W/m^2K), it is can be calculated using the following correlation [39]:

$$h_{R,c_1\to c_2} = \frac{\sigma\left(T_{c_1}^2+T_{c_2}^2\right)\left(T_{c_1}+T_{c_2}\right)}{\frac{2}{\varepsilon_C}-1} \tag{3.8}$$

σ is Stefan Boltzmann constant (W/m^2K^4).

ε_C is the emissivity of glass cover.

$h_{C,c_2\to a}$ is the convective heat transfer coefficient from the upper glass cover to the ambient air (W/m^2K),it is can be calculated using the following correlation [21]:

$$h_{C,c_2\to a} = 5.7{+}3.8 \times \mathrm{V} \tag{3.9}$$

V is the wind speed (m).

$h_{R,c_2\to s}$ is the radiative heat-transfer coefficient from the upper glass cover to the ambient air (W/m^2K), it is can be calculated using the following correlation [39]:

$$h_{R,c_2\to s} = \varepsilon_C\sigma\left(T_{c_2}^2+T_s^2\right)\left(T_{c_2}+T_s\right) \tag{3.10}$$

T_S is the sky temperature (K), and it is calculated using the following formula:

$$T_s = 0.0052T_a^{1.5} \tag{3.11}$$

Where T is the ambient air temperature (K).

3.2.1.2 Energy Balance Equations for The Lower Glass Cover:

$$\begin{aligned} &I_T\tau_c\alpha_c A_c + h_{c,w\to c_1}A_w\left(T_w - T_{c_1}\right) = h_{c,c_1\to c_2}A_c\left(T_{c_1}-T_{c_2}\right) \\ &+h_{r,c_1\to c_2}A_c\left(T_{c_1}-T_{c_2}\right) \end{aligned} \tag{3.12}$$

Where τ_c is transmissivity of the glass cover.

$h_{C,w\to c_1}$ is the convective heat transfer coefficient from the pond water to the lower glass covers (W/m^2K),it is can be calculated as:

$$h_{C,w\to c_1} = \frac{\overline{Nu_{X_W}}\times K_W}{X_W} \tag{3.13}$$

Where $\overline{Nu_{X_W}}$is the average Nusselt number, it can be calculated as follows [38]:

$$\overline{Nu_{X_W}} = 1 + 1.44\left[1 - \frac{1708}{Ra_{X_W}}\right]^* + \left[\left(\frac{Ra_{X_W}}{5830}\right)^{1/3} - 1\right]^* + 2\left[\frac{Ra_{X_W}^{1/3}}{140}\right]\left[1 - \ln\left(\frac{Ra_{X_W}^{1/3}}{140}\right)\right] \tag{3.14}$$

$X_W$is the depth of pond water (m).

3.2.1.3 Energy Balance Equations for The Absorber Plate:

$$I_T \tau_c^2 \tau_w \alpha_p A_p = h_{c,p\to w} A_p \left(T_p - T_w\right) + U_b A_p \left(T_P - T_a\right) \tag{3.15}$$

Where:
α_p is the absorptivity of the absorber plate .
A_p is the area of the absorber plate (m^2).
$h_{c,p\to w}$ is convective heat-transfer coefficient between the absorber plate and the pond water (W/m^2K).
U_b is the bottom loss-coefficient (W/m^2K), it can be calculated as follows:

$$U_b = \frac{K_{is}}{x_{is}} \tag{3.16}$$

3.2.1.4 Energy Balance Equations for The Pond Water

$$\begin{aligned} &I_T \tau_c^2 \alpha_w A_w + h_{C,p\to w} A_p \left(T_p - T_w\right) = m_w C_{p_w} \left(\frac{dT_w}{dt}\right) \\ &+h_{C,w\to c_1} A_w \left(T_w - T_{c1}\right) + U_s A_s \left(T_w - T_a\right) \end{aligned} \tag{3.17}$$

Where:
α_w is the absorptivity of the pond water.
A_w is the area of the pond water (m^2).
m_w is mass of the pond water (Kg).
C_w is specific heat of water (J/KgK).
Based on equations 3.1,3.12 and 3.15, it is possible to calculate:
Temperature of the upper glass cover:

$$T_{c_2} = \frac{I_T \alpha_c + \left(h_{c,c_1\to c_2} + h_{r,c_1\to c_2}\right) T_{c_1} + h_{r,c_2\to s} T_s + h_{c,c_2\to a} T_a}{\left(h_{c,c_1\to c_2} + h_{r,c_1\to c_2} + h_{r,c_2\to s} + h_{c,c_2\to a}\right)} \tag{3.18}$$

Temperature of the lower glass cover:

$$T_{c_1} = \frac{h_{c,w\to c_1} A_w T_w + A_c\left[I_T \tau_c \alpha_c + T_{c_2}\left(h_{c,c_1\to c_2} + h_{r,c_1\to c_2}\right)\right]}{h_{c,w\to c_1} A_w + A_c\left(h_{c,c_1\to c_2} + h_{r,c_1\to c_2}\right)} \tag{3.19}$$

Temperature of the absorber plate:

$$T_p = \frac{I_T \tau_c^2 \tau_w \alpha_p + h_{c,p\to w} T_w + U_b T_a}{h_{c,p\to w} + U_b} \tag{3.20}$$

By replacing T_{c_1} and T_p by using equations 3.19, 3.20 equation 3.17 can be simplified as follows:

$$M\left(\frac{dT_w}{dt}\right) + aT_w = f(t) \tag{3.21}$$

The method of integrating factor has been used for solving equation 3.21, The solution of equation 3.21, using the initial condition $T_w(t=0) = T_{w_i}$ is:

$$T_w = \frac{f(t)}{a} + \left(T_{wi} - \frac{f(t)}{a}\right) \exp^{\left(\frac{-at}{M}\right)} \tag{3.22}$$

Where:

$$\begin{aligned} a = {} & h_{C,p\to w} A_p + U_s A_s + h_{C,w\to c_1} A_w - \frac{h_{C,p\to w}^2 A_p}{h_{C,p\to w} + U_b} \\ & - \frac{\left(h_{C,w\to c_1} A_w\right)^2}{h_{C,w\to c_1} A_w + A_c\left(h_{C,c_1\to c_2} + h_{R,c_1\to c_2}\right)} \end{aligned} \tag{3.23}$$

and

$$\begin{aligned} f(t) = {} & I_T \tau_c^2 \alpha_w A_w + h_{C,p\to w} A_p \left[\frac{I_T \tau_c^2 \tau_w \alpha_p + U_b T_a}{h_{C,p\to w} + U_b}\right] \\ & + h_{C,w\to c_1} A_w \left[\frac{I_T \tau_c \alpha_c + T_{c_2} A_c\left(h_{C,c_1\to c_2} + h_{R,c_1\to c_2}\right)}{h_{C,w\to c_1} A_w + A_c\left(h_{C,c_1\to c_2} + h_{R,c_1\to c_2}\right)}\right] + U_s A_s T_a \end{aligned} \tag{3.24}$$

and

$$M = m_w C_w \tag{3.25}$$

where m_w is the water mass within the pond (Kg) and is calculated from:

$$m_w = \rho X_w A_w \tag{3.26}$$

The rate of thermal energy collection Q_{coll}, is given by:

$$Q_{coll} = \frac{M(T_{wpf} - T_{wpi})}{\Delta t} \tag{3.27}$$

3.3 SSP Under the Open Cycle and Continuous Mode of Heat Extraction:

The second section aims to develop a mathematical model based on the thermal equilibrium equations for SSP operating under the open mode and continuous heat extraction as shown in figure 3.3, in order to choose the best values for the parameters that allow providing the best thermal performance for the SSP.These parameters are:

- The length of the heat exchanger
- The diameter of the heat exchanger
- The mass flow rate of the heat transfer fluid

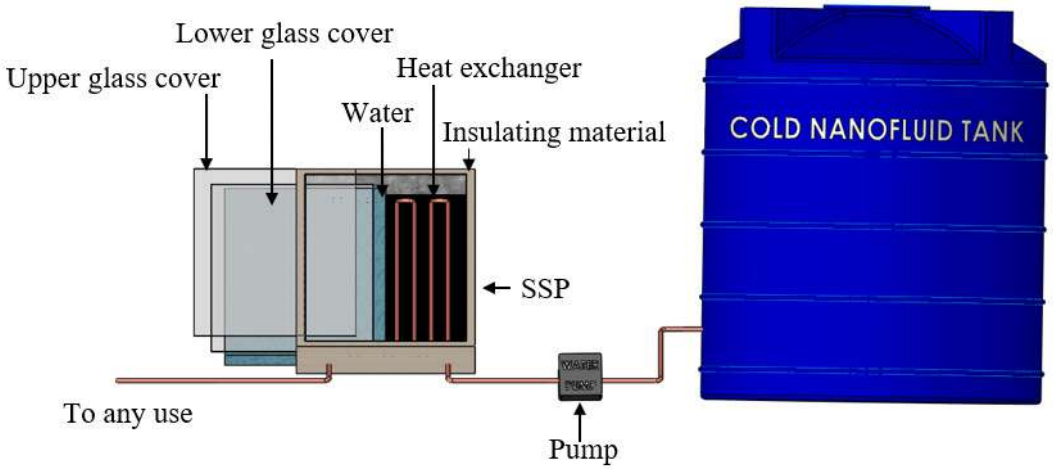


FIGURE 3.3: A schematic diagram showing the studied SSP operating under the open cycle mode of heat extraction.

As previously mentioned, in order to write the equations of the thermal equilibrium for the SSP there are several hypotheses which are:

- The heat exchanger is welded to the bottom of the SSP
- The temperature of the heat transfer fluid at the inlet of the heat exchanger is assumed to be constant
- The mass flow rate of the heat transfer fluid is assumed to be constant throughout the day

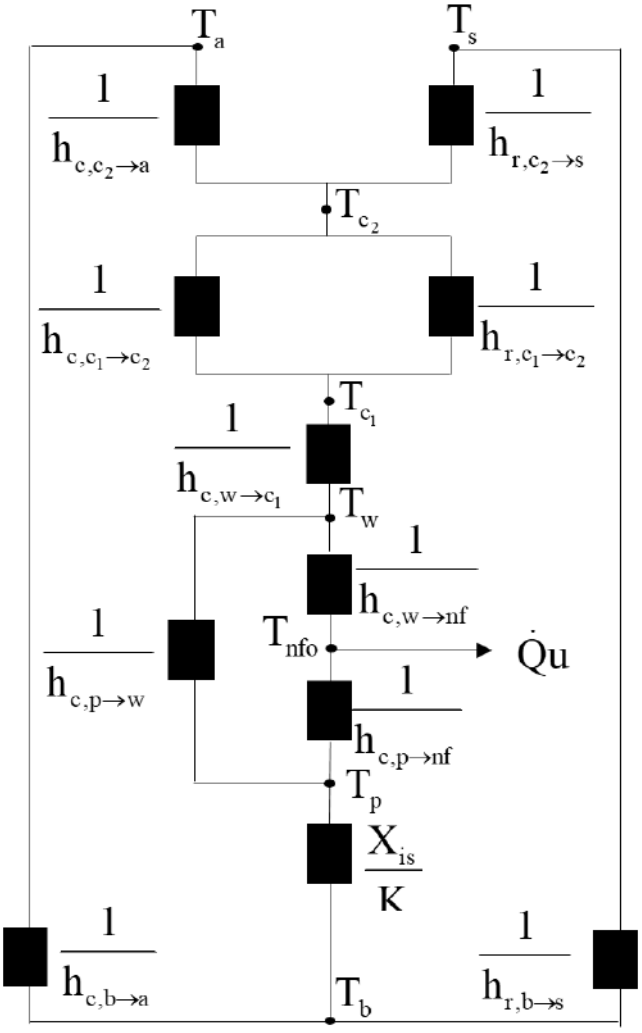


FIGURE 3.4: Diagram showing the heat transfer mechanisms in SSP operating under the open cycle mode of heat extraction.

3.3.1 Energy Balance Equation for Absorber Plate

$$I_T\tau_c^2\tau_w'\alpha_p\left(A_p-\tfrac{A_{he}}{2}\right)=h_{C,p\to w}\left(A_p-\tfrac{A_{he}}{2}\right)(T_p-T_w)+U_bA_p\left(T_P-T_a\right)+\dot{Q}_u \tag{3.28}$$

$\tau_w'$is the transmissivity of the pond water in the presence of the heat exchanger tube:

$$\tau_w'=\sum_{i=1}^{5}\psi_i\exp\left(-\mu_iX_w\right) \tag{3.29}$$

where μ_i is the extinction coefficient $(m)^{-1}$ of the solar radiation portion ψ_i. The values of μ_i and ψ_i are given in 3.1

$A_{he}$is the area of the heat exchanger tube (m^2) where:

$$A_{he}=2\pi rL_{he} \tag{3.30}$$

TABLE 3.1: The coefficients of the water transmittance [6]

i	ψ	μm^{-1}.
1	0.237	0.032
2	0.137	0.45
3	0.167	3
4	0.179	35
5	0.224	225

L_{he} is the length of the heat exchanger tube (m^2).
$\dot{Q}_u$ is the rate of thermal energy transferred from the pond water to the pond heat exchanger tube (W) ,is given by:

$$\dot{Q}_u = \dot{m}_f C_f \left(T_{fo} - T_{fi}\right) \tag{3.31}$$

$\dot{m}_f$ is the mass flow rate (Kg/s)

3.3.1.1 Energy Balance Equation for the Pond Water:

$$\begin{aligned} &I_T \tau_c^2 \alpha_w A_w + h_{C,p\to w}\left(A_p - \tfrac{A_{he}}{2}\right)\left(T_p - T_w\right) = m_w C_W \left(\tfrac{dT_w}{dt}\right) \\ &+h_{C,w\to c_1} A_w \left(T_w - T_{c1}\right) + h_{C,w\to f}\left(\tfrac{A_{he}}{2}\right)\left(T_w - T_f\right) + U_s A_s \left(T_w - T_a\right) \end{aligned} \tag{3.32}$$

3.3.2 Energy Balance Equation for Heat Exchanger Tube Welded on The Absorber Plate:

$$\begin{aligned} &\left(\tfrac{P}{2}\right) I_T \tau_c^2 \tau_w' \alpha_{he} dx + h_{C,p\to f}\left(\tfrac{P}{2}\right)\left(T_p - T_f\right) dx + h_{C,w\to f}\left(\tfrac{P}{2}\right)\left(T_w - T_f\right) dx \\ &= \dot{m}_f C_f \left(\tfrac{\partial T_f}{\partial x}\right) dx + A_t \rho_f C_f \left(\tfrac{\partial T_f}{\partial t}\right) dx \end{aligned} \tag{3.33}$$

P is the perimeter of the pond heat exchanger tube (m) ,is given by:

$$P = 2\pi r \tag{3.34}$$

α_{he} is the absorptivity of the heat exchanger tube.
$h_{CW\to f}$ is the convective heat transfer coefficient between the water and the heat transfer fluid , is calculated by the following correlation:

$$\tfrac{1}{h_{CW\to f}} = \left(\tfrac{1}{ho}\right) + \left(\tfrac{X_{he}}{K_{he}}\right) + \left(\tfrac{1}{hi}\right) \tag{3.35}$$

X_{he} is the thickness of the heat exchanger tube (m) .
K_{he} is the thermal conductivity of the heat exchanger tube (W/mK).
Where :

$$ho = hi = \frac{\left(NuK_f\right)}{D_{he}} = 0.47\left(\frac{K_f}{D_{he}}\right)(Gr\,\mathrm{Pr})^{\frac{1}{4}} \tag{3.36}$$

ho is the convective heat transfer coefficient from the pond water to the outer surface of the heat exchanger tube
hi is the convective heat transfer coefficient from the inner surface of the heat exchanger tube to the heat transfer fluid
D_{he} is the diameter of the heat exchanger tube (m) .
ρ_f is the mass density of the heat transfer fluid (Kg/m^3).
A_t is the cross sectional area of the heat exchanger tube (m^2), and is given by:

$$A_t = \pi r^2 \tag{3.37}$$

Temperature of the absorber plate:

$$T_p = \frac{\left(A_p - \frac{A_{he}}{2}\right)\left(I_T\tau_c^2\tau_w'\alpha_p + h_{C,p\to w}T_w\right) + U_bA_pT - \dot{Q}_u}{h_{C,p\to w}\left(A_p - \frac{A_{he}}{2}\right) + U_bA_p} \tag{3.38}$$

$$M\left(\frac{dT_w}{dt}\right) + a_1T_w = f_1(t) \tag{3.39}$$

Temperature of the pond water:

$$T_w = \frac{f_1(t)}{a_1} + \left(T_{wi} - \frac{f_1(t)}{a_1}\right)\exp^{\left(\frac{-at}{M}\right)} \tag{3.40}$$

Where:

$$\begin{aligned} a_1 = &\left[\frac{h_{C,w\to c_1}A_wA_c\left(h_{C,c_1\to c_2} + h_{R,c_1\to c_2}\right)}{h_{C,w\to c_1}A_w + A_c\left(h_{C,c_1\to c_2} + h_{R,c_1\to c_2}\right)}\right] + \left[\frac{h_{C,p\to w}\left(A_p - \frac{A_{he}}{2}\right)U_bA_p}{h_{C,p\to w}\left(A_p - \frac{A_{he}}{2}\right) + U_bA_p}\right] \\ &+ h_{C,w\to f}\left(\frac{A_{he}}{2}\right) + U_sA_s \end{aligned} \tag{3.41}$$

$$f_1(t) = \left| \frac{h_{C,p\to w}\left(A_p - \frac{A_{he}}{2}\right)\left\{ I_T \tau_c^2 \tau'_w \alpha_p + T_a \left[U_b A_p + U_S A_s + \left(\frac{U_b A_p U_S A_s}{h_{C,p\to w}\left(A_p - \frac{A_{he}}{2}\right)} \right) \right] - \dot{Q}_u \right\}}{h_{C,p\to w}\left(A_p - \frac{A_{he}}{2}\right) + U_b A_p} \right|$$

$$+ I_T \tau_c^2 \alpha_w A_w + h_{C,w\to f}\left(\frac{A_{he}}{2}\right) T_f + \left| \frac{h_{C,w\to c_1} A_w \left\{ A_c \left[I_T \tau_c \alpha_c + T_{c_2}\left(h_{C,c_1\to c_2} + h_{R,c_1\to c_2}\right) \right] \right\}}{h_{C,w\to c_1} A_w + A_c\left(h_{C,c_1\to c_2} + h_{R,c_1\to c_2}\right)} \right| \tag{3.42}$$

On substituting Tp and using equation 3.38, equation 3.33 can be written as:

$$\frac{\partial T_f}{\partial x} + a_2 \frac{\partial T_f}{\partial t} + b_1 T_f = f_2(t) \tag{3.43}$$

Where:

$$f_2(t) = \frac{\left(\frac{p}{2}\right)\left(I_T \tau_C^2 \tau'_W \alpha_{he} + h_{C,p\to f} T_p + h_{C,w\to f} T_w\right)}{\dot{m}_f C_f} \tag{3.44}$$

and:

$$b_1 = \frac{\left(\frac{p}{2}\right)\left(h_{C,p\to f} + h_{C,w\to f}\right)}{\dot{m}_f C_f} \tag{3.45}$$

and:

$$a_2 = \left(\frac{A_t \rho_f}{\dot{m}_f}\right) \tag{3.46}$$

In order to solve the partial differential equation 3.43, the following transformation relation is used :

$$\varepsilon = x + \frac{t}{a_2} \tag{3.47}$$

Using equation 3.47 ,equation 3.43 becomes:

$$2\left(\frac{dT_f}{\varepsilon}\right) + b_1 T_f = f_2(t) \tag{3.48}$$

Using the initial condition T_f (x = 0, t = 0)= T_{fi}, the solution of equation 3.48 may be written as:

$$T_f(x,t) = T_{fi} \exp - \left(\frac{b_1}{2}\right)\left(x + \frac{t}{a_2}\right) + \left(\frac{f_2(t)}{b_1}\right)\left(1 - \exp - \left(\frac{b_1}{2}\right)\left(x + \frac{t}{a_2}\right)\right) \tag{3.49}$$

Temperature of the heat exchanger fluid is obtained as:

$$T_{fo} = T_f(x,t)_{x=L_{he}} = T_{fi} \exp\left[-\left(\frac{b_1}{2}\right)\left(L_{he} + \frac{t}{a_2}\right)\right] + \left(\frac{f_2(t)}{b_1}\right)\left\{1 - \exp\left[-\left(\frac{b_1}{2}\right)\left(L_{he} + \frac{t}{a_2}\right)\right]\right\} \tag{3.50}$$

The rate of energy collected:

$$\dot{Q}_{coll} = \frac{m_w C_w \left(T_{fo} - T_{fi}\right)}{\Delta t} \tag{3.51}$$

The HWB equation for the instantaneous (hourly) heat flux per unit area of the SSP is defined as [12]

$$\dot{q} = (\alpha\tau)_e I_T - U_l \left(T_{wf} - T_{wi}\right) \tag{3.52}$$

where I_T is the total solar flux incident on the pond cover, T_{wi} is the initial pond water temperature and T_{wf} is the final pond water temperature and U_l is the overall loss coefficient are calculated as follows:

$$U_l = U_b + U_s\left(\frac{A_s}{A_b}\right) + U_t \tag{3.53}$$

U_t is the top loss coefficients for the SSP it can be calculated using the following equation [4]:

$$Ut = \frac{1}{\left(h_{C,p\to w}\right)^{-1} + \left(h_{C,w\to c_1}\right)^{-1} + 2\left(\frac{K_g}{X_g}\right)^{-1} + \left(h_{C,c_1\to c_2} + h_{R,c_1\to c_2}\right)^{-1} + \left(h_{C,c2\to a} + h_{R,c_2\to s}\right)^{-1}} \tag{3.54}$$

where:
X_g is thickness of the glass cover (m)
K_g is the thermal conductivity of the glass cover (W/mK)
The instantaneous collection efficiency η_i is defined as [12]:

$$\eta_i = \frac{\dot{q}}{I_T} \tag{3.55}$$

It is also useful to define the daily collection efficiency η_d [12]:

$$\eta_d = \frac{\int \dot{q} dt}{\int I_T dt} \tag{3.56}$$

The instantaneous efficiency of heat removal η_{ir} is defined as [18]:

$$\eta_{i_r} = \frac{\dot{Q}_u}{I_T} \tag{3.57}$$

Daily efficiency of heat removal η_d is defined as follows [18]:

$$\eta_{dr} = \frac{\int \dot{Q}_u dt}{\int I_T dt} \tag{3.58}$$

3.4 Carrier Fluid Description

Heat transfer plays an effective role in many industrial processes and consumer applications, such as cooling, heating, power generation, chemical and food industries, as well as air conditioning. However, conventional fluids used in thermal processes such as water, engine oil and ethylene glycol possess reduced thermal properties such as thermal conductivity, which may limit the efficiency of heat transfer and impose severe restrictions on them. One of the most important ways to overcome this problem is to use nanofluids, which are a colloidal fluid consisting of tiny particles ranging in size from 1 to 100 nanometers suspended in a basic fluid such as water, And it has been proven that adding nanoparticles to conventional fluids greatly improves the thermal conductivity,errano et al. [40], provided excellent examples of nanometer in comparison with millimeter and micrometer to understand clearly as can be seen in figure 3.5. This section aims a summary of

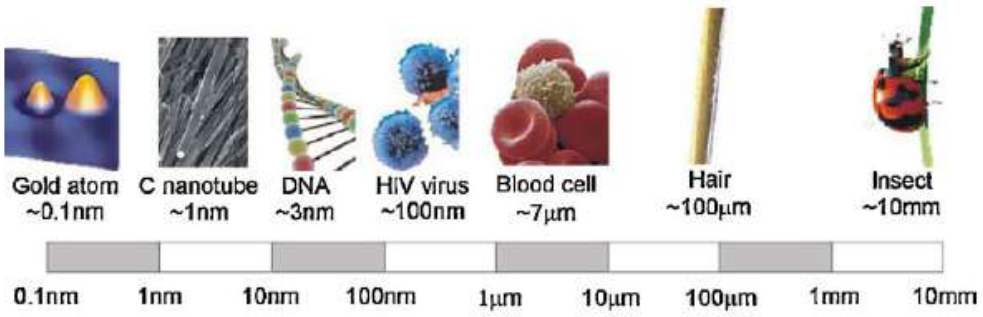


FIGURE 3.5: Length scale and some examples related [40]

different studies to estimate the thermo-physical properties of the nanofluids and the heat transfer coefficient.

3.4.1 components of nanofluids

A nanoparticle is an assembly of a few hundred to a few thousand atoms, resulting in an object of which at least one of the dimensions is of nanometric size (1 to 100 nm). Nanoparticles lie on the border between the microscopic

scale and the atomic or molecular scale. The most used nanoparticles to obtain nanofluids are shown in the figure 3.6

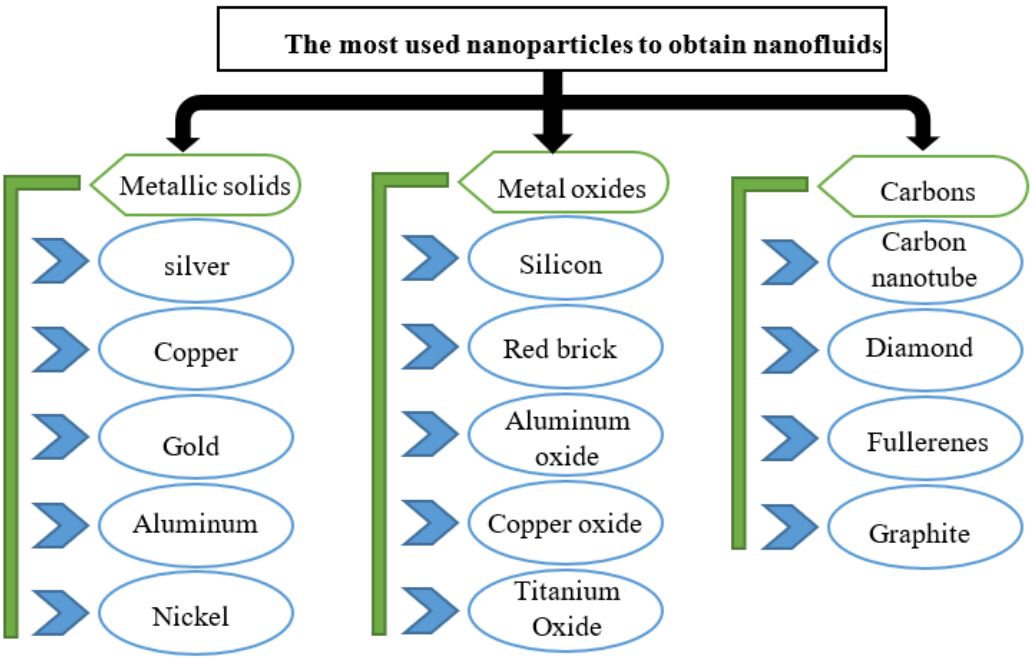


FIGURE 3.6: The most important nanoparticles used in the preparation of nanofluids

The most commonly used base fluids to obtain nanofluids are shown in the figure3.7 The dispersion of solid nanoparticles in the base fluid leads to a change in the thermal properties of the latter, which are represented by thermal conductivity, density, dynamic viscosity and specific heat. There are several parameters related to the nanoparticles that have a great influence on the physical and thermal properties of the obtained nanofluid, including the thermal conductivity of the base fluid, the medium temperature, the size and type of the nanoparticles and their thermal conductivity, as well as the volume fraction ...etc.

3.4.2 Thermal and physical properties of nanofluids

In order to calculate the expected heat transfer coefficients of nanofluids, and assuming that the nanoparticles are well dispersed with the base fluid, and that the resulting nanofluid is in thermal equilibrium and stability, the thermal and physical properties of this nanofluid can be calculated using the different relationships mentioned in the literature.

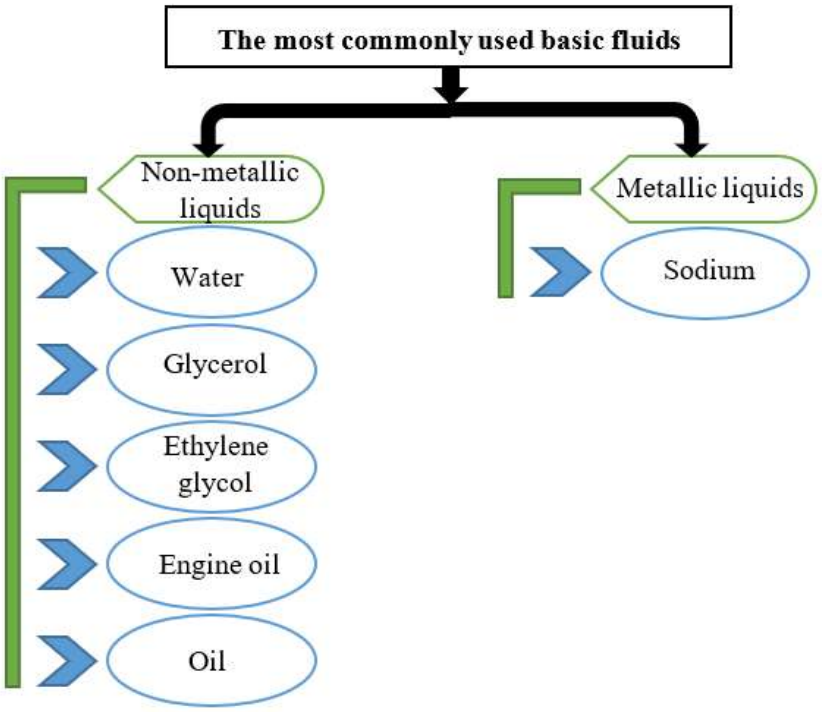


FIGURE 3.7: Some basic fluids used in the preparation of nanofluids

3.4.2.1 Density

The density of a homogeneous nanofluid can be calculated as a function of the volume fraction of the nanoparticles by the following relationship

$$\rho_{nf} = \frac{m_{nf}}{V_{nf}} = \frac{m_{bf}+m_p}{V_{bf}+V_p} = \rho_{bf}\frac{V_{bf}}{V_{bf}+V_p} + \rho_p\frac{V_p}{V_{bf}+V_p} \tag{3.59}$$

Where the volume fraction φ(%) denotes the ratio of the volume of the nanoparticles to the total volume of the nanofluid.

$$\varphi = \frac{V_p}{V_{bf}+V_p} \tag{3.60}$$

So, the density of the nanofluid can be written as follows:

$$\rho_{nf} = (1-\varphi)\,\rho_{bf} + \varphi\rho_p \tag{3.61}$$

Where:
$\rho_{nf}$is the mass density of the nanofluid.
ρ_{bf} is the mass density of the basic fluid.
ρ_p is the mass density of the solid nanoparticles

3.4.2.2 Specific heat

Specific heat is the heat input required to raise the temperature of a unit material by 1 (K) during the studied transformation [41]. In order to determine the specific heat of the nanofluid ,Most of the studies carried out in the literature use one of the two models defined by the equations 3.62 ,3.63 to determine the specific heat of nanofluids.

3.4.2.2.1 Pak and Cho model [42]:

$$\left(C_p\right)_{nf} = \frac{\rho_p\left(C_p\right)_p\varphi+\rho_{bf}\left(C_p\right)_{bf}(1-\varphi)}{\rho_{nf}} \tag{3.62}$$

3.4.2.2.2 Xuan and Roetze model [42]:

$$\left(C_p\right)_{nf} = (1-\varphi)\left(C_p\right)_{bf} + \varphi\left(C_p\right)_p \tag{3.63}$$

3.4.2.3 Viscosity

Viscosity characterizes the ability of a fluid to flow. His knowledge is fundamental for all applications involving the transport of fluids. The addition of nanoparticles makes it possible to increase and improve the thermal conductivity of the nanofluid, but it can also lead to an unfavorable increase in dynamic viscosity [41]. Thus, these two properties are closely correlated, and must be mastered for the use of this type of fluid in heat exchangers. Many theoretical and experimental studies have been carried out in order to estimate or measure the dynamic viscosity of nanofluids, Several theoretical models have been developed to predict the evolution of the dynamic viscosity of suspensions under certain conditions. In this part, we will focus on the models most used in the case of nanofluids.

3.4.2.3.1 Einstein model: The dynamic viscosity of a nanofluid given by Einstein [42] for a mixture containing dilute suspensions of fine spherical and rigid particles is as follows:

$$\mu_{nf} = (1+2.5\varphi)\,\mu_{bf} \tag{3.64}$$

Where:
μ_{nf} is the dynamic viscosity of the nanofluid
μ_{bf} is the dynamic viscosity of the base fluid
This relation is only valid for φ <0.03.

3.4.2.3.2 Brinkman model: Brinkman's formula complements Einstein's model down to a volume fraction of less than 4(%) [42]:

$$\mu_{nf} = \left[\frac{1}{(1-\varphi)^{2.5}}\right] \mu_{bf} \tag{3.65}$$

3.4.2.3.3 Maiga model: Other relationships have been proposed in the literature limited to very specific applications. Maiga et al. [42] from the results of measurements proposed the following correlation:

$$\mu_{nf} = \left(123\varphi^2 + 7.3\varphi + 1\right) \mu_{bf} \tag{3.66}$$

TABLE 3.2: Ratio of the viscosities of the nanofluid $(Al_2O_3 + H_2O)$ obtained from the different models studied

φ(%)	Einstein	Brinkman	Maiga
0	1	1	1
1	1.0250	1.0254	1.10
2	1.0500	1.0518	1.21
3	1.0750	1.0791	1.32
4	1.1000	1.1074	1.48

By comparing this correlation to Einstein and Brinkman models, we find that these last two approaches underestimate the experimental values of the viscosity of nanofluids.

3.4.2.4 Thermal conductivity

Thermal conductivity is the ability of a material to conduct or transmit heat. This is a very important property for improving the thermal performance of a heat transfer fluid. The synthesis of nanofluids responds to the need to improve and amplify the thermal conductivity of liquids [41]. Also, many works have been carried out to measure but also predict and explain this improvement. There are several theoretical models for estimating, under certain conditions, the thermal conductivity of suspensions. In this section,

We present in table 3.3, the values of the thermal conductivities of nanoparticles and base fluids used to form nanofluids.

TABLE 3.3: Values of thermal conductivities of nanoparticles and fluids used [5, 43]

The materials	Shapes	Thermal conductivities $(W/m.K)$
Metallic solids	Silver	427
	Copper	399
	Gold	316
	Aluminum	236
	Nickel	91
Metal oxides	Silicon oxide	1.38
	Aluminum oxide	37.17
	Copper oxide	20
	Titanium Oxide	8.4
Carbons	Carbon nanotube	2000-3000
	Diamond	2300
	Fullerenes	0.4
	Graphite	110-190
Non-metallic liquids	Water	0.597
	Glycerin	0.286
	Ethylene glycol	0.253
	Engine oil	0.145
Metallic liquids	Sodium (644 K)	72.3

3.4.2.4.1 Maxwell model: Maxwell is one of the researchers interested in calculating the thermal conductivity of a fluid containing suspended spherical particles. To arrive at the estimate of the latter, he assumed that the fluid contains several spherical particles of the same diameter. The particles are separated by a sufficient distance leading to the absence of mutual interaction between them, therefore the medium is strongly expanded (no contact between the particles). Maxwell's formula is given by [42]:

$$k_{nf} = \left[\frac{k_p+2k_{bf}+2\varphi\left(k_p-k_{bf}\right)}{k_p+2k_{bf}-\varphi\left(k_p-k_{bf}\right)}\right] k_{bf} \tag{3.67}$$

Where:

k_{nf} is the thermal conductivity of the nanofluid

k_{bf} is the thermal conductivity of the base nanofluid

k_p is the thermal conductivity of the nanoparticles

3.4.2.4.2 Bruggeman model: The model proposed by Bruggeman [42] seems to approximate certain experimental results better compared to other models for the case of spherical nanoparticles with no limitation concerning the concentrations of the nanoparticles.

$$k_{nf} = \left[\frac{1}{4}\left[(3\varphi - 1)\frac{k_p}{k_{bf}} + (2 - 3\varphi)\right] + \frac{k_{bf}}{4}\sqrt{\Delta}\right] k_{bf} \tag{3.68}$$

Where:
$\Delta = (3\varphi - 1)^2\left(\frac{k_p}{k_{bf}}\right)^2 + (2 - 3\varphi)^2 + 2\left(2 + 9\varphi - 9\varphi^2\right)\frac{k_p}{k_{bf}}$
This model does not take into account the size of the particles or their shape.

3.4.2.4.3 Hamilton's model: Hamilton's model [42] is an extension of Maxwell's model. It concerns particles of any shape. To take into account this diversity of shape, Hamilton introduces a geometric factor called sphericity ψ referring to spherical geometry. This coefficient is defined as the ratio of the area of the sphere having the same volume as the nanoparticles to the area of a nanoparticle.

$$k_{nf} = \left[\frac{k_p + (n-1)k_{bf} + (n-1)\varphi\left(k_p - k_{bf}\right)}{k_p + (n-1)k_{bf} - \varphi\left(k_p - k_{bf}\right)}\right] k_{bf} \tag{3.69}$$

n is an empirical form factor given by:$n = \frac{3}{\psi}$
This model can be used when the thermal conductivity of the particles is at least 100 times higher than that of the base fluid

3.4.2.5 Heat transfer

The rate of heat transfer by convection is described by the dimensionless number called the Nusselt number, Nu which plays a special role. This dimensionless number represents the ratio of convective heat flux to pure diffusion heat flux.
The convective flow is given by Newton's law:

$$\phi_{conv} = hA\Delta T \tag{3.70}$$

The conductive flux is given by Fourier's law:

$$\phi_{cond} = kA\frac{\Delta T}{\Delta x} \tag{3.71}$$

So, the Nusselt number is defined by:

$$Nu = \frac{\phi_{conv}}{\phi_{cond}} = \frac{hA\Delta T}{kA\frac{\Delta T}{\Delta x}} = \frac{h\Delta x}{k} \tag{3.72}$$

Where:
Δx is the diameter of the heat exchanger
k is the thermal conductivity of the fluid,
h is the convective exchange coefficient
There are several equations in the literature used for predicting of h for the laminar flow regime we have used Maiga Equation [44, 42] as given in the equation 3.73 to estimate the h of nanofluids for the laminar flow regime.

$$Nu_{nf} = 0.086\mathrm{Re}_{nf}^{0.55}\,\mathrm{Pr}_{nf}^{0.5} \tag{3.73}$$

that correlation is valid for $\varphi \prec 10(\%), \mathrm{Re} \leq 1000, \text{and} 6 \prec \mathrm{Pr} \prec 573$

Chapter 4

Results and Discussion

4.1 Results obtained from a numerical simulation of SSP under different operating conditions

The results obtained from the numerical simulation are based on the solutions of the differential equations previously mentioned, taking into account the following assumptions:

- Transitional system
- The temperature is uniform along the length of the solar pond
- Estimation of losses towards the back of the solar basin
- The absence of chemical reactions in the solar pond
- One-dimensional heat transfer
- Mechanical balance system
- Laminar flow
- The additional tubular load is neglected

The relevant parameters used in the calculation are presented in the table 4.1

The instantaneous values traced by the Bird & Hulstrom model of the solar radiation I_T incident on the SSP used in the different calculation programs are shown in figure 4.1

TABLE 4.1: Numerical parameters which were used for numerical calculations

Parameters	Value	Parameters	Value
α_C	0.05	$\rho_a \ (Kg/m^3)$	1.164
α_{he}	0.95	$K_a \ (W/mK)$	0.0251
α_p	0.95	$C_{P_a} \ (J/Kg\ \mathrm{K})$	1012
$\tau_w^{'}$	calculated by 3.29	$\mu_a \ (Kg/ms)$	18.64×10^{-6}
α_W	$1 - \tau_w^{'}$	$X_p = X_s \ (m)$	0.04
τ_C	0.9	$K_P = K_s \ (W/mK)$	0.157
ε_C	0.88	$X_{he} \ (m)$	0.001
$\beta_a \ (K^{-1})$	3.4×10^{-3}	$K_{he} \ (W/mK)$	59
$\sigma \ (W/m^2K^4)$	5.67×10^{-8}	$V \ (m/s)$	2

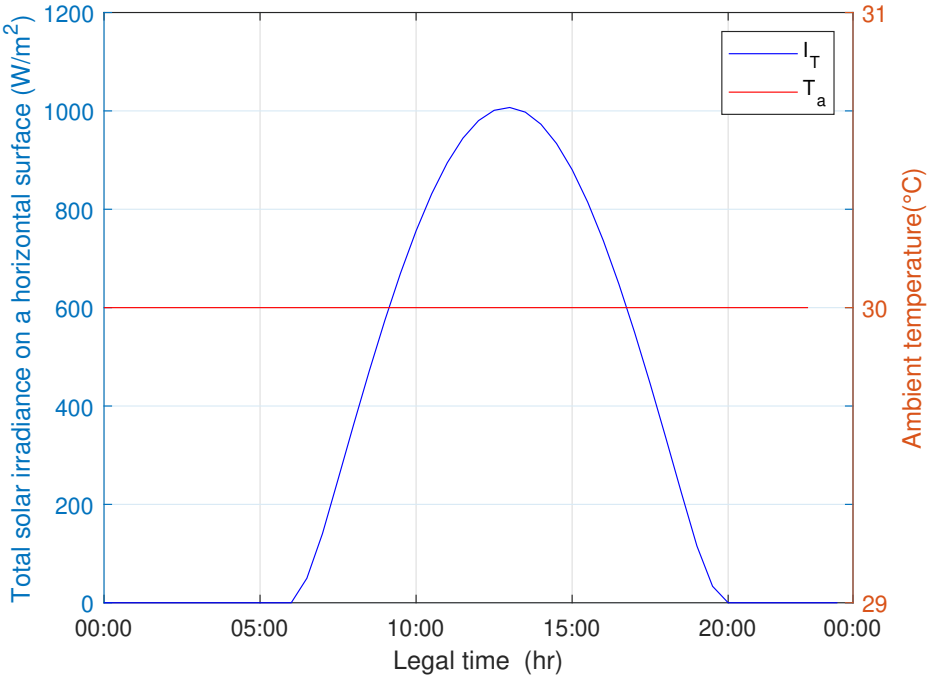


FIGURE 4.1: Hourly values of solar radiation I_T at Medea calculated by the Bird & Hulstrom model and the ambient air temperature on August 18

4.1.1 Numerical Simulation of SSP Under the Batch Mode of heat Extraction

Numerical simulations were performed to find the optimum thermal performance of a shallow solar pond operating under the batch mode for heat extraction as shown in figure 3.1, and this simulations was based on thermal balance equations between the various components of the SSP. The optimum thermal performance of the SSP depends on several factors such as the gap

between the glass covers, the depth of the SSP and the thickness of the insulating material. The results obtained are shown in the figures below.

4.1.1.1 The Effect of the Depth of the Pond Water on the Thermal Performance of the SSP

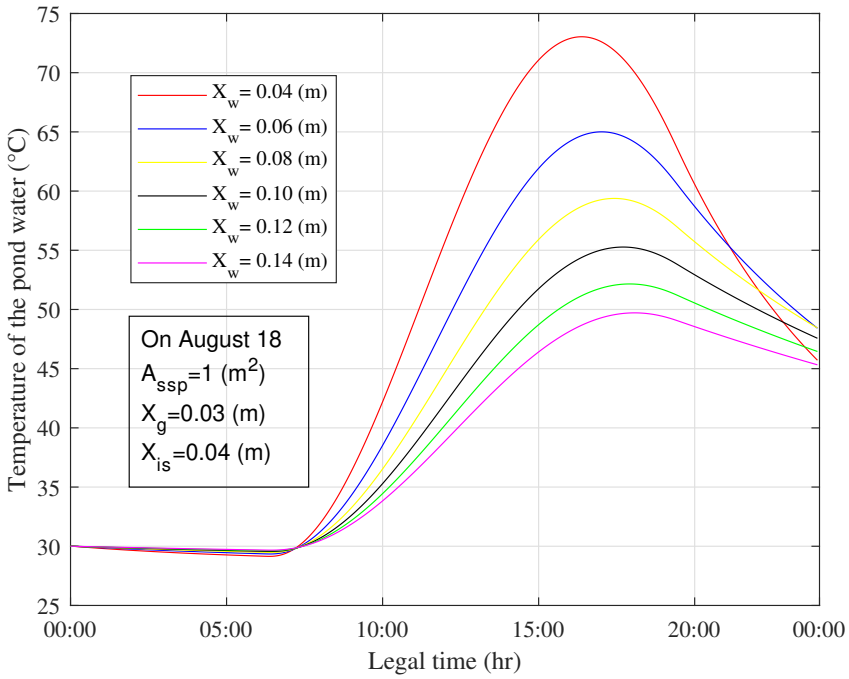


FIGURE 4.2: Calculated pond water temperature T_w vs time for different depth of the pond water

Figure 4.2 shows the evolution of the calculated temperature of the pond water T_w vs time with increasing in the depth of the pond X_w on August 18 when A_{SSP}=1 (m^2) and X_g=0.03 (m) ,X_{is}=0.04 (m). The T_w reaches a maximum at 16:00 at a value of 73.03, 65.00, 59.37, 55.27, 52.15, and 49.71 $(°C)$ this is for the X_w values estimated at 0.04, 0.06, 0.08, 0.1 ,0.12 and 0.14 (m) respectively.It is clear that the T_w is inversely proportional to the X_w during the sunshine hours, due to the increase in the heat capacity of the pond water with the increase in the X_w,but after sunset, the T_w is directly proportional to the X_w due to the effect of storage pond water,The obtained results indicate a good compatibility with those obtained by Aboul-Enein [11]

4.1.1.2 The Effect of the Gap Between the Glass Covers on the Thermal Performance of the SSP

Figure 4.3 shows the evolution of pond water temperature T_w vs time with different values of the gap between the two glass covers X_g, the pond water temperature reaches a maximum at 16:00 with very close values in the range of 65 $(°C)$ and this is for all the gap from 0.02 to 0.06 (m).

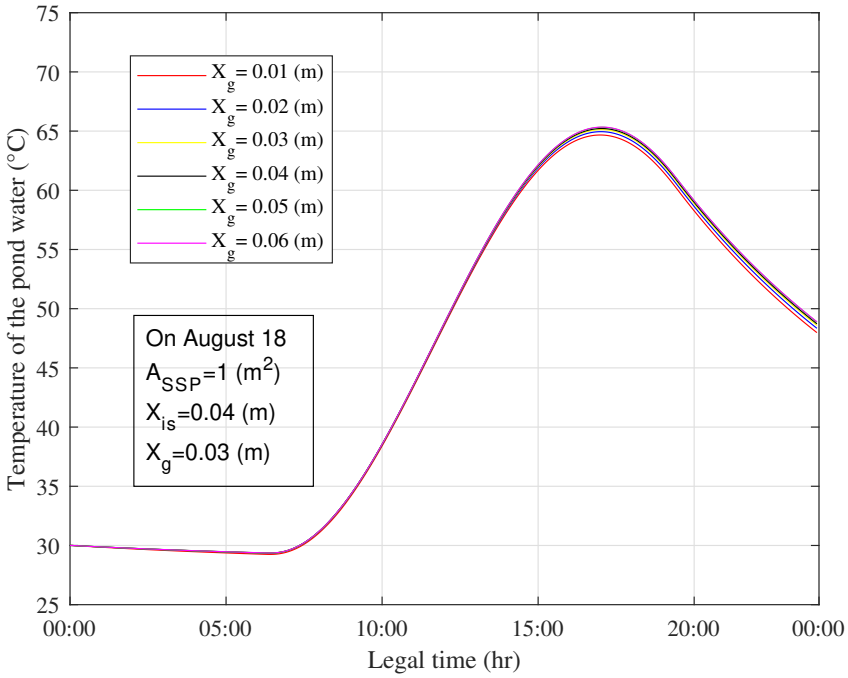


FIGURE 4.3: Calculated pond water temperature T_w vs time for different distance between the lower and upper glass covers

4.1.1.3 The Effect of Insulating Material Thickness on the Thermal Performance of the SSP

Figure 5.3 shows the evolution of the temperature of the pond water $T_w$vs time with increasing thickness of the insulation material. The pond water temperature reaches a maximum at 17:00 at a value of 51.33, 58.97, 62.75, 65.00, 66.49 and 67.55 $(°C)$ this is for the insulation thickness values estimated at 0.01, 0.02, 0.03, 0.04 ,0.05 and 0.6 (m) respectively.It is clear that the temperature of the pond water is directly proportional to the thickness of the thermal insulation, but the effect of the thermal insulation during the sunshine hours is negligible compared to the period of sunset.

Figure 4.5 shows the development of the water temperature of the SSP dur-

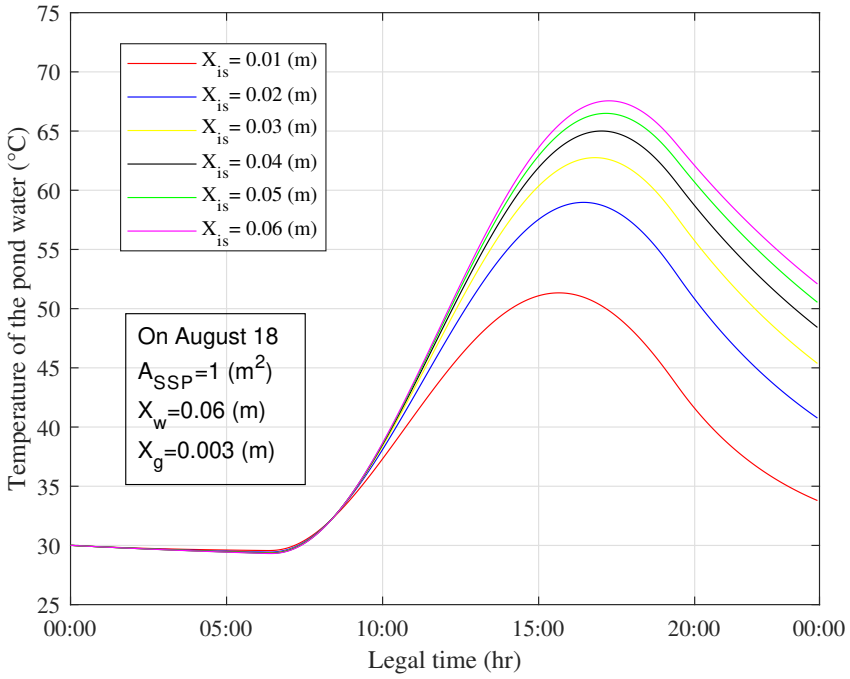


FIGURE 4.4: Calculated pond water temperature T_w vs time for different thicknesses of insulating material X_{is}

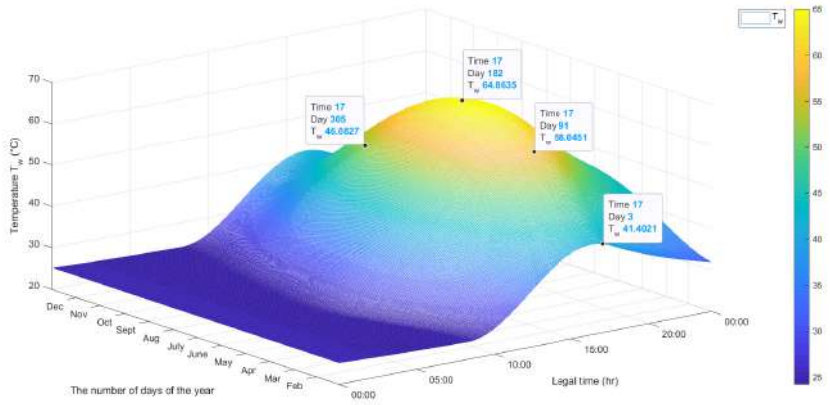


FIGURE 4.5: Variation of the pond water temperature T_w during the day and throughout the year

ing the day and throughout the year under the batch mode of heat extraction.When X_w=0.06 (m) and X_{is}=0.04 (m) .The highest value is recorded in the month of January at 17:00 in the afternoon, and it is estimated at 41.40 $(°C)$, while in the month of April it is estimated at 58.04 $(°C)$, as is done Recording the value of the pond water temperature at 64.86 $(°C)$ and 46.08 in July and November respectively.

Figure 4.6 shows the development of the amount of energy collected by

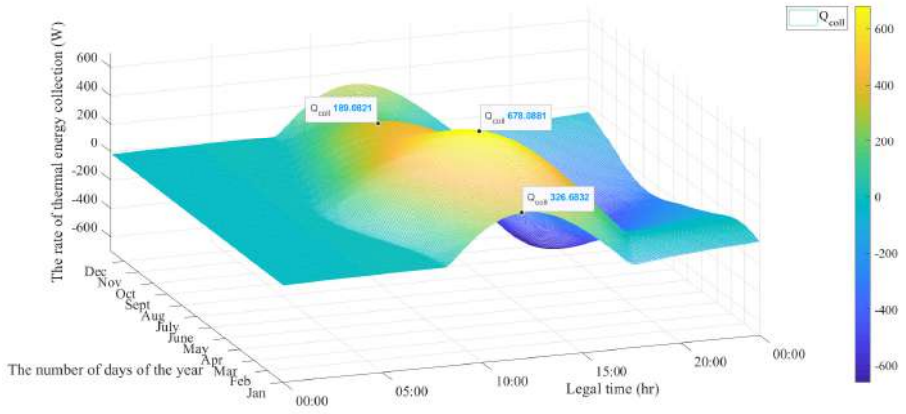


FIGURE 4.6: Variation of the useful energy collected during the day and throughout the year

the SSP during the day and throughout the year under the batch mode of heat extraction , the amount of energy collected during the night decreases due to thermal loss, then increases with the beginning of the day to reach its peak at midday, the amount of energy collected in the month of January at the midday is estimated at 326.25 (W), while the highest value of the collected energy in the year is recorded at midday in the month of April and is estimated at 678.08 (W), then this value decreases during the year to record its lowest value at midday in the month of October, which is estimated at 189, 08 (W), and then it increases with the passage of days. As for the lowest value of the combined energy loss during the day, it was recorded in the month of September at 18:00 in the afternoon, and it is estimated at -570.69, (W)

4.1.2 Numerical Simulation of the SSP Under the Open and Continuous mode of heat Extraction

Numerical simulations were performed to find the optimum thermal performance of a shallow solar pond operating under the open and continuous mode of heat extraction as show in the figure 3.3. The pond depth is 0.06 (m) . It is equipped with two glass covers to reduce thermal loss and it is provided with an insulating material of thickness equls 0.04 (m) . This simulation was based on thermal balance equations among the various components of SSP. After providing the pond with a heat exchanger by welded to the absorber

plate, the optimum thermal performance of the SSP depends on several factors such as the length of the heat exchanger and its diameter in addition to the mass flow rate of the heat transfer fluid. The results obtained are shown in the figures below.

4.1.2.1 The Effect of heat Exchanger Length on the Thermal Performance of the SSP

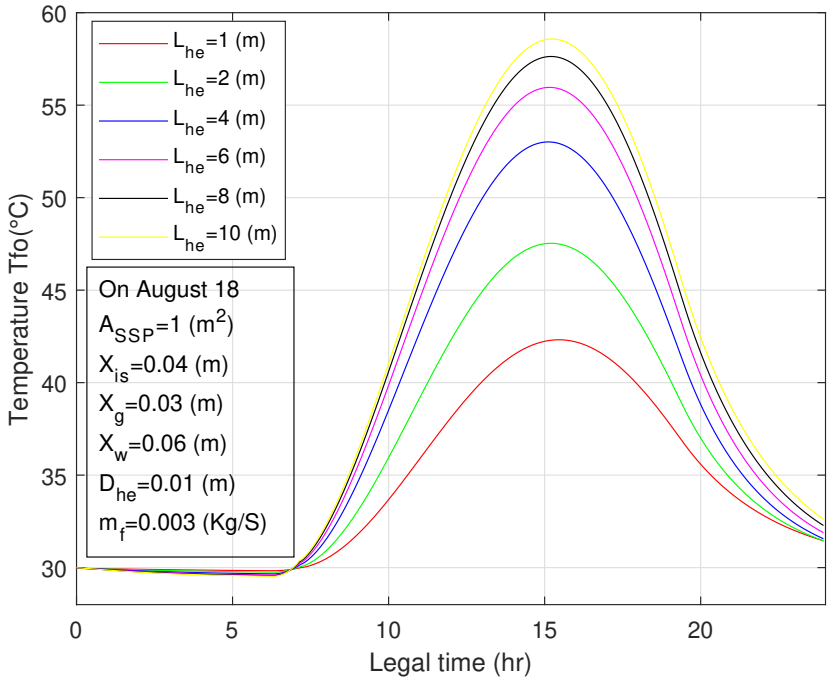


FIGURE 4.7: Calculated outlet temperature of the heat transfer fluid T_{fo} as a function of time for different values of the heat exchange length

Figure 4.7 show the hourly evolution of the calculated temperature of heat transfer fluid for different values of the heat exchanger length L_{he}= on August 18 when the diameter of heat exchanger Dhe=0.01 (m) ,the mass flow rate m_f=0.003 (Kg/s) ,the depth of the SSP X_w=0.06 (m),the gap between the glass covers X_g=0.03 (m) and the thickness of the insulation materials X_{is}=0.04 (m) . It is clear that the temperature of the heat transfer fluid is directly proportional to the length of the heat exchanger, and this is due to the increase in the heat exchange area between the pond water and the absorption plate on the one hand and the heat exchanger on the other hand, which allows an increase in the rate of energy transferred to the heat transfer fluid, The value of the temperature of the heat transfer fluid reaches its maximum

value at 15:00 and is estimated at the points : 42.31, 47.53, 53.01 , 55.95 , 57.63 and 58.57 $(^{\circ}C)$ for different values of the length of the heat exchanger:1 , 2 , 4 , 6 , 8 and 10 (m) respectively.

4.1.2.2 The Effect of heat Exchanger Diameter on the Thermal Performance of the SSP

Figure 4.8 shows the variation of the calculated temperature of the heat transfer fluid vs time for different values of the diameter of the heat exchanger. The value of the heat transfer fluid temperature increases at sunrise, reaching its peak in the afternoon, which is estimated at : 54.68, 57.99, 59.45, 60.25, 60.75 and 61.07 $(^{\circ}C)$for different values of diameter of the heat exchanger :0.01 , 0.02 , 0.03 , 0.04 ,0.05 and 0.06 (m) respectively. Then it gradually decreased due to the decrease in the rate of solar radiation.

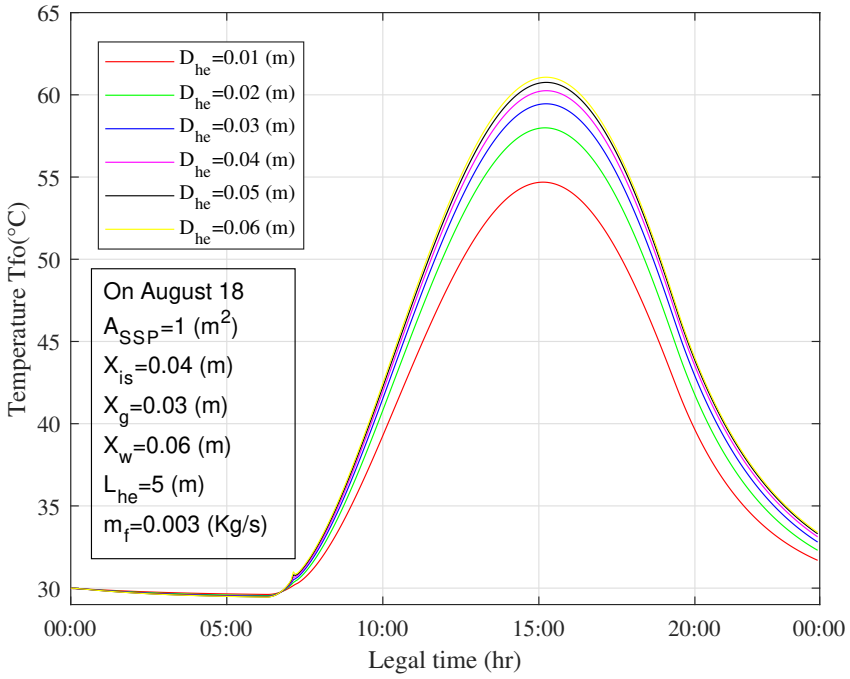


FIGURE 4.8: Calculated outlet temperature of the heat transfer fluid T_{fo} as a function of time for different values of diameter of the heat exchanger

4.1.2.3 The Effect of Mass Flow Rate on the Thermal Performance of the SSP

Figure 4.9 shows the effect of mass flow rate on the temperature of the heat transfer fluid , The temperature of the heat transfer fluid is inversely proportional to the mass flow rate. The maximum values for the temperature of the heat transfer fluid are recorded at 15:00 , which is estimated at : 68.06, 54.71, 43.91, 39.52, 37.26 and 35.89 $(°C)$ for different values of mass flow : 0.001 , 0.003 , 0.006 , 0.09 , 0.012 and 0.015 (Kg/s) respectively.

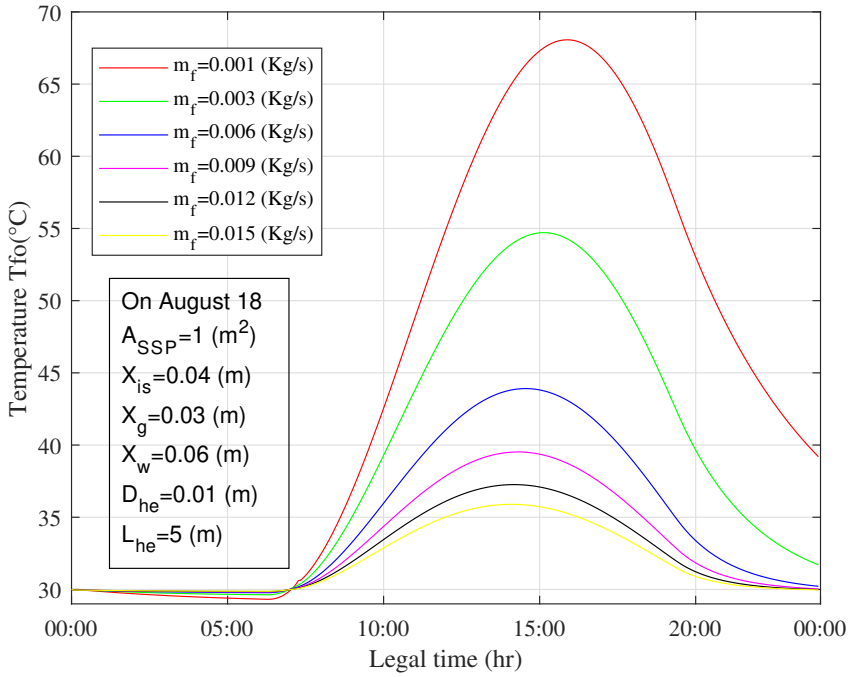


FIGURE 4.9: Calculated outlet temperature of the heat transfer fluid T_{fo} as a function of time for different values of mass flow rate

Figure 4.10 shows the temporal evolution of the beneficial energy extracted from the SSP vs time for diffrennt mass flow rate , with the length of heat exchanger Lhe=5 (m) , the diameter of heat exchanger Dhe=0.01 (m) ,the depth of the SSP X_w=0.06 (m) ,the gap between the glass covers X_g=0.03 (m) and the thickness of the insulation materials X_{is}=0.04 (m). The value of the useful energy extracted from the SSP increases in the morning, due to the solar radiation, until it reaches its peak at 14:00, which is estimated at : 159.40, 310.65, 350.30, 360.27, 366.84 and 372.79 (W) for different values of mass flow : 0.001 , 0.003 , 0.006 , 0.09 , 0.012 and 0.015 (Kg/s) respectively.

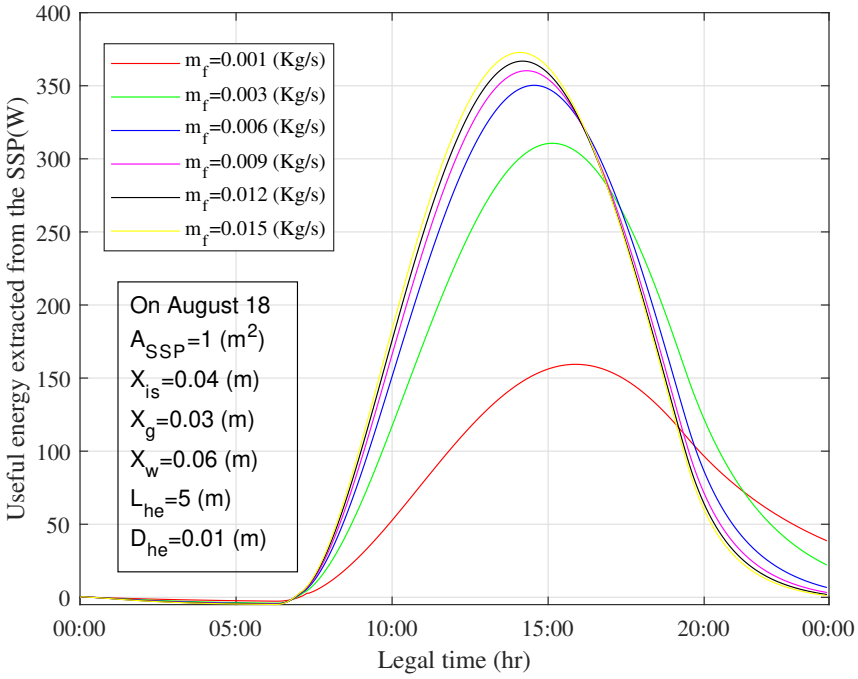


FIGURE 4.10: hourly variations in useful energy $\dot{Q}_u$ vs time for different value of mass flow rate

4.1.3 The effect of using nanofluids on the thermal performance of the SSP

As shown in figure 3.3 the system studied is a shallow solar pond working under the open cycle and continuous heat extraction. The pond area is 1 (m^2) and its depth is 0.06 (m). The SSP is equipped with two glass covers to increase the greenhouse effect, the distance between the two covers is 0.03 (m). The bottom of the pond was painted black in order to increase the absorption of solar radiation. In order to reduce heat loss, the SSP is coated with polyester material from the sides and from the bottom. The SSP is connected to a cold reservoir by serpentine welded to the bottom of the SSP. In order to extract heat from the SSP, we propose five types of heat transfer fluids consisting of water (H_2O) as a basic fluid, and five types of solid nanomaterials with different physical properties, namely copper Cu, titanium dioxide (TiO_2), silicon dioxide (SiO_2), copper oxide (CuO) and finally aluminum oxide (Al_2O_3). These nanofluids are pumped with a flow of 0.003 (kg/s), the heat exchanger length is 5 (m) and the diameter is 0.01(m). Based on the solutions of differential equations resulting from the thermal equations of the

SSP, a computer program was developed using the Matlab program in order to simulate the thermal performance of the SSP. The simulation was performed on August 18 from 00:00 am to 00:00 pm . The BIRD & HULSTROM model was also used to calculate solar radiation using climatic conditions for the city of Medea in Algeria. Latitude is 36.28° and longitude is 2.73° as shown in figure 4.1.

4.1.3.1 Thermophysical Properties of Nanofluids

The thermophysical properties of the nanofluids are calculated using the following models:
Thermal conductivity of nanofluids was calculated using the Maxwell model3.67
Viscosity of nanofluids was calculated using the Maiga et al. model 3.66
Density of nanofluids was calculated using the model 3.61
Specific heat capacity of nanofluids was calculated using the Pak and Cho model 3.62
The different physical properties of these nanoparticles and the basic fluid are shown in Table 4.2.

TABLE 4.2: Thermophysical properties of base fluid and nanoparticles

Thermophysical Properties	The basic fluid	nanoparticles				
	(H_2O)	(Al_2O_3)	(TiO_2)	(CuO)	(Cu)	(SiO_2)
$\rho\ (Kg/m^3)$	998.2	3960.14	4157	6450	8954	2220
$C\ (J/Kg\,\mathrm{K})$	4182	761.55	710	561	385	745
$K\ (W/mK)$	0.597	37.17	8.4	20	401	1.38
$\mu\ (Kg/m\,s) \times 10^{-6}$	993					

4.1.3.2 The effect of nanoparticles on the thermal conductivity of nanofluids

Figure 4.11 shows the positive effect of nanoparticles on the thermal conductivity of nanofluids. We recorded an increase the thermal conductivity of all type of nanofluids wich is $(Al_2O_3 + H_2O)$, $(CuO + H_2O)$, $(Cu + H_2O)$, $(SiO_2 + H_2O)$ and $(TiO_2 + H_2O)$ at different volume fraction ranging from 0 to 5(%).

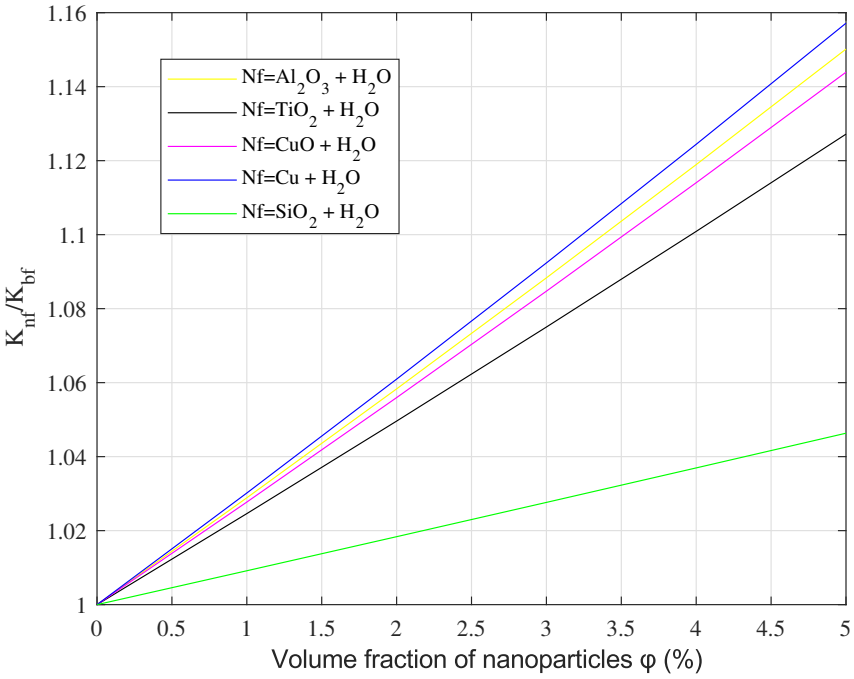


FIGURE 4.11: Impact of nanoparticles volume fraction on Thermal conductivity of nanofluids

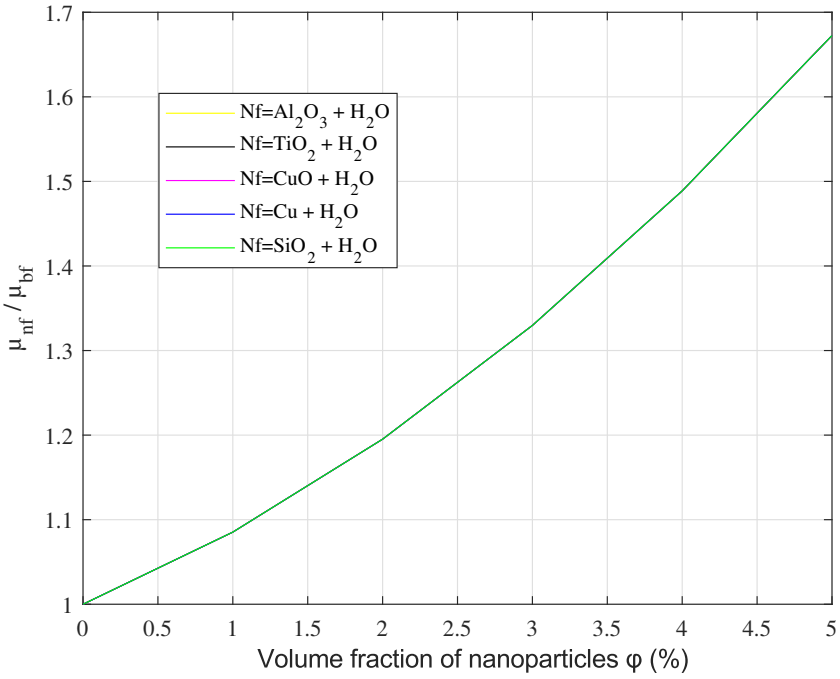


FIGURE 4.12: Impact of nanoparticles volume fraction on Dynamic viscosity of nanofluids

4.1.3.3 The effect of nanoparticles on the dynamic viscosity of nanofluids

Figure 4.12 shows the effect of submerged nanoparticles on the dynamic viscosity of nanofluids. Dynamic viscosity increases with increasing of the volume fraction of nanoparticle. Note that the effect of the volume fraction of nanoparticle on the nanofluids is equal, as shown in Figure 4.12 All curves are identical

4.1.3.4 The effect of nanoparticles on the specific heat capacity of nanofluids

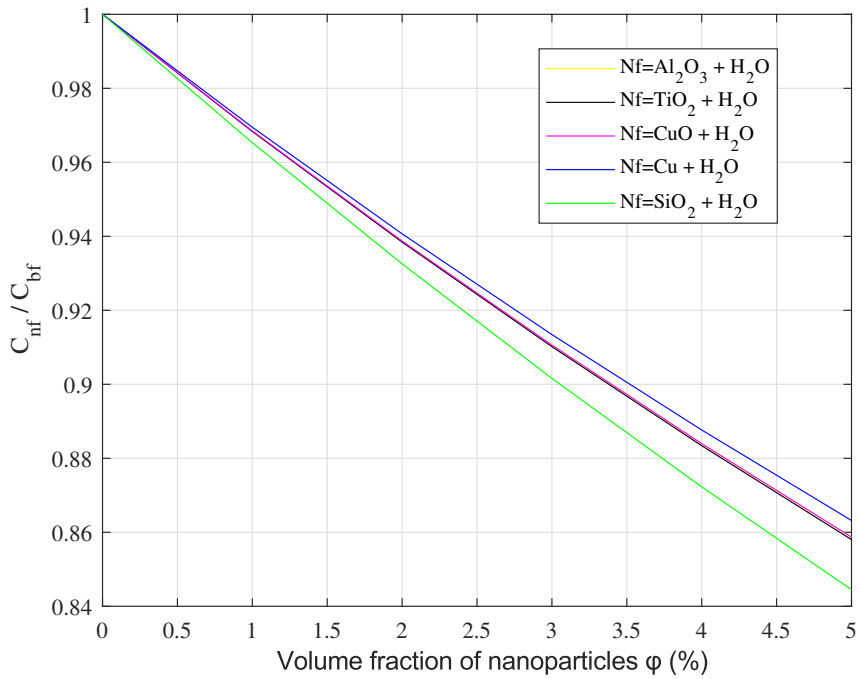


FIGURE 4.13: Impact of nanoparticles volume fraction on specific heat capacity of nanofluids

Figure 4.13 shows the effect of nanoparticles on the heat capacity for different nanofluids that contain water as a basic fluid and for different nanoparticles ((Al_2O_3), (CuO), (Cu), (SiO_2) and (TiO_2)) as a function of volume fraction that ranges from 0 to 5 (%). This effect is clearly negative, as a significant decrease in the heat capacity is recorded with the increase in the volume fraction, as this applies to all nanofluids.

4.1.3.5 The effect of nanoparticles on the density of nanofluids

Figure 4.14 Show the values of the nanofluids density ratios on the basic fluid density of the five nanofluids $(Al_2O_3 + H_2O)$, $(CuO + H_2O)$, $(Cu + H_2O)$, $(SiO_2 + H_2O)$ and $(TiO_2 + H_2O)$ depending on the volume fraction which ranges from 0 to 5(%). The obtained results show the positive effect of nanoparticles on the density of nanofluids as it increases with increasing of volume fraction.

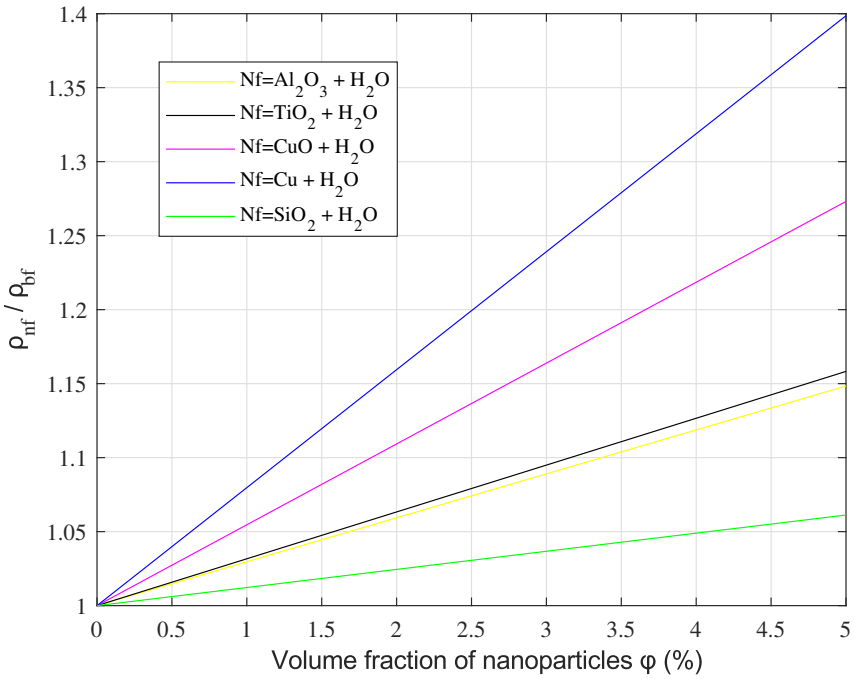


FIGURE 4.14: Impact of nanoparticle volume fraction on mass density of nanofluids

4.1.3.6 The effect of nanoparticles on the outlet temperature of the nanofluids

Figure 4.15 illustrates the temperature change for heat transfer based on nanofluid $(Al_2O_3 + H_2O)$ during the day with different concentrations of nanoparticles. and that will be on August 18 ,The numerical simulations are done based on the following SSP parameters:

- The area of the SSP eqals 1 (m^2)
- The depth of the SSP Xw=0.06 (m)
- The gap between the glass covers Xg=0.03 (m)

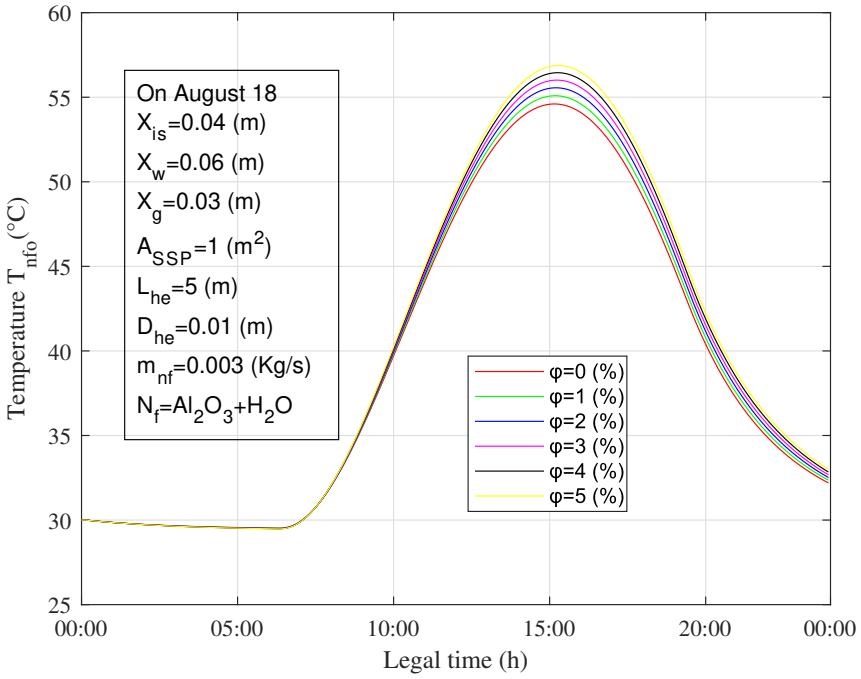


FIGURE 4.15: Calculated outlet temperature of the nanofluids $(Al_2O_3 + H_2O)$ vs time for different nanoparticles volume fraction φ

- The thickness of the insulation materials Xis=0.04 (m)
- The length of heat exchanger Lhe=5 (m)
- The diameter of heat exchanger Dhe=0.01 (m)
- The mass flow rate mf=0.003 (Kg/s).

The initial temperature of nanofluids is equal to the ambient air temperature which is 30 $(°C)$. For a range of the time comprise between 00:00 am and 15:00 , the temperature of nanofluids increases with sunrise and present a peak which is estimated at 54.60, 55.08, 55.55, 56.01, 56.44 and 56.87 $(°C)$ for different nanoparticle volume fraction 0, 1, 2, 3, 4, and 5 (%) respectively.Then the temperature gradually decreases with sunset. The temperature of all nanofluids $(Cu + H_2O)$,$(Cuo + H_2O)$,$(SiO_2 + H_2O)$ and $(TiO_2 + H_2O)$ behave as $(Al_2O_3 + H_2O)$ nanofluid in their evolution over time and with all different concentrations of nanoparticles, and the maximum values for the temperature of nanofluids at different concentrations are given in Table 4.3.

TABLE 4.3: Maximum temperature values for different nanofluids and with different volume fraction

	Maximum nanofluids temperature (°C)			
Volume fraction (%)	$SiO_2 + H_2O$	$Cu + H_2O$	$TiO_2 + H_2O$	$CuO + H_2O$
$\varphi = 0$	54.60	54.60	54.60	54.60
$\varphi = 1$	54.84	55.70	55.10	55.38
$\varphi = 2$	55.08	56.71	55.58	56.11
$\varphi = 3$	55.32	57.65	56.04	56.80
$\varphi = 4$	55.55	58.52	56.50	57.46
$\varphi = 5$	55.77	59.32	56.93	58.08

4.1.3.7 Comparison between the outlet temperature for different nanofluids

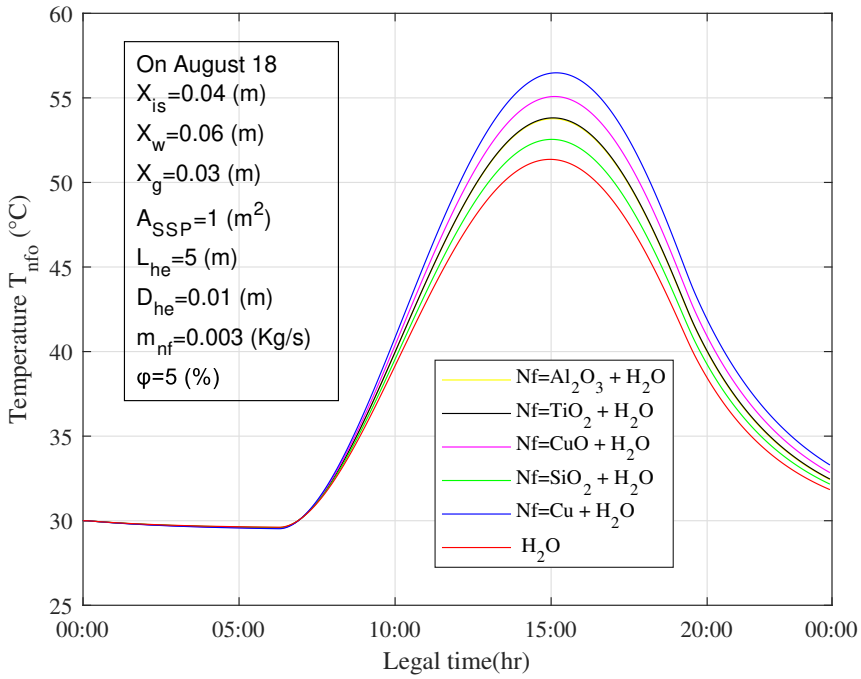


FIGURE 4.16: Comparison between calculate outlet temperature of the nanofluids vs time with nanoparticles volume fraction φ=5 (%) for different types of nanofluids and $\dot{m}_{nf}$= 0.003 (Kg/s)

Figure 4.16 shows a comparison between the outlet temperature of various nanofluids for a period of 00:00 a.m. to 00:00 p.m, with a volume fraction φ = 5 (%) ,the nanofluids temperature increases and peaks for all types of nanofluids, indicating the positive effect of nanoparticls on intensifying heat exchange. The effect of the mass flow rate on the temperature of the nanofluids is negative with a mass flow rate$\dot{m}_{nf}$= 0.003 (Kg/s); the maximum of

the nanofluids temperature at 15:00 are obtained around: 59.32, 58.08, 56.93 ,56.44, 55.77 and 54.60 $(°C)$ for the nanofluids based on (Cu), (CuO), (TiO_2), (Al_2O_3), (SiO_2) and (H_2O) , respectively. however, as the mass flow rate increases,$\dot{m}_{nf}$= 0.007 (Kg/s), the temperature drops significantly,as the figure 4.17 shows the maximum values at 15:00 are found to be 45.71, 44.61, 43.65, 43.60, 42.76 and 41.90 $(°C)$ respectively.

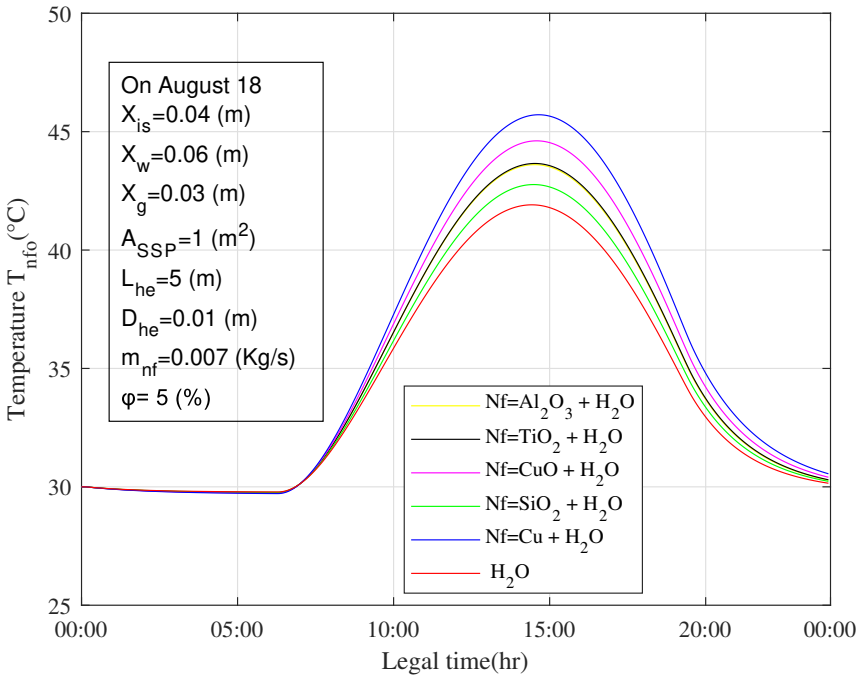


FIGURE 4.17: Comparison between calculate outlet temperature of the nanofluids vs time with nanoparticles volume fraction φ=5 (%) for different types of nanofluids and $\dot{m}_{nf}$= 0.007 (Kg/s)

4.1.3.8 The effect of nanoparticles on the useful energy extracted

Figure 4.18 shows the useful energy change based on $(Al_2O_3 + H_2O)$ nanofluids during the day with different concentrations of nanoparticles and that will be on August 18th with mass flow rate $\dot{m}_{nf}$= 0.003 (Kg/s).The useful energy increases between 00:00 AM and 15:00 and provides an estimated peak at 308.65, 304.84, 301.00, 297.15, 293.32, and 289.52 (W) for different sizes of nanoparticles fraction 0, 1, 2, 3, 4 and 5 (%), respectively, then the useful energy gradually decreases with sunset. The results obtained show that the value of the useful energy extracted from the SSP decreases with the increase in the size of the fraction of the nanoparticles.// The useful energy of

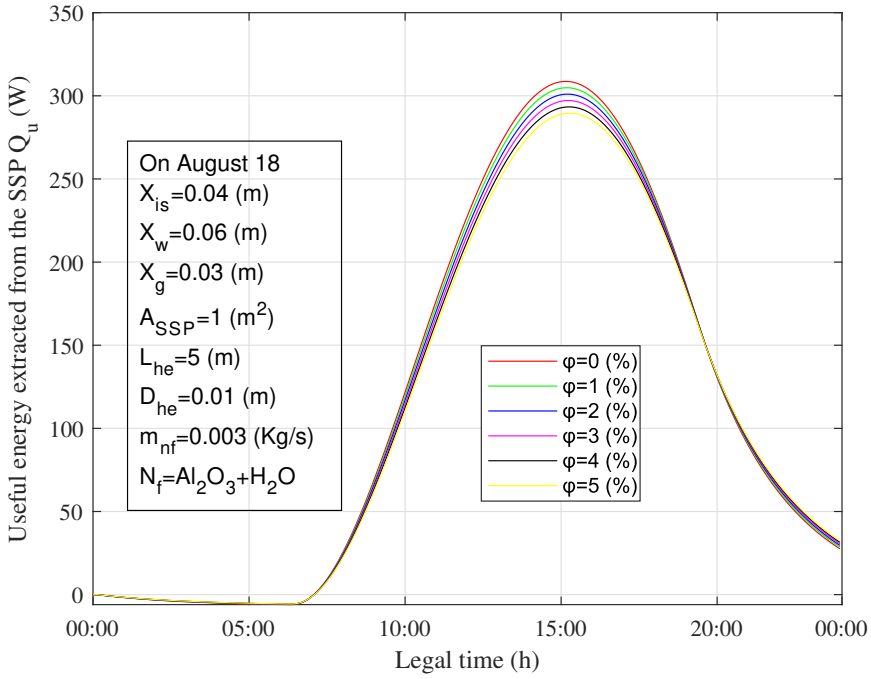


FIGURE 4.18: Calculated useful energy of the nanofluids $(Al_2O_3 + H_2O)$ vs time for different nanoparticle volume fraction φ

all nanofluids $(Cu + H_2O)$,$(Cuo + H_2O)$,$(SiO_2 + H_2O)$ and $(TiO_2 + H_2O)$ behave as $(Al_2O_3 + H_2O)$ nanofluid behave in their development over time and with all the different concentrations of nanoparticles, and the maximum values of the useful energy of the nanofluids at different concentrations are shown in Table 4.4.

TABLE 4.4: Maximum useful energy values for different nanofluids and with different volume fraction

	Maximum useful energy of nanofluids (W)			
Volume fraction (%)	$SiO_2 + H_2O$	$Cu + H_2O$	$TiO_2 + H_2O$	$CuO + H_2O$
$\varphi = 0$	308.65	308.65	308.65	308.65
$\varphi = 1$	306.10	298.14	304.38	301.53
$\varphi = 2$	303.50	288.10	300.11	294.58
$\varphi = 3$	300.86	278.54	295.85	287.83
$\varphi = 4$	298.21	269.43	291.65	281.28
$\varphi = 5$	295.55	260.77	287.48	274.94

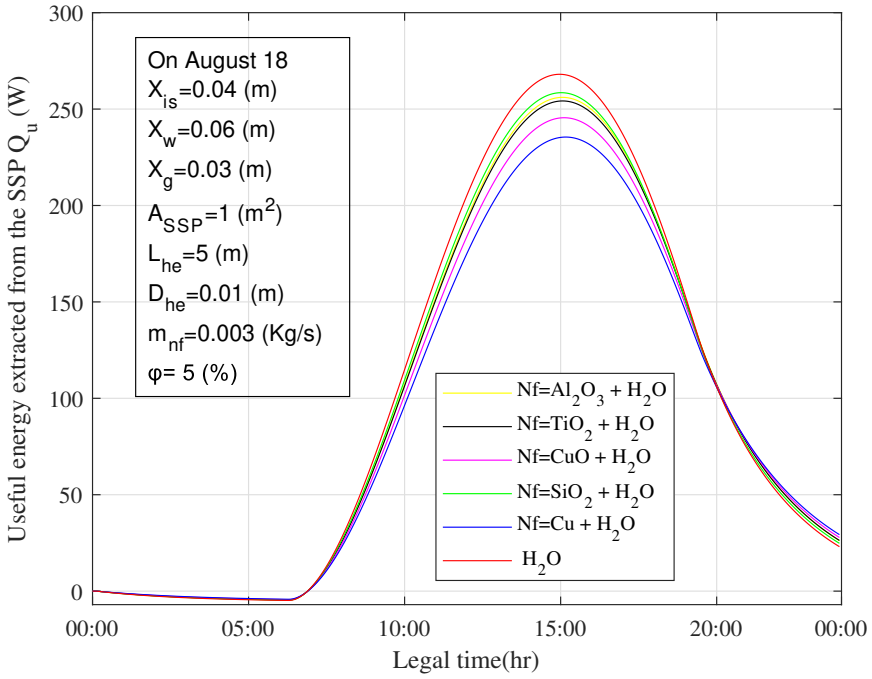


FIGURE 4.19: Comparison between calculate useful energy of the nanofluids vs time with nanoparticles φ=5 (%) for different types of nanofluids and $\dot{m}_{nf}$= 0.003 (Kg/s)

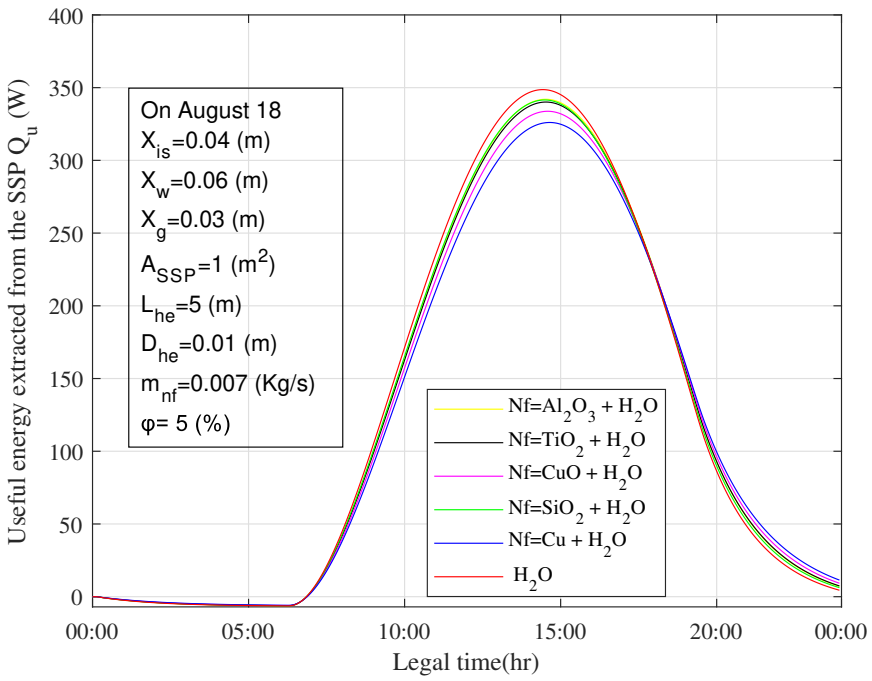


FIGURE 4.20: Comparison between calculate useful energy of the nanofluids vs time with nanoparticles φ=5 (%) for different types of nanofluids and $\dot{m}_{nf}$= 0.007 (Kg/s)

4.1.3.9 Comparison between the useful energy for different nanofluids

Figure 4.19 shows a comparison of the useful energy extracted from the pond for different nanofluids for a period from 00:00 AM to 00:00 PM, with volume fraction φ=5 (%). For a range of the time comprise between 00:00 am and 15:00 ,the useful energy increases and peaks for all types of nanofluids, with the mass flow rate $\dot{m}_{nf}$= 0.003 (Kg/s),The maximum useful energy for all nanofluids is obtained at 15:00 around: 260.77, 274.94, 287.289.52, 295.55 and 308.65 (W) and this is for $(Cu + H_2O)$, $(CuO + H_2O)$, $(TiO_2 + H_2O)$, $(Al_2O_3 + H_2O)$, $(SiO_2 + H_2O)$ and (H_2O) nanofluids respectively. However, with an increase in the mass flow rate $\dot{m}_{nf}$ = 0.007 (Kg/s),the value of the useful energy extracted increases significantly as shown in figure 4.20 and reaches a peaks at 15:00 are found to be :326.04, 333.75, 340.10, 342.01, 341.51 and 348.64 (W)respectively.It is clear that the effect of the mass flow rate is positive on the useful energy, but the effect of nanoparticles is negative despite the increase in the mass flow rate. However, the highest recorded value for the useful energy extracted is for the heat transfer fluid represented by pure water.

4.1.3.10 The effect of nanoparticles on daily efficiency

The daily efficiency of both types is shown, whether the daily efficiency of heat removal as shown in figure 4.22 and the daily efficiency of collection as shown in figure 4.21 in its development is a behavior contrary to temperature, as the results obtained showed that the daily efficiency is inversely proportional to the volume fraction of the nanoparticles, and that for all nanofluids, But it is directly proportional to the mass flow rate of nanofluids, however, despite the increase in the mass flow rate that the best thermal performance provided by the solar pond is the use of pure water as a heat transfer fluid, we think that this is due to the negative effect of the nanoparticles on the heat capacity of the basic fluid as shown in figure 4.13

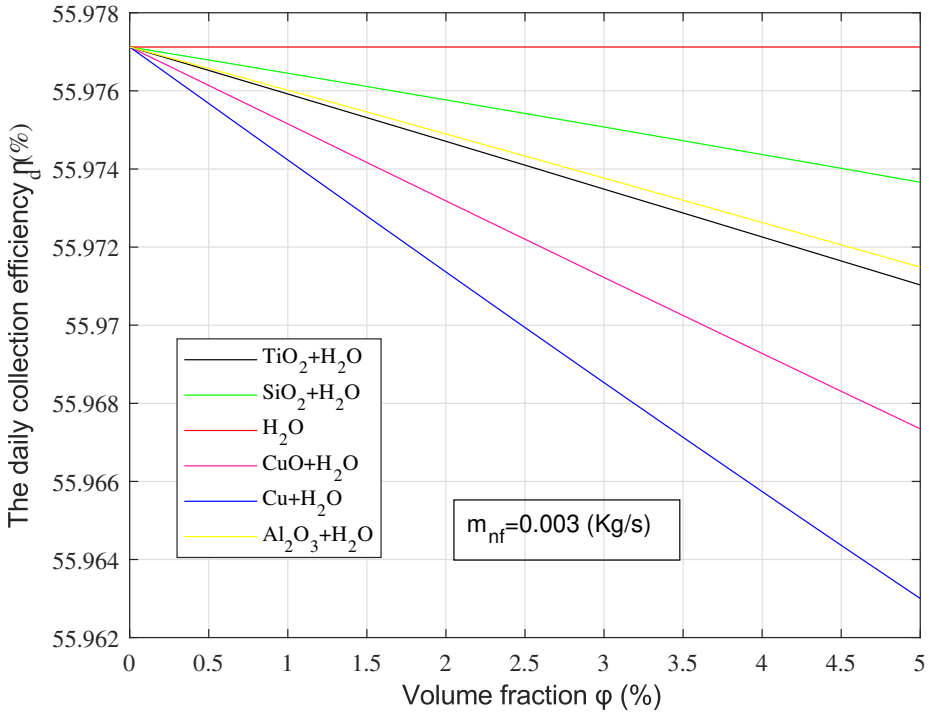


FIGURE 4.21: Daily collection efficiency with nanoparticle volume fraction φ=5 (%) for different types of nanofluids: $\dot{m}_{nf}$ = 0.003 (Kg/s)

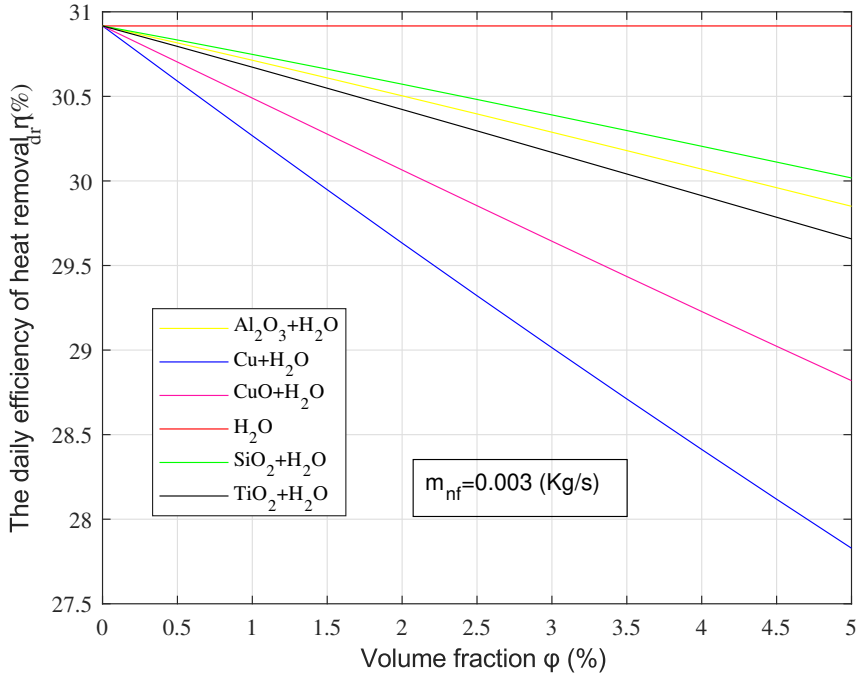


FIGURE 4.22: Daily efficiency of heat removell with nanoparticle volume fraction φ=5 (%) for different types of nanofluids: $\dot{m}_{nf}$ = 0.003 (Kg/s)

Chapter 5

Experimental techniques

5.1 Introduction

In order to test the thermal performance of a shallow solar pond operating in batch mode on one hand and open and continuous mode of heat extraction on the other hand experimentally and compare it with theoretical results in order to test the viability of the mathematical model .The SSP was performed from previously obtained dimensions of theoretical simulations. The SSP was manufactured locally using a stainless galvanized material with dimensions of 2 * 1 (m). The SSP is made with 0.06 (m) depth and 1 (m^2) area with dimensions of 0.76 *1.3 (m), the bottom of the SSP is painted black in order to enhance the absorption of solar radiation, and the SSP is supplied with two transparent glass covers and this is in order to enhance global warming inside the pond. In order to maintain pond water temperature and reduce heat loss at night, SSP is covered on both sides and the bottom with 0.04 (m) thick polyester. Finally, in order to test the SSP in open and continuous heat extraction mode, the SSP is provided with a heat exchanger from a material of PVC with length 10 $(m)$and diameter 0.008(m) .

5.2 Material and Methods

5.2.1 Solar Radiation Calculation

In order to obtain the value of solar radiation, and in view of the inability to obtain a solar radiation measuring device, a semiempirical model (BIRD & HULSTROM) is used to calculate the value of solar radiation on 18 August under the longitude of 3.0930 degrees and latitude 36.2022 degrees and altitude of 581 (m) in The city of Tablat located in Medea in Algeria.

5.2.2 Temperature Measurement

5.2.2.1 Ambient air temperature and humidity measurement

The ambient air temperature and humidity were measured using a temperature and humidity sensor (DHT22), a DHT22 communicates with a microcontroller via a serial port.The temperature and humidity sensor DHT22 has the following specifications:

- Power supply: 3.3 to 6 vdc
- Maximum consumption: 1.5 ma
- Consumption at rest: 50 µa

Measuring range:

- Temperature: -40 to +80 $(^{\circ}C)$
- Humidity: 0 to 100 (%) rh

Precision:

- Temperature: ± 0.5 $(^{\circ}C)$
- Humidity: ± 2 (%) rh

Dimensions: 25 x 15 x 9 (mm)

5.2.2.2 Measuring the Temperature of SSP Components

The temperature of the pond components was measured using a waterproof temperature sensor (DS18B20). It is connected to a microcontroller via a digital input.The temperature sensor DS18B20 has the following specifications:

- Power supply: 3 to 5 (Vdc)
- Accuracy: 0.5(%) from -10 to +85 $(^{\circ}C)$
- Measuring range: -55 to + 125 $(^{\circ}C)$
- Connects to a digital input
- Probe dimensions: Ø6 x 35 (mm)
- Cord length: 90 (cm)

5.2.3 Microcontroller

The Arduino Uno is a programmable microcontroller that allows to control mechanical elements: systems, lights, motors, etc. This electronic card therefore allows its user to easily program things and create automated mechanisms, without having any particular programming knowledge. An Arduino uno board was used to program temperature sensors DHT22 and DS18B20 ,and display the results on the computer.

5.2.4 Water Pump

QR30E Ultra Quiet Brushless Mini Pump, with the following specifications:

- Fluids: Water, oil, gasoline, acid and alkali solution, etc.
- Power consumption:4.2(W)
- Rated voltage:12 (V)
- Max flow rate:240 (L/H)
- Outer diameter of inlet / outlet:9 (mm)
- Inner diameter of inlet / outlet:6 (mm)
- Product size:56 x 52 x 47 (mm)

It was used to circulate the heat transfer fluid and overcome the pressure drop.

5.3 Experiment Description

The experiment is done under two heat extraction modes:

5.3.1 The SSP is operated under the batch mode for heat extraction

The experiment was conducted in the city of Tablat on August 19, 2019, using a prototype that was manufactured using local materials. Four temperature sensors, type DS18B20, are installed over the two glass covers, one inside the pond water, and one touching the bottom of the pond (the absorber plate),

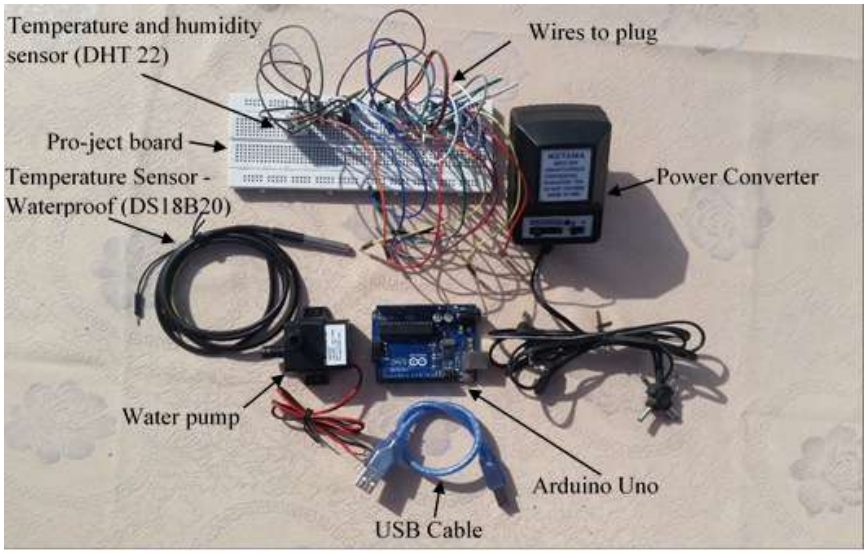


FIGURE 5.1: Measuring instrument used in the experimental study

and the ambient air temperature and humidity are measured by the DHT22 temperature and humidity sensor, all of these sensors are connected to the computer via a Arduino Uno board , Finally, these sensors were programmed to measure the temperature of the various components of the pond from 08:00 AM until 20:00 PM, and record the experimental values every minute. The prepared prototype enables to measurement of changes in the following parameters:

- Ambient air temperature
- Ambient air humidity
- The temperature of the upper glass cover
- The lower glass cover temperature
- Pond water temperature
- The temperature of the absorber plate

In order to compare the experimental and theoretical results, a computer program was prepared using Matlab software, depending on the solutions of differential equations resulting from the energy balance equations between the various components of the SSP, the program includes the input parameters represented in the design, operational and climatic factors, the solar

radiation was calculated by using the semi-emperical model (BIRD & HULSTROM), while the ambient air temperature was measured using the sensor (DHT22) and entered into the computer programs.



FIGURE 5.2: Photograph showing the operation of the SSP under the batch mode of heat extraction

5.3.2 The SSP is operated under open cycle and continuous heat extraction mode

Using the same parameters as those used in the first mode, the experiment is carried out in open cycle and continuous heat extraction mode on August 18, 2019, a PVC heat exchanger is placed at the bottom of the SSP and a water pump is used to circulate the heat transfer fluid represented by water. 2 temperature sensors (DS18B20) are placed in the inlet and outlet of the heat exchanger to measure the inlet and outlet temperature of the heat transfer fluid. The prepared prototype enables measurement of changes in the following parameters:

- Ambient air temperature
- Ambient air humidity
- The temperature of the upper glass cover
- The lower glass cover temperature
- Pond water temperature

- The initial temperature of the heat transfer fluid
- The final temperature of the heat transfer fluid
- The temperature of the absorber plate



FIGURE 5.3: Photograph showing the operation of the SSP under the open cycle mode of heat extraction

5.4 Results of Experimental Tests

5.4 shows hourly variations of the horizontal solar radiation calculated by Bird Hulstrom model using geographical coordinates of the site of the experiment, as well as the date it was conducted,It is seen that the maximum value of the solar radiation is 1011 W/m2 at noon.

Hourly variations of the measured ambient air temperature Ta when the pond operates under the batch mode of heat extraction on 19 August 2019 is presented in 5.5

Figure 5.6 shows a comparison between the calculated and experimental results for the temperature of the upper glass cover of the solar pond operating under the batch mode to extract the heat. It is noticeable that the calculated values are somewhat close to the experimental values, as we record the highest experimental value estimated at 42.63 $(^{\circ}C)$, while the calculated value is 40.87 $(^{\circ}C)$ at 14:00 PM, the relative error between these two values is equal 4.12 (%), on the other hand the relative error between the average daily

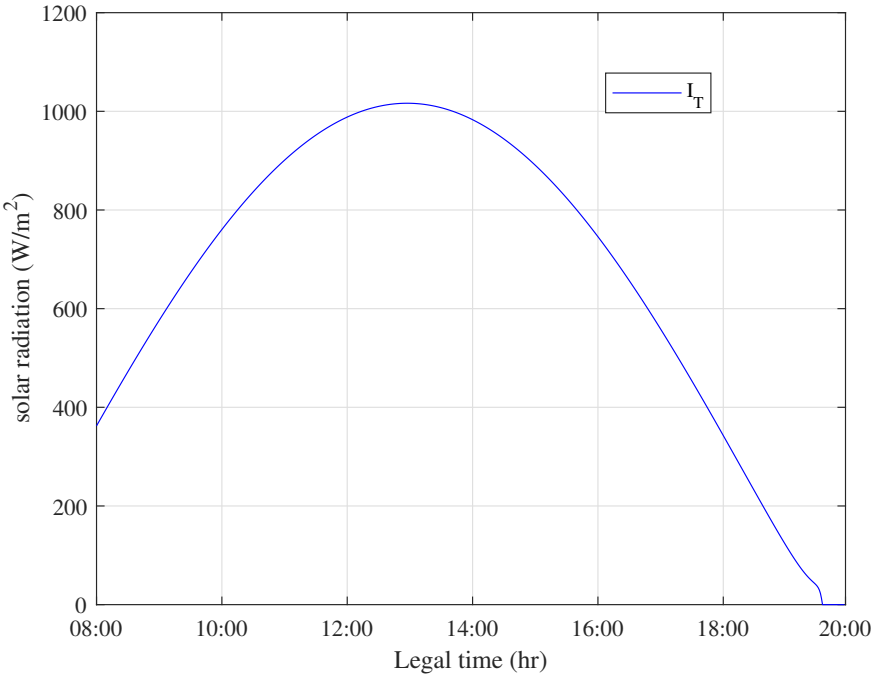


FIGURE 5.4: Hourly variations of the calculated solar radiation by Bird & Hulstrom model

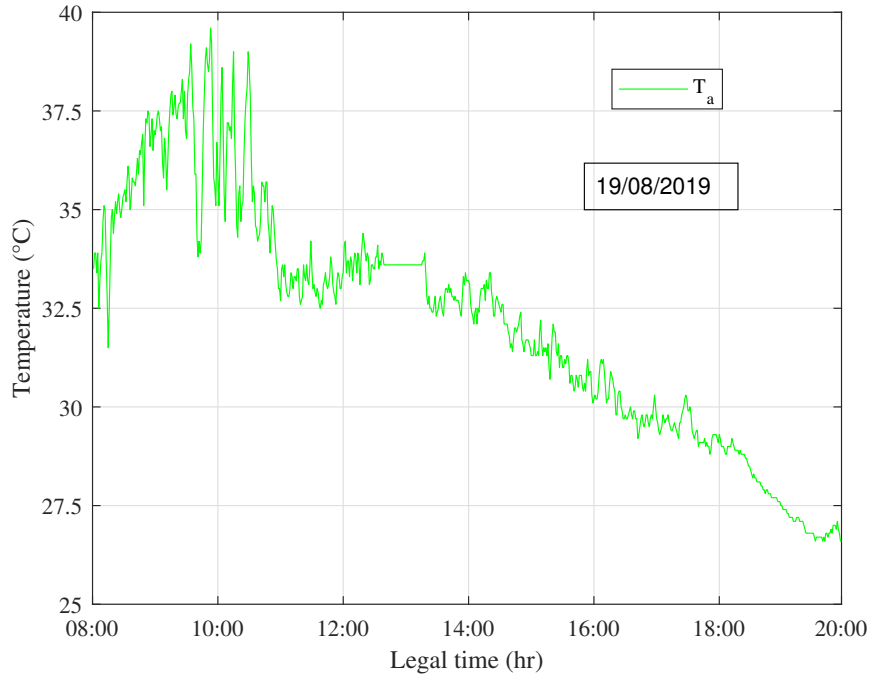


FIGURE 5.5: Hourly variations of the measured ambient temperature under the batch mode of heat extraction

values experimental and calculated values equal-2.57 (%).

As shown in the figure 5.7, the agreement between the calculated and exper-

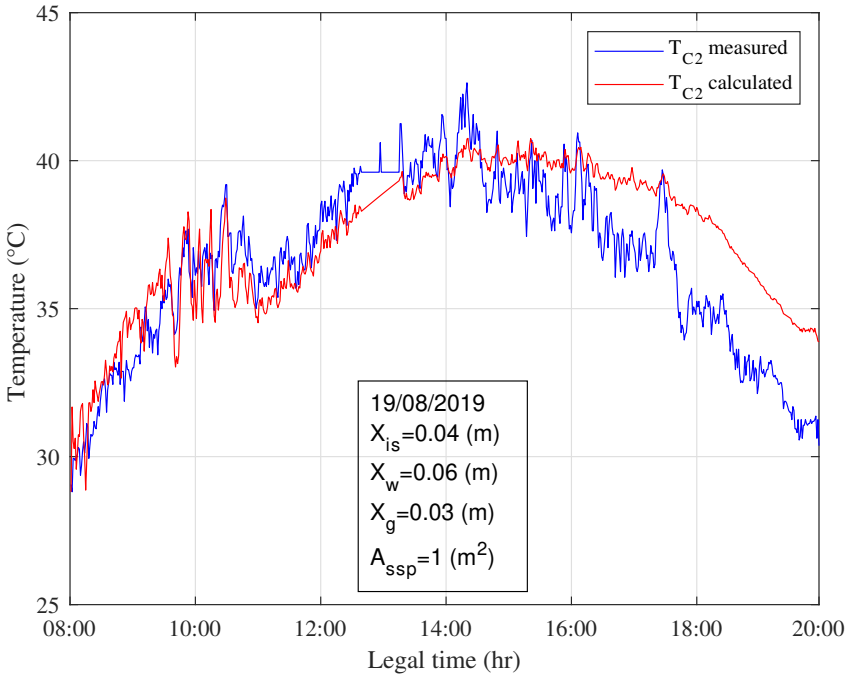


FIGURE 5.6: Comparison between experimental and calculated results for the temperature of the upper glass cover of the SSP operating under the batch mode for heat extraction

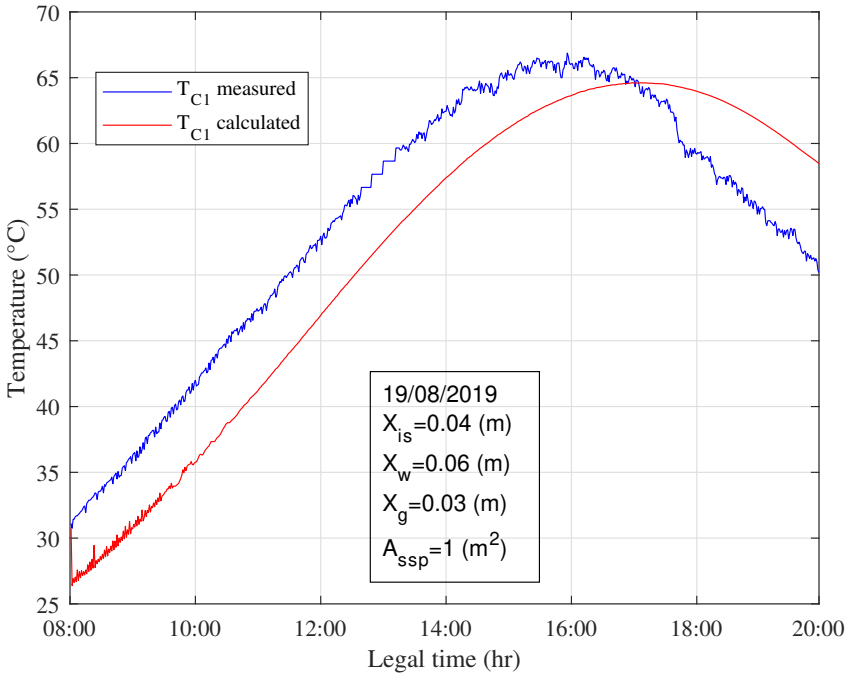


FIGURE 5.7: Comparison between experimental and calculated results for the temperature of the lower glass cover of the SSP operating under the batch mode for heat extraction

imental values of the temperature of the lower glass cover for a pond operating under the batch mode for heat extraction is good ,The experimental and calculated temperature of the lower glass cover reached its maximum value which is 66.87 $(°C)$ and 64.73 $(°C)$ respectively .It is found that the value of the relative error between the the maximum values of the experimental and calculated is 3.20 (%).On the other hand, the relative error between the daily average values of the experimental and calculated is 3.10 (%).

Figures 5.8 and 5.9 show a comparison between the experimental and cal-

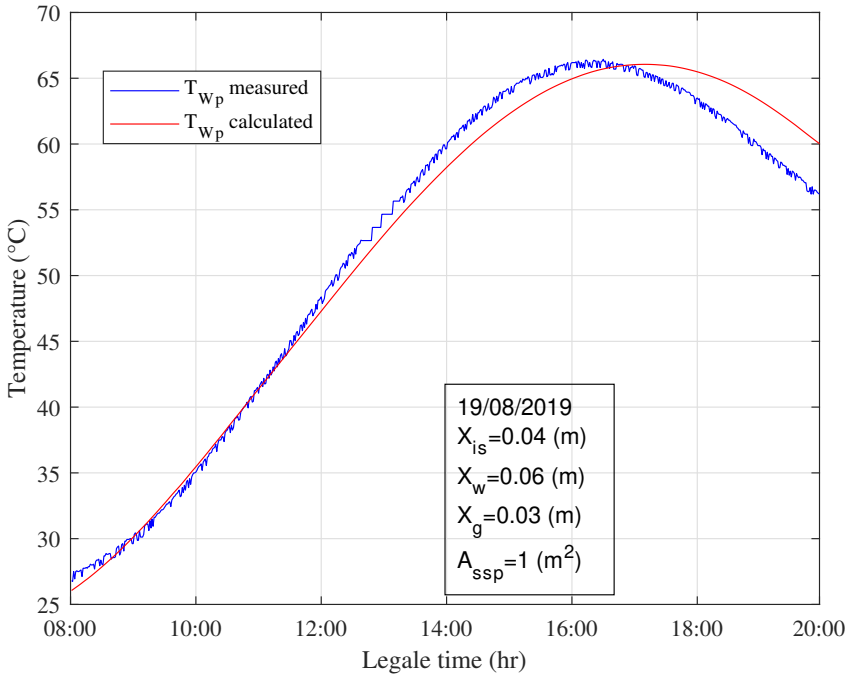


FIGURE 5.8: Comparison between experimental and calculated results for the temperature of the pond water of the SSP operating under the batch mode for heat extraction

culated temperatures for each of the pond water and the absorber plate respectively. The results obtained showed that the agreement between the experimental and calculated results is somewhat acceptable. The relative error between the maximum values of the experimental and calculated temperature of the pond water and temperature of the absorber plate are obtained as 0.33 (%) and 0.15(%), respectively. On the other hand, the relative error between the daily average values of the experimental and calculated temperature of the pond water and temperature of the absorber plate are found to be -1.53 (%) and -1.78 (%), respectively.

Hourly variations of the measured ambient air temperature Ta when the

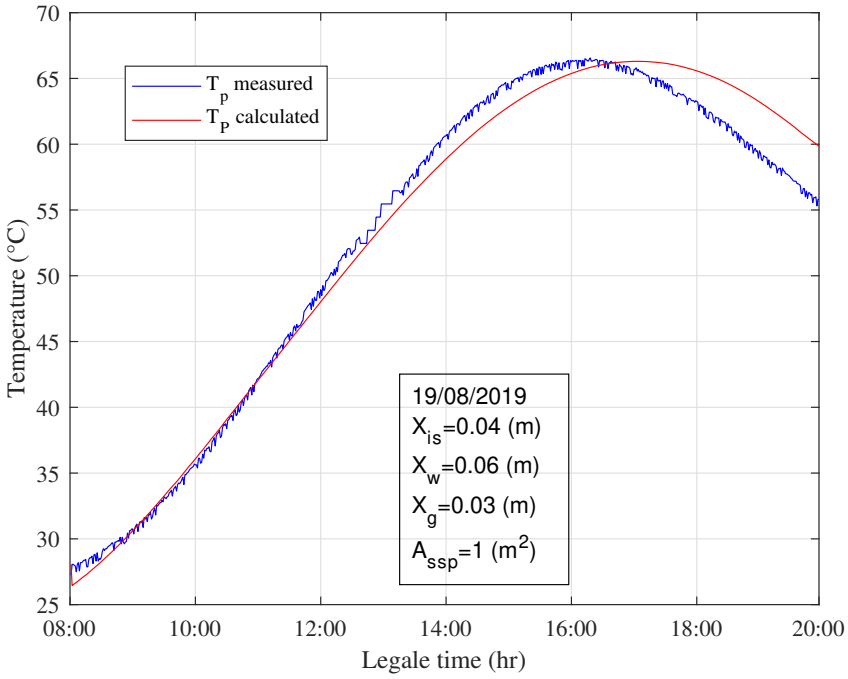


FIGURE 5.9: Comparison between experimental and calculated results for the temperature of the absorber plate of the SSP operating under the batch mode for heat extraction

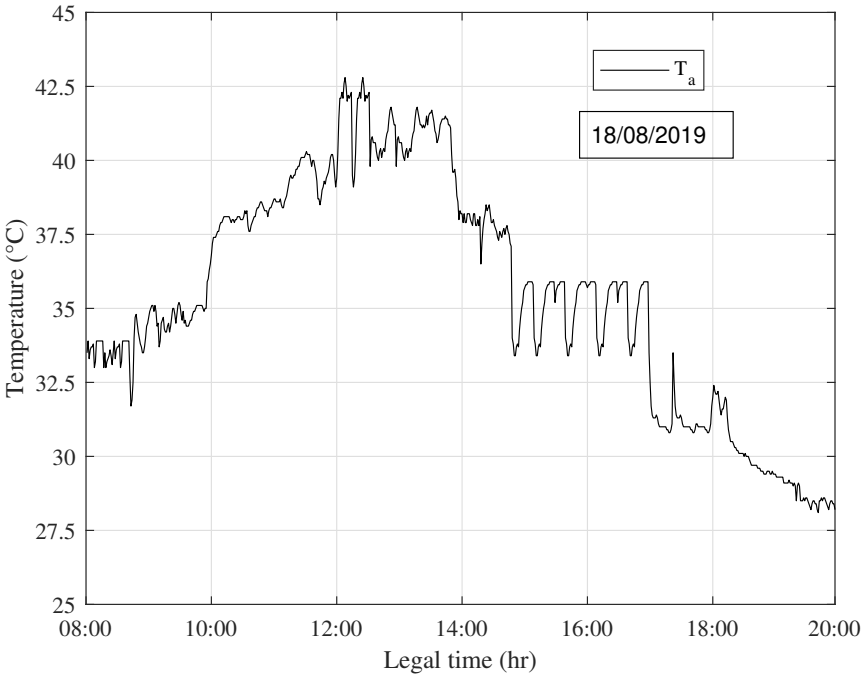


FIGURE 5.10: Hourly variations of the measured ambient temperature under the open cycle mode of heat extraction

pond operates under the open cycle mode of heat extraction on 18 August 2019 is presented in 5.10

Figure 5.12 shows a comparison between the experimental and calculated

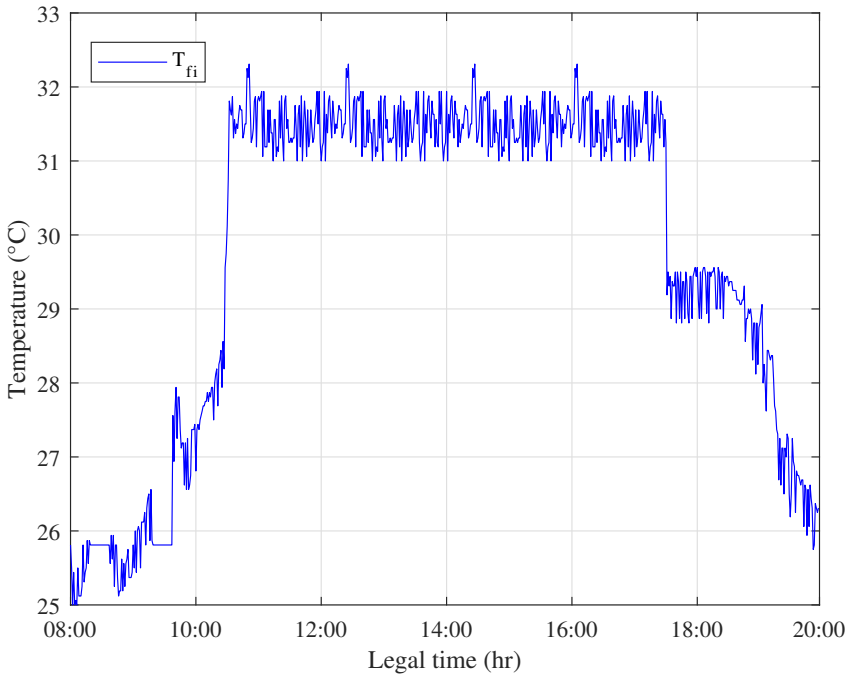


FIGURE 5.11: Hourly variations of the measured inlet temperature of the heat transfer fluid under the open cycle mode of heat extraction

results for the temperature of the upper glass cover of a shallow solar pond operating under the open cycle mode and continuous heat extraction. It is noticeable that the two curves show almost the same appearance, as the relative error value between the maximum values of the experimental and calculated is 7.61 (%), On the other hand, the relative error between the daily average values of the experimental and calculated is 1.43 (%).

Figure 5.13 shows a comparison between the experimental and calculated results for the temperature of the lower glass cover. It is noticeable that the two curves show almost the same appearance, as the relative error value between the maximum values of the experimental and calculated is 2.87 (%), On the other hand, the relative error between the daily average values of the experimental and calculated is 0.56 (%). Figure 5.14 shows a comparison between the experimental and calculated results for the outlet temperature of the heat transfer fluid. It is noticeable that the two curves show almost the same appearance, as the relative error value between the maximum values

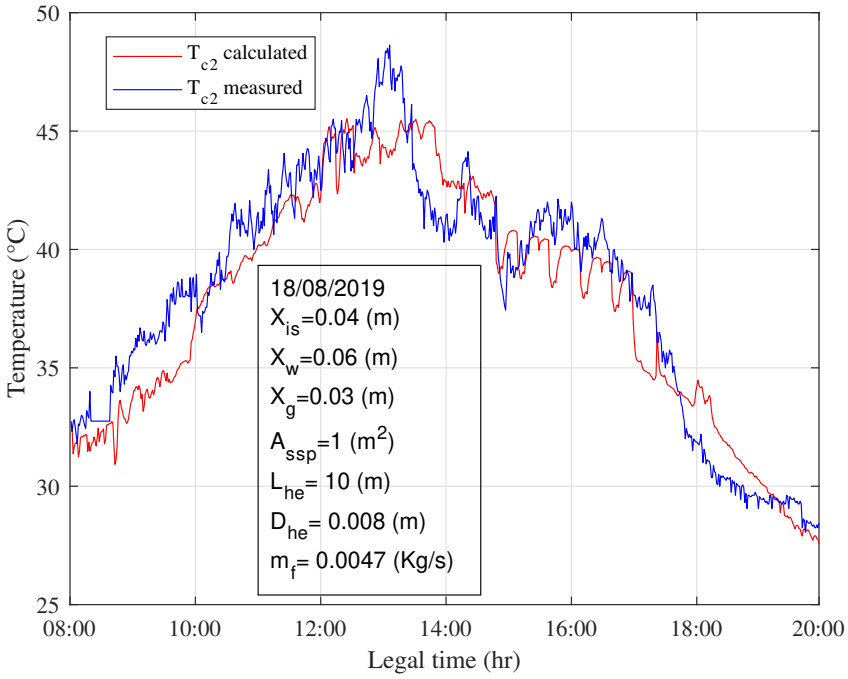


FIGURE 5.12: Comparison between experimental and calculated results for the temperature of the upper glass cover of the SSP operating under the open cycle and continuous heat extraction mode

of the experimental and calculated is 0.28 (%), On the other hand, the relative error between the daily average values of the experimental and calculated is -3.37(%).

Figures 5.15 and 5.16 show a comparison between the experimental and calculated temperatures for each of the pond water and the absorber plate respectively. The results obtained showed that the agreement between the experimental and calculated results is somewhat acceptable. The relative error between the maximum values of the experimental and calculated temperature of the pond water and temperature of the absorber plate are obtained as 2.68 (%) and 2.72(%) respectively. On the other hand, the relative error between the daily average values of the experimental and calculated temperature of the pond water and temperature of the absorber plate are found to be 0.15 (%) and -0.23 (%)respectively.

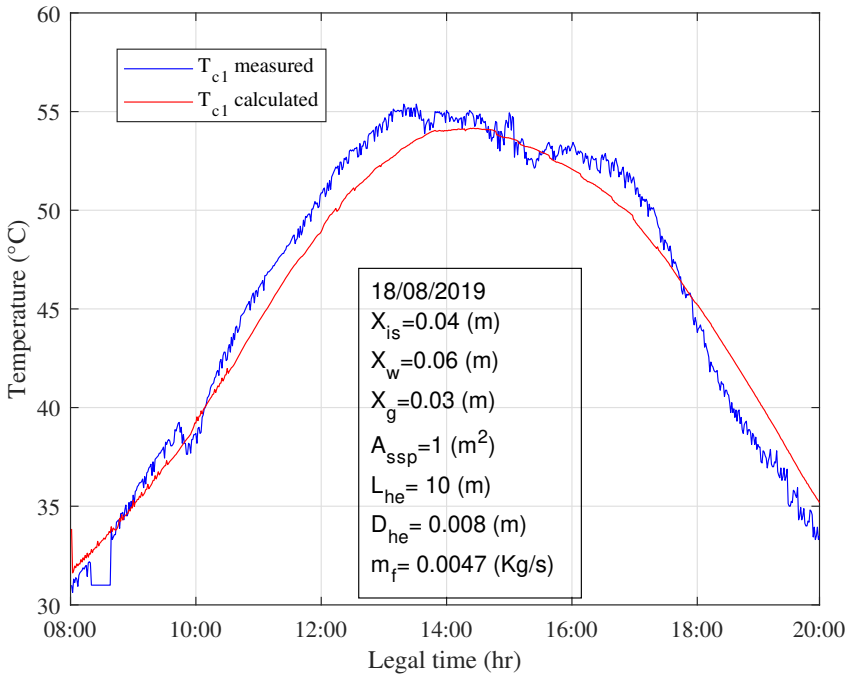


FIGURE 5.13: Comparison between experimental and calculated results for the temperature of the lower glass cover of the SSP operating under the open cycle and continuous heat extraction mode

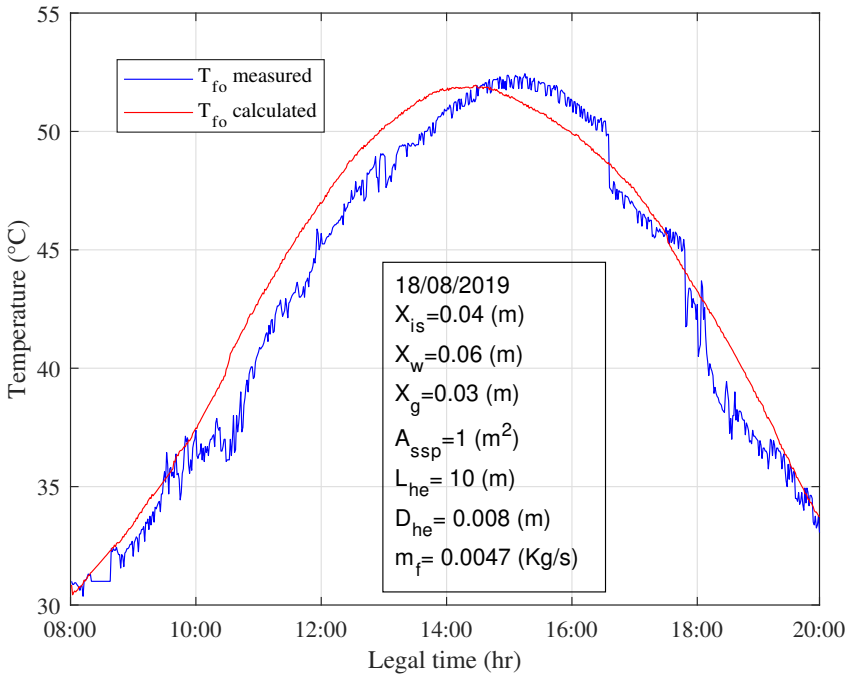


FIGURE 5.14: Comparison between experimental and calculated results for the outlet temperature of the heat transfer fluid of the SSP operating under the open cycle and continuous heat extraction mode

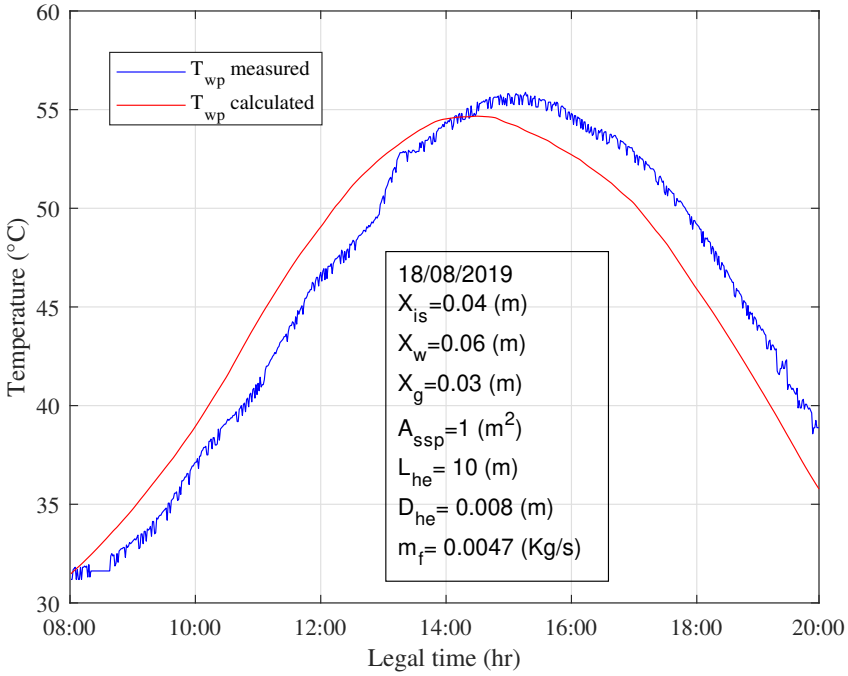


FIGURE 5.15: Comparison between experimental and calculated results for the pond water temperature of the SSP operating under the open cycle and continuous heat extraction mode

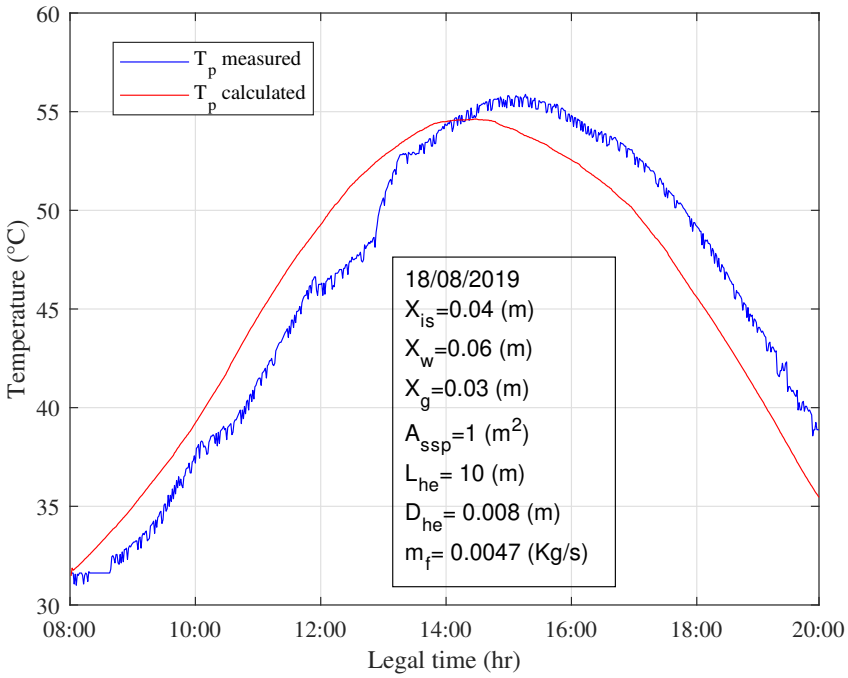


FIGURE 5.16: Comparison between experimental and calculated results for the temperature of the absorber plate of the SSP operating under the open cycle and continuous heat extraction mode

General Conclusion

The aim of this work is to study the thermal performance of a shallow solar pond operating under the batch mode for heat extraction, and the open cycle and continuous heat extraction mode , in addition to studying the effect of using nanofluids as a fluids to extract heat from a solar pond working under the open cycle mode and continuous heat extraction. In the end, a prototype of the pond was made in order to test the validity of the mathematical model used in the numerical simulation experimentally. The results obtained from the numerical simulation of the solar radiation modeling by using each of the four models proposed in the study equations to calculate the global solar radiation and compare it with the measured values. We found that the (Davies & Hay) model and the (Bird & Hulstrom) model give a good estimate of solar irradiance. The results obtained by the two previous models approach with great accuracy the real data. A shallow solar pond was studied in the batch mode for heat extraction under the various designs of the pond, including the depth of the pond and the thickness of the insulating material, the results obtained showed that:

- The thermal performance of the pond increases with the increasing thickness of the insulating material
- The optimum value of the insulating material is about 0.04 (m).
- The most important parameter that affects the thermal performance of the solar pond is the depth of the pond water, as the results showed that the temperature of the pond water decreases with the increasing depth of the pond.
- The pond can provide about 60 liters of hot water, the temperature of which may reach 65 $(^{\circ}C)$ with a depth equals 0.06 (m).

Among the methods of extracting heat from the pond is the use of a heat exchanger and the operation of the pond under the open cycle mode and continuous extraction of heat, for this reason a numerical simulation was made

to choose the length and diameter of the ideal heat exchanger in addition to the mass flow rate, the results obtained showed that:

- The outlet temperature of the heat transfer fluid is directly proportional to the length of the heat exchanger.
- The optimum value of the heat exchanger is about 4 (m), after which the increase in temperature becomes insignificant with the increase in the length of the heat exchanger.
- It was also found that the increase in the diameter of the heat exchanger positively affects the outlet temperature of the heat transfer fluid and that the typical value of the diameter of the heat exchanger is about 0.03 (m).
- The numerical simulation showed that the outlet temperature of the heat transfer fluid decreases with the increase in the mass flow rate of the heat transfer fluid.
- The typical value of the mass flow rate can be considered 0.003 (Kg/s).
- Operating the pond under open circulation mode and continuous extraction of heat with these parameters allows to obtain a heat transfer fluid with a temperature of up to 55 $(°C)$

Testing the thermal performance of a shallow solar pond under the open cycle and the continuous extraction of heat under different types of nanofluids with a concentration ranging up to five percent led to the following conclusions:

- The outlet temperature of the nanofluid increases with the increase in the nanoparticle concentration.
- $(Cu + H_2O)$ nanofluid has the highest temperature compared to other nanofluids
- The increase in the mass flow rate negatively affects the temperature of the nanofluids
- The increase in the mass flow rate positively affects the daily efficiency of the pond and the beneficial energy extracted from the pond
- The daily efficiency decreases with the increase in the volume fraction

We present an experimental study of a shallow solar pond operating under two different heat extraction modes. This locally produced pond was placed on a test platform in Tablat Town for a series of thermal measurements. Thanks to these experimental results on the pond, we got the following results:

- The temperature of the pond water operating in the batch mode for heat extraction reaches its maximum value at 16:00 in the afternoon, with a maximum value of 66 $(^{\circ}C)$, which equates to 60 (Kg) of hot water
- The relative error between the daily average values of the experimental and calculated temperature of the pond water found to be -1.53 (%), which confirms the effectiveness of the mathematical model used in the numerical simulation

The operation of the solar pond under the open cycle and the continuous extraction of heat by using water as a heat transfer fluid experimentally allowed to obtain the following conclusions:

- With a mass flow of heat transfer fluid equal 0.0047 (Kg/s), the temperature of the heat transfer fluid at the outlet of the heat exchanger has a maximum value of 52.06 $(^{\circ}C)$ at 15:30 pm.
- The relative error between the mean daily values for the experiment and calculated for the heat transfer fluid is -3.37 (%) ,
- The agreement between measured and calculated results is fairly good; therefore, the proposed mathematical models can be used for estimating the thermal performance of the SSP with open and continuous heat extraction with reasonable accuracy

Bibliography

[1] Lyes Maifi and Tahar Kerbache. Etude et modélisation d'un panneau solaire thermique photovoltaïque. 2018.

[2] Ismail Tabet. Étude, réalisation et simulation d'un capteur solaire. 2016.

[3] Abdelkrim Terfai, Younes Chiba, and Mohamed Najib Bouaziz. Artificial neural networks modeling of a shallow solar pond. In *International Conference in Artificial Intelligence in Renewable Energetic Systems*, pages 491–496. Springer, 2018.

[4] MRI Ramadan, AA El-Sebaii, S Aboul-Enein, and AM Khallaf. Experimental testing of a shallow solar pond with continuous heat extraction. *Energy and buildings*, 36(9):955–964, 2004.

[5] Gladés Bachir. *Contribution à l'étude de la convection naturelle dans les nanofluides en configuration de Rayleigh-Bénard*. PhD thesis, Université de Toulouse, Université Toulouse III-Paul Sabatier, 2010.

[6] AA El-Sebaii, MRI Ramadan, S Aboul-Enein, and AM Khallaf. History of the solar ponds: a review study. *Renewable and Sustainable Energy Reviews*, 15(6):3319–3325, 2011.

[7] WC Dickinson, AF Clark, JA Day, and LF Wouters. The shallow solar pond energy conversion system. *Solar Energy*, 18(1):3–10, 1976.

[8] ND Kaushika. Solar ponds: A review. *Energy conversion and management*, 24(4):353–376, 1984.

[9] Ibrahim Alenezi. *Salinity Gradient Solar Ponds: Theoretical Modelling and Integration with Desalination.* PhD thesis, University of Surrey, 2012.

[10] P.E. William A. Tolbert. State-of -the-art review of solar ponds. 1981.

[11] S Aboul-Enein, AA El-Sebaii, MRI Ramadan, and AM Khallaf. Parametric study of a shallow solar-pond under the batch mode of heat extraction. *Applied Energy*, 78(2):159–177, 2004.

[12] HP Garg, B Bandyopadhyay, Usha Rani, and DS Hrishikesan. Shallow solar pond: state-of-the-art. *Energy Conversion and Management*, 22(2):117–131, 1982.

[13] AI Kudish and D Wolf. A compact shallow solar pond hot water heater. *Solar Energy*, 21(4):317–322, 1978.

[14] MS Sodha, GN Tiwari, and JK Nayak. Shallow solar pond water heater: an analytical study. *Energy Conversion and Management*, 21(2):137–139, 1981.

[15] MS Sodha, NK Bansal, PK Bansal, and DS Hirishikeshan. A study of plastic shallow solar pond water heater for domestic applications. *Sol. Energy;(United Kingdom)*, 34(6), 1985.

[16] DK Dutt, SN Rai, and GN Tiwari. Transient analysis of a shallow solar pond water heater integrated with a baffle plate. *Energy conversion and management*, 27(3):303–307, 1987.

[17] K Kamiuto and T Oda. Thermal performance of a shallow solar-pond water heater with semitransparent, multilayer surface insulation. *Energy*, 16(10):1239–1245, 1991.

[18] VVN Kishore, MR Gandhi, and KS Rao. Experimental and analytical studies of shallow solar pond systems with continuous heat extraction. *Solar energy*, 36(3):245–256, 1986.

[19] HM Ali and M Akhlaghi. Experimental study in a shallow solar pond. *Solar & wind technology*, 4(4):425–430, 1987.

[20] Said MA Ibrahim and Medhat K El-Reidy. Performance of a mobile covered shallow solar pond. *Renewable energy*, 6(2):89–100, 1995.

[21] AA El-Sebaii. Thermal performance of a shallow solar-pond integrated with a baffle plate. *Applied Energy*, 81(1):33–53, 2005.

[22] AA El-Sebaii, S Aboul-Enein, MRI Ramadan, and AM Khallaf. Thermal performance of shallow solar pond under open cycle continuous flow heating mode for heat extraction. *Energy conversion and management*, 47(7-8):1014–1031, 2006.

[23] AA El-Sebaii, S Aboul-Enein, MRI Ramadan, and AM Khallaf. Thermal performance of shallow solar pond under open and closed cycle modes of heat extraction. *Solar energy*, 95:30–41, 2013.

[24] K Shanmugasundaram B Janarthanan. Comparative study of shallow solar ponds with different depths. *Mapana Journal of Sciences*, 13(1):13–28, 2014.

[25] AA El-Sebaii, MRI Ramadan, S Aboul-Enein, and N Salem. Thermal performance of a single-basin solar still integrated with a shallow solar pond. *Energy conversion and Management*, 49(10):2839–2848, 2008.

[26] Abdelkrim Terfai, Younes Chiba, and Mohamed Nadjib Bouaziz. Numerical simulation of shallow solar pond operating under open and closed cycle modes to extract heat, in the medea area, algeria. In *International Conference in Artificial Intelligence in Renewable Energetic Systems*, pages 173–183. Springer, 2019.

[27] Abdelkrim Terfai, Younes Chiba, and Mohamed Nadjib Bouaziz. Etude numérique d'un bassin d'eau solaire opérant dans la zone de médéa, algérie.

[28] Abdelkrim Terfai, Younes Chiba, and Mohamed Nadjib Bouaziz.

[29] Abdelkrim Terfai, Younes Chiba, and Mohamed Nadjib Bouaziz. Numerical study of shallow solar pond by using neural networks method. In *2018 International Conference on Applied Smart Systems (ICASS)*, pages 1–4. IEEE, 2018.

[30] AA El-Sebaii, S Aboul-Enein, MRI Ramadan, and AM Khallaf. Thermal performance of an active single basin solar still (asbs) coupled to shallow solar pond (ssp). *Desalination*, 280(1-3):183–190, 2011.

[31] Basharat Jamil and Naiem Akhtar. Comparative analysis of diffuse solar radiation models based on sky-clearness index and sunshine period for humid-subtropical climatic region of india: A case study. *Renewable and Sustainable Energy Reviews*, 78:329–355, 2017.

[32] Jianyuan Zhang, Li Zhao, Shuai Deng, Weicong Xu, and Ying Zhang. A critical review of the models used to estimate solar radiation. *Renewable and Sustainable Energy Reviews*, 70:314–329, 2017.

[33] Michel Capderou. Atlas solaire de l'algérie, modèles théoriques et expérimentaux. *Vol. 1, T1, Office des Publications Universitaires, Algérie*, 1987.

[34] M Mesri-Merad, I Rougab, A Cheknane, and NI Bachari. Estimation du rayonnement solaire au sol par des modèles semi-empiriques. *Revue des Energies Renouvelables*, 15(3):451–463, 2012.

[35] Richard E Bird and Roland L Hulstrom. Simplified clear sky model for direct and diffuse insolation on horizontal surfaces. Technical report, Solar Energy Research Inst., Golden, CO (USA), 1981.

[36] M MesriMoukhtari. Introduction au gisement solaire algérien théorie et applications. *Doctorant en Energies Renouvelables, Université Amar Telidji–Laghouat*.

[37] Younes Chiba. Etude de l'utilisation d'un bassin d'eau comme capteur solaria.université frères mentouri constantine 1. 2005.

[38] Frank Kreith, Raj M Manglik, and Mark S Bohn. *Principles of heat transfer*. Nelson Education, 2012.

[39] John A Duffie and William A Beckman. Solar engineering of thermal processes, fourth editio, 2013.

[40] Rahman Saidur, KY Leong, and Hussein A Mohammed. A review on applications and challenges of nanofluids. *Renewable and sustainable energy reviews*, 15(3):1646–1668, 2011.

[41] Salma Halelfadl. *Caractérisation des propriétés thermo-physiques et d'échanges de chaleur des nanofluides à base de nanotubes de carbone (Doctoral dissertation)*. PhD thesis, 2014.

[42] Gabriela Huminic and Angel Huminic. Application of nanofluids in heat exchangers: A review. *Renewable and Sustainable Energy Reviews*, 16(8):5625–5638, 2012.

[43] Theodore L Bergman, Frank P Incropera, David P DeWitt, and Adrienne S Lavine. *Fundamentals of heat and mass transfer*. John Wiley & Sons, 2011.

[44] Sidi El Becaye Maiga, Samy Joseph Palm, Cong Tam Nguyen, Gilles Roy, and Nicolas Galanis. Heat transfer enhancement by using nanofluids in forced convection flows. *International journal of heat and fluid flow*, 26(4):530–546, 2005.